Université Libre de Bruxelles

Master Thesis

Simulating cosmic–ray air shower radio emission for the Askaryan Radio Array

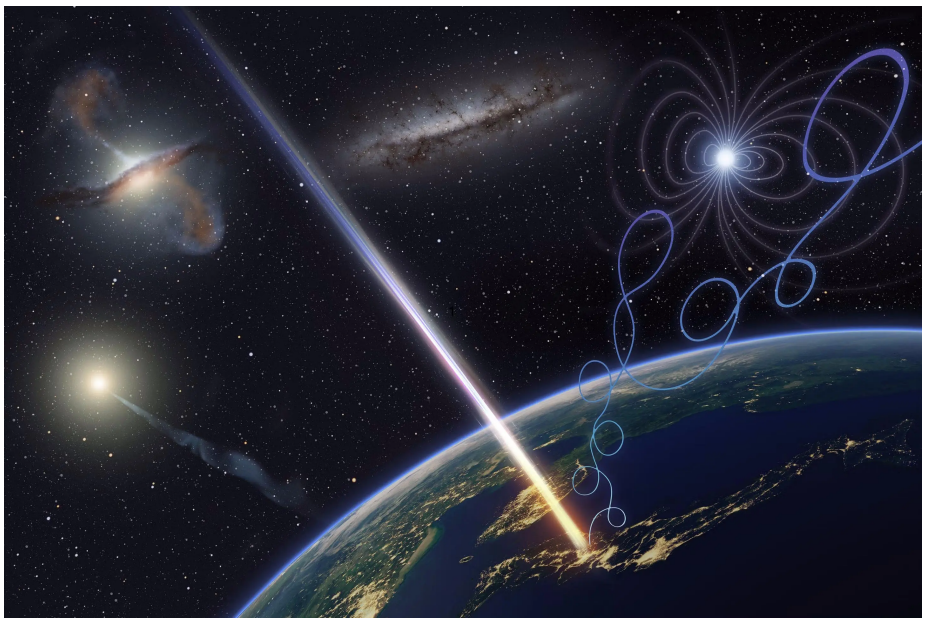

Nicolas Moller

Supervisors: Simona Toscano (ULB), Krijn De Vries (VUB)

June 20, 2024

Abstract

The flux of cosmic neutrinos drops rapidly towards the highest energies. Therefore, huge volumes of dense, signal transparent material have to be probed to allow for their detection. The Askaryan Radio Array (ARA) collaboration aims to probe this flux through the radio signal from the in-ice particle cascade induced upon the interaction of a cosmic neutrino. Recently, it was shown there is a second process that induces an in-ice particle cascade. Cosmic rays interacting in our atmosphere induce an in-air particle cascade, also referred to as an air–shower. Due to the high elevation of the polar ice sheet of $\sim$ 3 km, the in-air cascade will penetrate the ice-sheet. Its in-ice continuation is shown to have very similar properties to a neutrino-induced cascade. Therefore, this signal not only poses a background to the neutrino search, but if understood properly allows for the in-situ calibration of the detector.

The research presented in this thesis owes its realization to the FAERIE simulation framework, which was developed at VUB–IIHE. It is the first complete Monte–Carlo cosmic–ray radio emission simulation framework for in-ice detectors, including both the propagation of the particle cascade in air and in ice. This framework marks a significant advancement to the field, enabling the simulation of radio signals received by antennas positioned deep in the ice.
Within this study, the framework was used to generate a library of radio emission from cosmic–ray induced air–showers, including a study of their in-ice signature, as observed by the radio antennas in ARA $140 - 200$ m below the ice. This library offers a novel capability to map, in three dimensions, the footprint of radio emissions stemming from cosmic–ray induced particle cascades across a spectrum of energies and arrival directions. Using this library, we generate a simulated dataset of radio signals originating from cosmic rays at diverse antenna locations within the ice, mirroring the configuration of the Askaryan Radio Array. Furthermore, we compute the estimated cosmic–ray event rate for a single ARA station, which represent a crucial step for any analyses searching for CRs or neutrinos in ARA. The simulated dataset can also be used in future analyses to identify a cosmic–ray signature in ARA data, providing, for the very first time, a proof of concept for the detection of in-nature signals using the in–ice radio technique.

The first chapter introduces the important concepts for this dissertation and motivates the research of ultra high energy neutrinos with the radio method. In the second chapter, we discuss the radio detection technique before jumping into the simulations in Chapter 3, where first results are exposed. The Askaryan Radio Array is then presented in Chapter 4. The implementation of the simulations into the ARA framework in order to estimate a number of cosmic–ray event is discussed in Chapter 5. Finally, we conclude with prospects on continuing this work to differentiate cosmic–ray events from neutrino events in ARA.

Contents

1 Introduction

From immemorial time, humans have been watching the universe with curiosity, longing to reveal mysteries about the world they live in. This quest of knowledge about our universe was done for ages through one single messenger, visible light. With the later discovery of other bands of the electromagnetic spectrum (IR, X–rays, γ–rays, ...), astronomy allowed us to make countless discoveries and greatly improve our understanding of the universe, but it has its own limitations due to the very interactive nature of light. Happily, observational science underwent three recent revolutions that downgraded light from its privileged position as sole messenger.

The first one began in 1910 when a German physicist named Theodor Wulf measured an unexpected high ionization of the air at the top of the Eiffel Tower [1]. After that, measurements conducted in the high atmosphere by Victor Francis Hess confirmed the existence of a radiation coming from beyond our atmosphere [2]. These charged particles travelling through the universe before reaching us where called cosmic rays and gave rise to a whole new branch of observational science: Astroparticle physics. After this discovery, a lot of new experiments were conducted to better understand these new messengers and what information do they carry.

While the race for cosmic rays was going on, a third type of messenger was discovered: the neutrino. The first neutrino detection was near a nuclear reactor in 1956 [3]. The first atmospheric neutrino was then detected in 1965, and solar neutrinos were discovered in 1968 by the Homestake experiment [4]. The first supernovae neutrinos were detected in February 1987 by the Kamiokande experiment [5] and finally, cosmic neutrinos from unknown origin were detected by IceCube [6] for the first time in 2013, opening the path to neutrino astronomy as a tool to observe the universe.

Last but not least, the growing family of astro-messengers was enhanced again the 14 of september 2015 with the detection of the first gravitational wave [7], which is beyond the scope of this work.

Armed with cosmic rays, neutrinos and the good old particles of light, astroparticle physics has already proved to be quite fruitful, and yet is far from having revealed all its secrets.

1.1 UHE Astroparticle Physics

Cosmic rays and neutrinos give different informations and require different type of detectors so their study is usually done separately. This difference comes from their charge and the fundamental interaction that rules them. Furthermore, as can be seen in Fig. 1, the cosmic–ray flux extends to very high energies (neutrinos reach similar energies). While the low energy flux is fairly well understood, the high energy flux is more obscure, and its study gave rise to a sub-branch of astroparticle physics, the Ultra-High-Energy CR/ν physics.

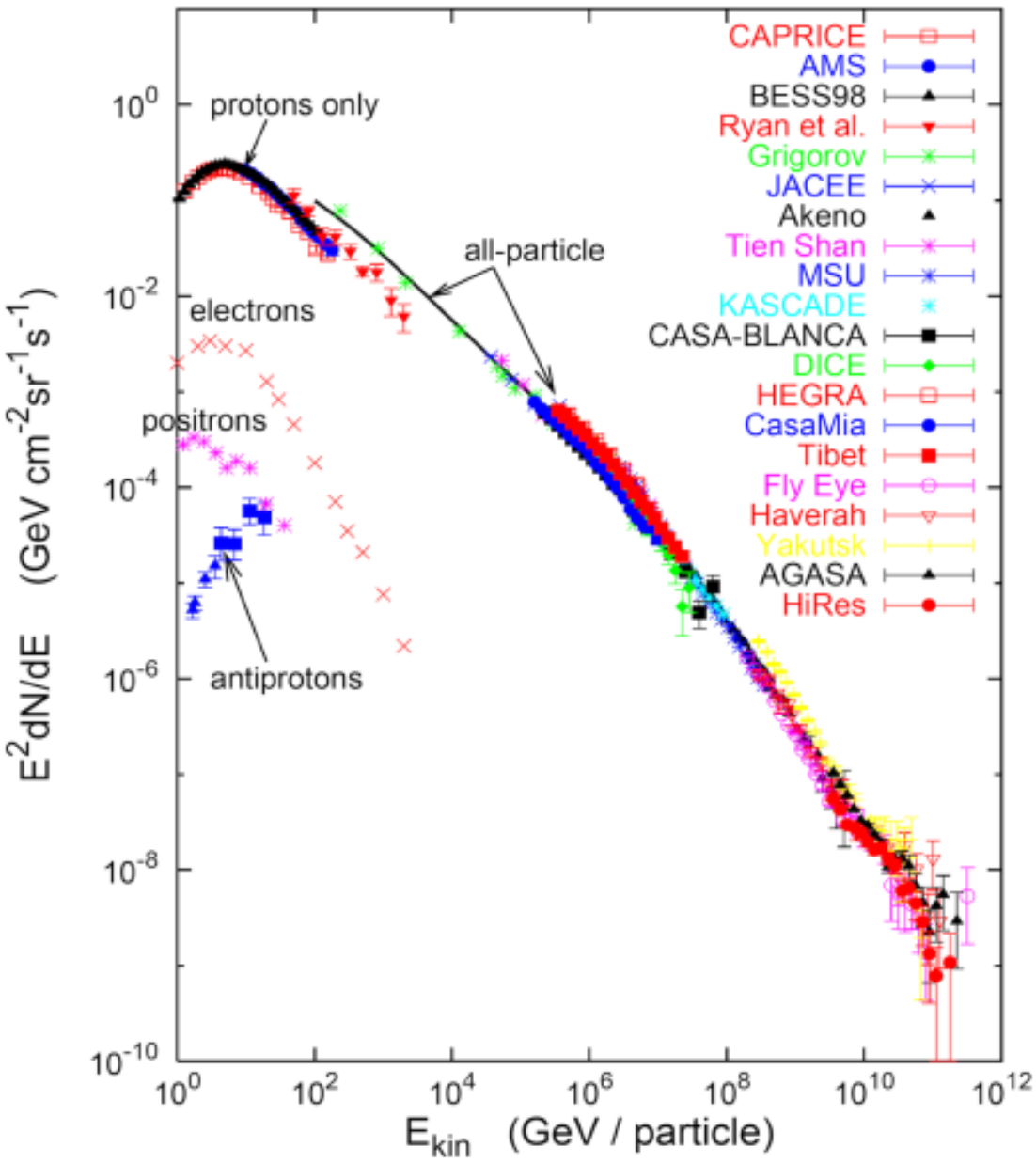

Figure 1: The cosmic–ray flux on Earth as measured by several experiments. The y–axis is multiplied by energy squared for visual reasons and the x–axis is in kinetic energy per nucleus. Kinetic energy is chosen because mass is negligible at these energies and energy–per–nucleus is preferred to energy–per–nucleons because cosmic–ray experiments using air–shower detection (see Section 1.2) generally measure a quantity which is related to total energy per particle. From [8].

1.1.1 UHE cosmic rays

As can be seen in Fig. 1 and Fig. 2, the cosmic–ray flux is dominated by protons up to 10^{15} eV, while the composition beyond that is still unclear. Recent measurements with the Pierre Auger Observatory (see Section 1.3) favors a mixed composition tending towards heavy nuclei at the highest energies.

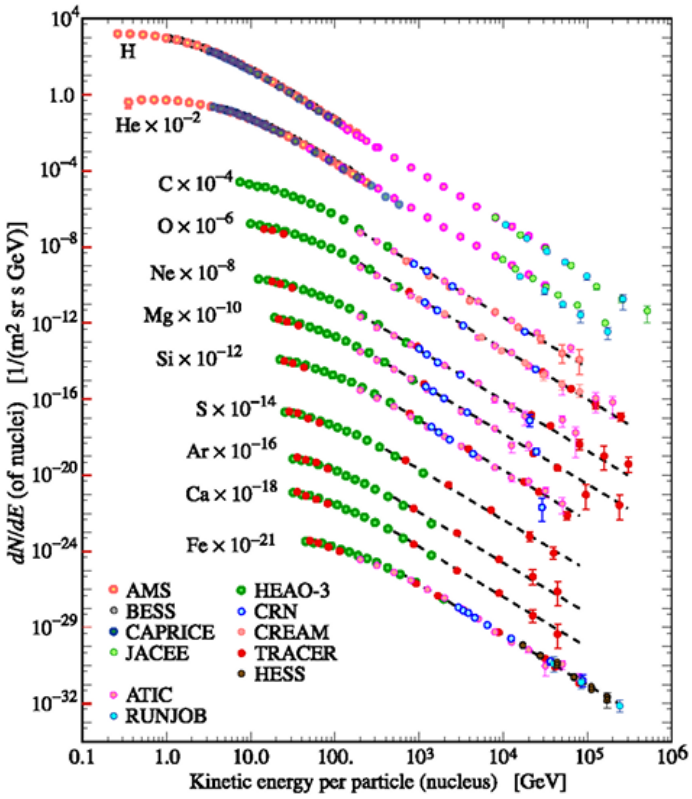

Figure 2: Composition of the bulk of cosmic rays: 80% are protons, 15% Helium nuclei and the rest is made of heavier nuclei (C, O, Fe, ...) and electrons. Each nuclei flux has been multiplied by an appropriate power of 10 to make it more visual. The X–axis is in kinetic energy per nucleus as in Fig. 1. From [9]

The first remarkable thing is that the flux covers 32 orders of magnitude; at very high energy, the flux goes down to 1 particle per km^2 per 10 years. The second is that the slope of the flux encounters several breaks that have been made more visible in Fig. 1 by multiplying the vertical axis by energy squared. We denote the first break around 3x10^{15} eV as the knee and the second break around 5×10^{18} eV as the ankle. Note also the sharp cut–off around 5×10^{19} eV. Identifying the sources of UHE cosmic rays could help us to better understand these breaks but this is not a simple task.

Indeed, as cosmic rays are charged nuclei (sometimes people include electrons and positrons but we can ignore them since they have only been observed at lower energies of $\sim 10^{12}$ eV), they are deflected by the galactic or intergalactic magnetic fields. Therefore, the information they carry on the direction of their source when reaching the Earth is limited.
This statement becomes false above 10^{19} eV where directionality becomes possible. Indeed, by equalising the Lorentz force with the centrifugal force:

$$qvB = \frac{mv^2}{r_L} \tag{1}$$

we obtain the radius of a cosmic–ray trajectory, called the Larmor radius, which, after correcting for relativity, can be expressed in the following way:

$$r_L = 1\,\mathrm{kpc}\left(\frac{E}{10^{18}\mathrm{eV}}\right)\left(\frac{1}{\mathrm{Z}}\right)\left(\frac{\mu G}{\mathrm{B}}\right) \tag{2}$$

A proton of 10^{19} eV travelling through a mean magnetic field of 10μG will then have a Larmor radius of 1kpc (1pc= 3×10^{16} m). Additionaly, if the Larmor radius of a cosmic ray is higher than the radius of the Milky Way, it will exit the galaxy. The maximum energy at which a proton created within the Milky Way can remain contained within it is determined by:

$$E < 10^{18}\left(\frac{h}{1\mathrm{kpc}}\right)\left(\frac{\mathrm{B}}{\mu G}\right) \sim 10^{17} - 10^{20} eV \tag{3}$$

where h is the galactic radius ($\sim 1 - 10$ kpc) and the galactic magnetic field varies between $0.1 - 10$ μG. It follows that the transition from galactic to extra-galactic origin is assumed to start around 10^{17} eV. A final effect to notice is the one pointed at by Greissen–Zatsepin and Kuz–min who predicted that protons should start to interact with Cosmic Microwave Background at energies above $10^{19.5}$ eV, which limits the horizon to tens or hundreds of Mpc. This is known as the GZK-effect [10, 11].

The energy at which the knee appears could be the maximum acceleration energy of the dominant galactic sources for light nuclei, while 10^{17} eV could be the limit for galactic heavy nuclei. The ankle could be due to the transition from galactic to extra-galactic origin and the final cut–off in the spectrum due to GZK-effect.

1.1.2 UHE–neutrinos

Neutrinos and photons are chargeless particles so they are not deflected by magnetic fields and thus provide a tool to point at sources. Photons are easy to detect but they interact easily inside sources and with the ISM[1] , while neutrinos are weakly interacting, which makes them the best candidates to look

[1]Interstellar medium, mostly composed of ionized hydrogen.

at very dense sources. This characteristic of neutrinos implies that they remain identical to when they left the source, ignoring flavor mixing. This comes to be very handy especially if one wants to look at the nuclear reactions in the center of the Sun, knowing that a photon takes around 10.000 years to reach its surface after numerous scatterings, while neutrinos take only a few seconds. In the same way as for the Sun, certain candidate sources for UHE cosmic rays are surrounded by opaque media, which makes photon astronomy useless in these cases. Neutrinos are thus the only reliable messengers to study these sources and they are not strangers to cosmic rays. In fact, UHE neutrinos can be produced by UHE cosmic rays interacting with the source environment:

$$p + p \rightarrow \begin{cases} p + p + \pi^0 & (2/3) \\ n + p + \pi^+ & (1/3) \end{cases} \tag{4}$$

Neutrons can then decay as:

$$n \rightarrow p + e^- + \overline{\nu_e} \tag{5}$$

or interact like protons, but with a π^- production:

$$n + p \rightarrow \begin{cases} n + p + \pi^0 & (2/3) \\ p + p + \pi^- & (1/3) \end{cases} \tag{6}$$

These pions then decay as:

$$\pi^+ \rightarrow \mu^+ + \nu_\mu \tag{7}$$

$$\mu^+ \rightarrow e^+ + \nu_e + \overline{\nu_\mu} \tag{8}$$

$$\pi^- \rightarrow \mu^- + \overline{\nu_\mu} \tag{9}$$

$$\mu^- \rightarrow e^- + \overline{\nu_e} + \nu_\mu \tag{10}$$

The proton–proton or neutron–proton interactions are dominant in opaque sources such as supernovae remnants because of the high quantity of matter. For sources featuring powerful electromagnetic emission, as Blazar jets for instance, radiation tends to dissipate the matter surrounding the source and proton–photon interactions become dominant:

$$p + \gamma \rightarrow p + \pi^0 \tag{11}$$

$$\pi^0 \rightarrow \gamma + \gamma \tag{12}$$

$$p + \gamma \rightarrow n + \pi^+ \tag{13}$$

The π^+ in Eq. 13 then decays as in Eqs. 7 and 8, while the π^0 decay shown in Eq. 12 is a source of high energy γ–rays that can be detected by the Fermi space telescope [12] for instance.

UHE neutrinos can also be produced during the propagation of the cosmic rays that managed to escape the source environment. Indeed, UHE cosmic rays can interact with CMB photons by the so-called GZK effect. This occurs for protons with energies above $10^{19.5}$ eV hitting the Δ^+ resonance:

$$p + \gamma \rightarrow \Delta^+ \rightarrow p + \pi^0 \tag{14}$$

$$\pi^0 \rightarrow \gamma + \gamma \tag{15}$$

$$p + \gamma \rightarrow \Delta^+ \rightarrow n + \pi^+ \tag{16}$$

$$\pi^+ \rightarrow \mu^+ + \nu_\mu \tag{17}$$

$$\mu^+ \rightarrow e^+ + \nu_e + \overline{\nu_\mu} \tag{18}$$

Note that the delta resonance can also occur within sources but is not required there since both photons and protons can have a very high energy.

The production of neutrinos is thus strongly related to the production of cosmic rays in sources. Since neutrinos come from cosmic–ray interactions, they carry only a fraction of their energy, typically 5% of the energy per nucleon. A heavy primary composition would therefore imply a lower neutrino flux.
An assumption one can make is that only neutrons escape the source and decay, producing the observed cosmic–ray and neutrino flux, while the protons remain trapped inside the source. A more realistic approach assume that some protons escape, meaning the observed cosmic–ray flux gives a lower limit on the total number of accelerated protons in the source. This is the Waxman–Bachall model [13]. In a general case, one can write the following relation between neutrino and cosmic–ray flux:

$$I_\nu(E_\nu) \sim n_{\nu/p} \frac{1}{\langle x_{p\rightarrow\nu} \rangle} I_p(E_p) \tag{19}$$

where $n_{\nu/p}$ is the number of neutrinos produced per proton interaction and $\langle x_{p\rightarrow\nu} \rangle$ is the fraction of the proton energy that goes into the neutrinos.

The small neutrino cross–section allows them to cross the entire universe without interacting. Neutrinos with energies up to $\sim$ 1 PeV can even cross the Earth from one side to another. This makes them incredibly hard to detect and require a large instrumented volume in order to obtain a substantial amount of events. One thing is to detect them, another is to point at sources. For that, IceCube (see Section 1.4) searches for a local excess of events in the sky with respect to the atmospheric neutrino background. This requires a lot of statistics and as of today only a few neutrino point sources have been found. The first UHE neutrino to be localized was detected in 2017. Its origin was announced a few months later as being the blazar TXS0506+056 located 5.7 billion light–years away in the direction of the Orion constellation [14]. More recently in 2022, another UHE–neutrino source detected by IceCube was found as being the active galactic nuclei of NGC1068, also known as Messier77 [15]. Another remarkable

result, in 2023, was the identification of diffuse neutrino emission from the Milky Way plane [16]. However, all these identified sources fail to account for the quantity of neutrino observed by IceCube, meaning that many more sources are yet to be discovered.

1.2 Cosmic–ray air–showers

We can consider UHE cosmic ray interactions in the atmosphere as proton–proton interactions, where slight differences with heavier cosmic nuclei are outlined below. These proton–proton interactions lead to cascades of particles, called air–showers. The difference with, for example, collisions at the LHC, is the energies involved. Indeed, UHE cosmic rays can reach energies $\sim 10^{21}$ eV well above the LHC reach. Another difference with experiments at LHC is that we are looking at fixed target interactions, which is very different from the case where two protons equally share the total energy. This leads to the cascade being oriented in the direction of the cosmic ray, rather than with a cylindrical symmetry. Finally, in the case of CR–initiated air–showers, the entire atmosphere plays the role of a calorimeter, and its conditions must be monitored as precisely as possible.
Due to the lack of knowledge on hadronic interactions in the regime of UHE fixed target collisions, the choice of hadronic model introduces an imprecision in the simulations, which then impacts the reconstruction of the air–shower parameters. An example is the excess of muons observed in air–showers with regard to the predictions [17, 18].

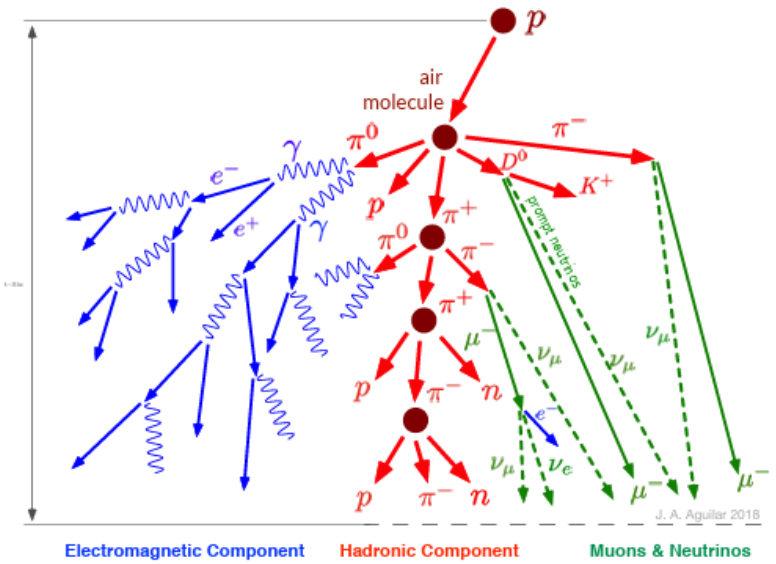

Figure 3: Schematic evolution of an air–shower. From [8]

Air–showers have 3 different components. The first one is the hadronic component, made mostly of protons, neutrons and pions. The second is the electromagnetic component, made of electrons, positrons and photons. This one is induced by the immediate decay of π^0 in 2 photons. The photons can then create a e^-/e^+ pair by virtual photon exchange. Electrons and positrons can also produce new photons thanks to the bremsstrahlung effect, and continue to feed the EM component of the shower. The third one is the muonic and neutrino component. Muons and neutrinos are produced by π^+ and π^- decay as in Eqs. 7, 8, 9 and 10.

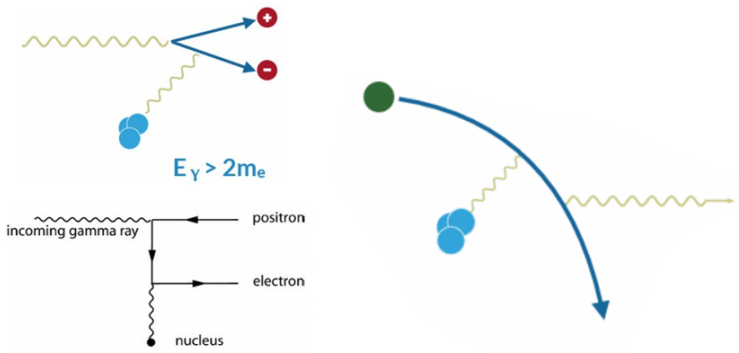

Figure 4: Pair production (left), and Bremsstrahlung (right).

Due to time dilatation, the muon life-time in the laboratory referential is long enough to reach the ground before they decay. For the electromagnetic part, both pair production and bremsstrahlung imply a growing number of particles. However, due to energy conservation, each particle carries less and less energy until ionization becomes the dominant interaction process at low energies. Ionization transfers energy to the atoms of the media, therefore the air–shower looses energy and the number of particles in the electromagnetic component decreases. The energy at which ionisation becomes dominant and the shower dies off is the critical energy (E_c).

$$\left.\frac{dE}{dx}(E_c)\right|_{Brems} = \left.\frac{dE}{dx}(E_c)\right|_{ion} \tag{20}$$

E_c depends strongly on material but empirically:

$$E_c = \frac{610MeV}{Z+1.24}(solid, liquid) \qquad E_c = \frac{710MeV}{Z+0.92}(gaz) \tag{21}$$

where Z is the mean number of protons of the media.

For the hadronic component a similar process occurs when pion decay becomes more probable than pion interaction. The production of new hadrons stops and the hadronic component dies off. The number of particles in an air–shower

thus reaches a maximum at a certain stage of evolution, which is deeper in the atmosphere for higher primary energies. The typical profile of an air–shower is shown in Fig. 5.

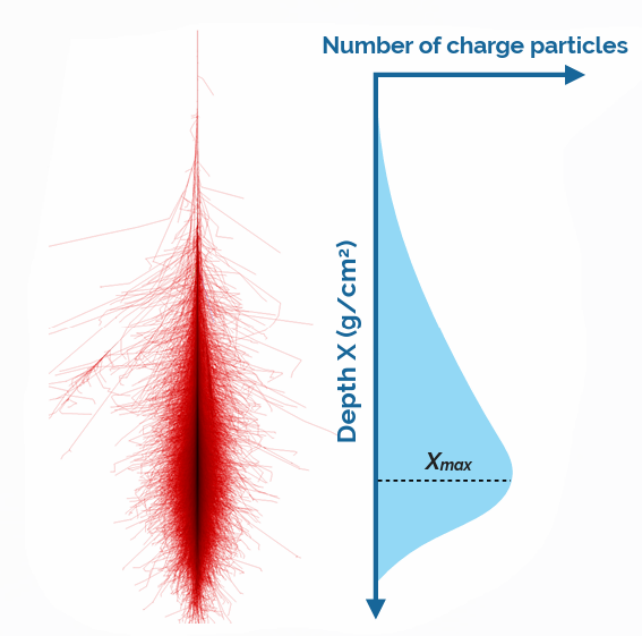

Figure 5: Schematic longitudinal development of an air–shower. From [8]

We define X_{max} as the position along the shower axis (defined by the prolongation of the primary particle track) where the number of particle is maximum. It is expressed in slant depth [g/cm^2], which is the density of the atmosphere integrated along the shower axis:

$$X_{\text{slant-depth}}(h,\theta) = \frac{1}{\cos(\theta)} \int_h^\infty \rho(h')\, dh' \tag{22}$$

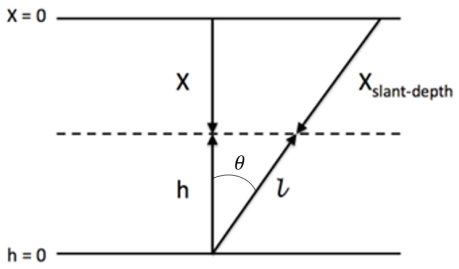

Figure 6: Slant–depth geometrical definition. From [8]

If we now want to consider a heavier nuclei hitting the atmosphere, we can use the superposition principle [19] according to which a nucleus with energy E_0 containing A nucleons will initiate A air–showers of energy $\frac{E_0}{A}$. With this supposition, X_{max} becomes:

$$X^A_{max}(E_0) = X^p_{max}(E_0) - X_0 \log(A) \tag{23}$$

where X_0 is the radiation length in the air and X^p_{max} is the X_{max} of a proton–induced air–shower. Therefore, the heavier the nuclei, the faster the shower will develop and the maximum of the shower will be higher in the atmosphere (smaller X_{max}).

1.3 Leading cosmic–ray detection methods

An air–shower is a complex process involving many particles over large distances (up to few kilometers wide). During its development, an air–shower has several ways to produce radiation, which can be detected and used to infer the air–shower properties. Another solution is to directly detect the particles of the air–shower by placing particle detectors on the ground or below. Both methods can be used together to reach a maximal precision and that is precisely what is done at the world leading cosmic–ray observatories, as the Pierre Auger Observatory (PAO) situated in Argentina [20].

The Pierre Auger Observatory uses several particle detectors on the ground (see Fig. 7), arranged in a regular pattern. The surface detectors consist of water tanks in which relativistic charged particles produce Cherenkov light. Depending on the energy range the experiment is optimized for, the distance between each particle detector can vary: the smaller the energy of the air–shower, the thinner it is, the closer the detectors must be from each other. In PAO the spacing goes over 1 km, targeting the detection of the highest energy particles. Showers are then detected by looking for time coincidences of signals in neighboring stations.

Together with the surface detectors, PAO features four telescopes positioned at higher altitudes to directly measure the longitudinal profile of the air–shower (see Fig. 8). This is done thanks to the fluorescence emission: if the shower energy exceeds 10^{17} eV, charged particles of the shower can excite the nitrogen molecules (N_2) present in the atmosphere. The de-excitation proceeds through two transitions of electronic states, as well as a change in vibrational and rotational states of the molecule. This leads to several fluorescence emission bands in the wavelength range from 300 to 400 m. If neglecting the other de-excitation processes, the number of emitted fluorescence photons would follow directly from the ionization energy deposited by the shower particles in the atmosphere. In practice, collision between molecules is an important non-radiative de-excitation process leading to an uncertainty in the energy reconstruction.

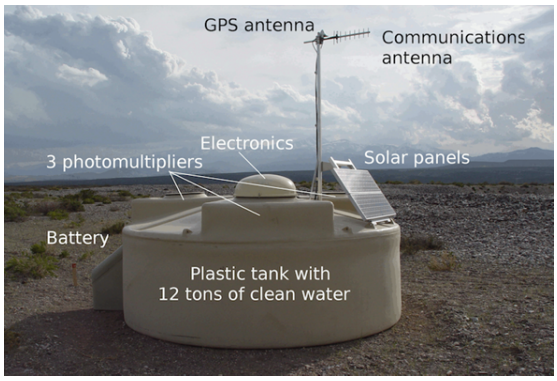

Figure 7: Surface detector of the Pierre Auger Observatory. Muons entering the tanks produce Cherenkov light while electrons and positrons produce photons via bremsstrahlung. The signal is then amplified by photomultipliers. From [21]

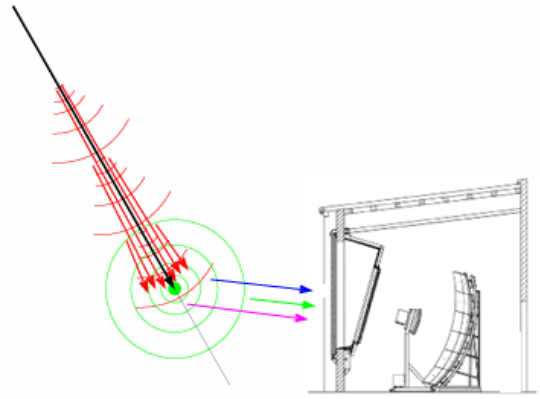

Figure 8: Principle of fluorescence telescopes as used in the Pierre–Auger Observatory. From [8]

1.4 Neutrino Detection

As previously mentioned, neutrino astronomy requires large instrumented volumes to make up for the low neutrino interaction cross–section. The current state–of–the–art technique is to detect Cherenkov light emitted by secondary particles that originate from a neutrino interaction in a transparent media like the ice. With this idea, the IceCube neutrino observatory was built at the South–Pole ice sheet, between 1.5 km and 2.5 km depth to decrease the atmospheric muon background and avoid scattering caused by air bubbles, which are more prevalent in shallower regions. IceCube is a large scale experiment in terms of the cutting-edge

technologies employed, the number of researchers involved in the project and the cost of the experiment. As of today, it is the world leading neutrino observatory.

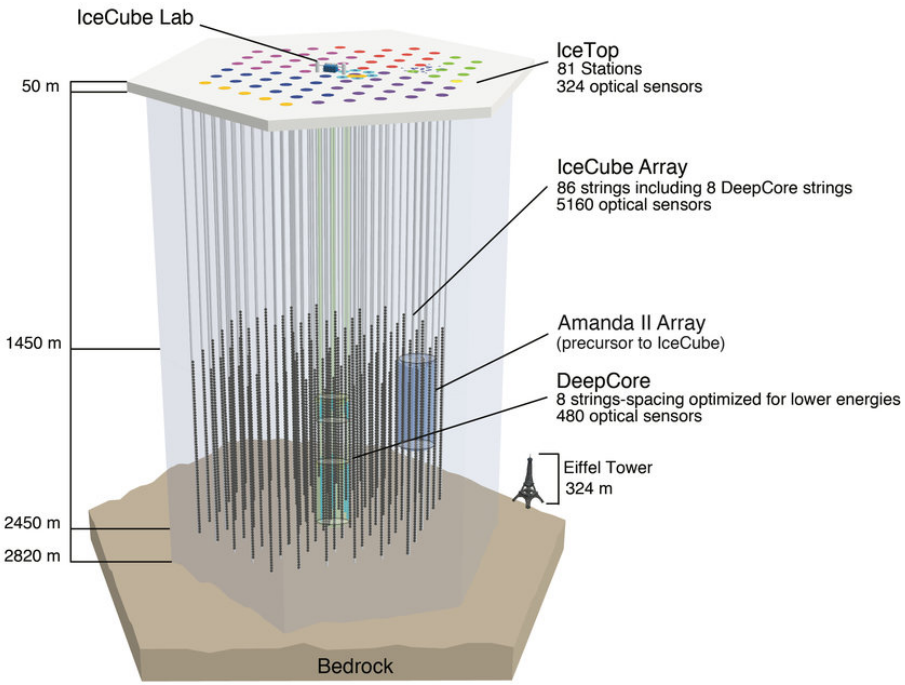

Figure 9: Layout of the IceCube Observatory at the South Pole. From Wikipedia

To detect the Cherenkov light, a large network of photomultipliers have been deployed with precise relative timing. The amount of detected light provides a measure of the energy of the event, and the arrival direction of the neutrino can be estimated from the light-arrival time in the individual photomultipliers.

With this method, IceCube has been able to probe the astrophysical neutrino flux in the TeV–PeV energy region and localized a few UHE–neutrino sources as mentioned in Section 1.1.2. However, statistics at ∼PeV energies is very limited. To address this limitation, IceCube has planned to expand the instrumented volume to ~ 8 km^3 with the future IceCube–Gen2 observatory. The upgraded observatory will also feature a radio array to detect UHE neutrinos across an area of about 500 km^2. While the mean free path of Cherenkov light in the ice is ~ 100 m, radio waves can travel distances of ~ 1 km, leading to much bigger detection volumes. Furthermore, the radio detection method is sensitive to primary energies above 10 PeV, which allows to explore the Ultra–High–Energy range of the neutrino flux, using relatively cheap detectors (radio antennas). Before implementing this new detection method in a large scale detector such as IceCube–Gen2, an in–situ proof–of–concept is required. With this idea, close to IceCube, the Askaryan Radio Array was constructed [22, 23]. ARA is a

first–generation radio neutrino detector and it will be the subject of Section 4. More recently, a second–generation radio neutrino detector named RNO–G was built in Greenland [24]. RNO–G is spanning an area of approximately 50 km^2 and will inform the design of the radio component of IceCube–Gen2.

1.5 Radio Detection of High–Energy Particle Cascades

The radio detection method appears as a cheap solution to compensate for the very low flux of UHE–neutrinos. It has an energy threshold of $\sim 10^{16.5}$ eV and is capable of probing vast areas thanks to the high mean free path of radio waves in ice. It would not only allow the detection of extra-galactic UHE neutrinos but also require only the deployment of a few radio antennas, providing a relatively inexpensive alternative to the detection techniques currently used around the world. Furthermore, the radio method can also be used to detect UHE cosmic rays, making it a versatile method for UHE astroparticle physics.

The first air–shower radio signal was detected in 1965 by Jelley et al.[25] but it is only recently that radio detection became a reliable method to study these phenomena. The 21st century has seen the birth of many experiments featuring arrays of radio antennas to make air–shower measurements ([26], [27], [28], [29], [30], ...). The radio reconstruction methods are still improving thanks to the very active radio community, meanwhile they already reached a competitive precision with regard to the previously discussed methods used in PAO, so that observatories with multiple detector systems could already profit from including radio measurements in a hybrid reconstruction of air–shower parameters. The present day accuracy of the radio technique on air–showers direction, total radiation energy and X_{max} position are respectively 0.7°, 17% and 40 g/cm^2 while the theoretical predictions are $< 0.1°$, $< 10\%$ and 30 g/cm^2 [31], so that radio reconstruction methods have still a lot of room for improvement.
This improvement in the past 20 years was allowed by a better understanding of the processes through which radio waves are emitted, mainly through the Geomagnetic effect [32, 33] and the Askaryan effect [34].

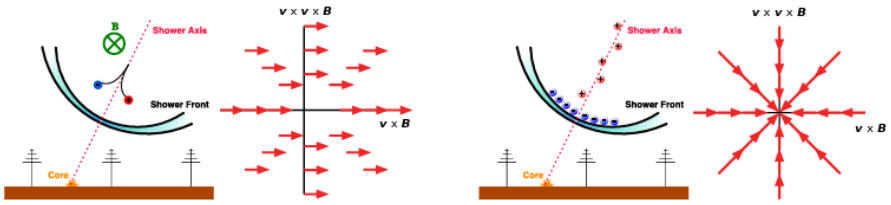

Figure 10: Sketch of the geomagnetic (left) and Askaryan (right) emission and their respective polarization. Note the shortening of the pulse close to the shower axis. From [35]

1.5.1 Geomagnetic Effect

During the development of an air–shower, the Earth magnetic field deflects electrons and positrons in opposite directions, which creates a current drifting perpendicular to the shower axis. This current varies with time according to the shower development, and reach its maximum value when the number of electromagnetic particles is maximum, which roughly corresponds to X_{max}. This time–varying current then induces radio waves. The geomagnetic radiation is linearly polarized in the direction orthogonal to local magnetic field and shower axis, and scales with the magnetic field strength perpendicular to the shower axis.
The time variation of the current is related to the initial growth of the air–shower and the later absorption in the atmosphere once the critical energy is reached. The radiated energy increases with the duration of the emission process, and thus with the longitudinal length of the shower maximum. For this reason, inclined showers radiate more than vertical showers, since they develop higher in the atmosphere where the density is smaller and the region around the shower maximum last thus longer, leading to increased emission.

1.5.2 Askaryan Effect

Askaryan emission is an other type of radio emission happening in an air–shower. This one is due to the accumulation of a negative net charge excess that builds up in the development of the shower: some positrons annihilate with electrons of the medium and photons ionize the surrounding atoms, which leads to an excess of electrons of 20–30% with respect to positrons along the shower axis. Charge conservation is maintained by the presence of a positively charged ionization trail created behind the shower. This charge excess increases until the shower maximum is reached. The shower can thus be seen as a point charge whose strength increases up to the shower maximum, and as the electric field lines of a point charge are radial, Askaryan emission is polarized radially inward.
This radio emission was predicted by Askaryan in the 1960s for showers in dense media [36, 37], where, as will be seen in the next section, Askaryan emission is the dominant effect.

1.6 Showers in Dense Media

As this work aims to study the cosmic–ray signal in ARA, which features in–ice radio antennas, not only the understanding of the air–shower is important, but also its propagation in the Polar ice sheet.

In an air–shower, the density of particles is the highest in a region of $\sim$1 m around the shower axis [35]. This is where most of the very high energy particles are located, while low energy particles are distributed more sparsely over long distances. Fig. 11 shows that the mean kinetic energy per particle grows when getting closer to the shower axis and the limit of 80 MeV, the critical energy,

that is represented by the black line is the limit above which electromagnetic particles are expected to initiate a cascade in the ice.

The shower core is defined as the point where the shower axis intersect the ground. This notion is important because the particles located within ten(s) of centimeter from the shower core are the one that will interact in the ice and initiate a cascade thanks to pair–production[2] and Bremsstrahlung, while the low energy particles far from the shower core will quickly die out because of energy losses by ionization. Even the particles 1 m away from the shower core will mostly vanish after a single radiation length[3] once entering the ice.
This work focuses on the South–Pole ice but similar properties are expected for other dense media. From now on we will only consider the particles located within 1 m from the shower core to describe the in–ice cascade. This assumption is discussed more thoroughly in Section 3.

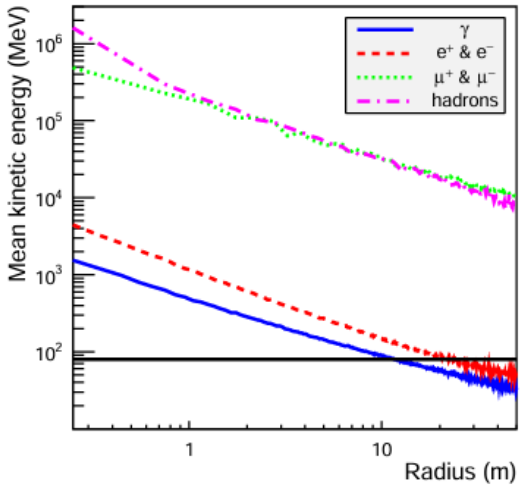

Figure 11: Average kinetic energy per particle in function of radius for different components of a simulated air–shower with an energy of 10^{17} eV and a zenith angle of $\theta = 0°$, at an altitude of 2.4km. The black horizontal line indicates the value of 80 MeV. From [38]

From Fig. 12 we see that an in–ice shower is made of a very energy-dense core that is typically ~ 50 cm wide and decreases radially very fast. The more inclined the air–shower is, the longer it has to travel through the atmosphere before reaching the ground, meaning less particles will make it to the ice and initiate an in–ice cascade. This implies that the energy of an in–ice cascade drops rapidly with increasing zenith angle.

[2]Only the electromagnetic part is of interest for radio emission so only electromagnetic processes and π_0 production is relevant

[3]Mean free path of an electromagnetic particle in a specific media before its energy is reduced by a factor 1/e

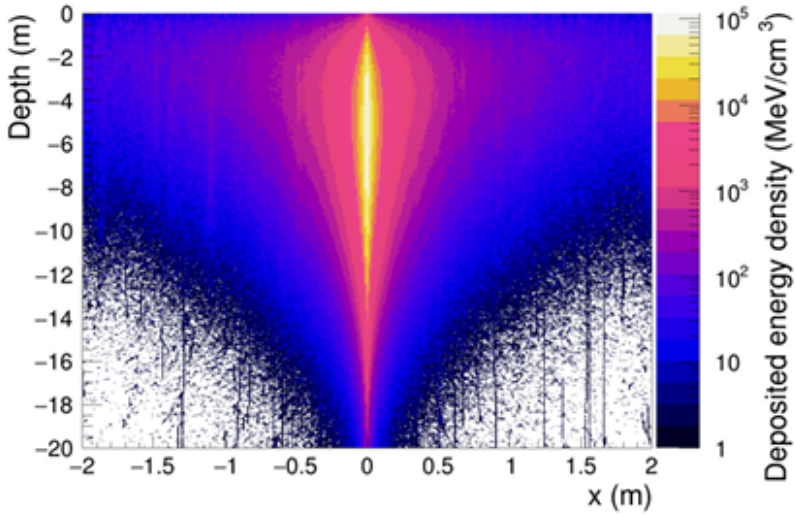

Figure 12: Energy deposited in ice by a simulated air–shower. Shown here is the deposited energy density within a vertical 1 cm wide slice going through the center of the particle shower. From [38]

The first difference with an air–shower is the much shorter radiation length due to the higher density of the ice. An in–ice cascade will therefore develop way faster than an air–shower, leading to a vertical extension of $10 - 20$ meters rather than kilometers. This is very important for radio emission because it causes the geomagnetic effect to be completely negligible, meaning the Askaryan effect becomes the dominant type of emission. Indeed, the very short length of an in–ice cascade does not allow the electrons and positrons to be accelerated enough by Earth's magnetic field to induce a noticeable current. Since Askaryan emission is radially polarized, the radio footprint of an in–ice cascade is expected to have a radial symmetry. In practice, since the radio emission from the air–shower also propagates into the ice, the total signal seen by an in–ice antenna will be the combination of both in–air and in–ice emission, resulting in a non–symmetric radio footprint.
Another difference, also due to the short length of an in–ice cascade, is that particles have way more chances to interact before decaying. This mostly impacts the muonic component of the in–ice cascade, since charged pion decay is the only muon production mechanism here.
The critical energy at which bremsstrahlung and ionization energy losses are equal highly depends on the media (see Eq. 16), and will be slightly smaller in the ice than in the air.
The last difference concerns the refractive index of the ice ($n \sim 1.79$) which is larger than the one of the air ($n \sim 1$). This will of course play a role in the propagation of the air–shower radio emission when entering the ice, but most importantly will modify the value of the Cherenkov angle. As will be seen in

Section 2.1, the radio waves are mostly coherent close to the Cherenkov angle of the media for both air–showers and in–ice cascades. The Cherenkov angle is defined as:

$$\cos\theta = \frac{1}{n\beta} \tag{24}$$

where n is the refractive index of the medium and $\beta = v/c \sim 1$. As a consequence, the radiation from an in–ice cascade is beamed at an angle $\theta \sim 56^{\circ}$ while the radiation from an air–shower is beamed at an angle $\theta \sim 1^{\circ}$. These values are not fixed since the refractive index of air changes with altitude and similarly, the refractive index of ice changes with depth.

Finally, showers in dense media do not really depend on the type of the primary particle, so that a neutrino and a proton initiated air–shower will provoke in–ice cascades with very similar properties. For this reason, the in–ice propagation of a cosmic–ray induced cascade is expected to perfectly mimic the tail of a UHE–neutrino induced particle cascade in the ice. Cosmic–ray particle cascades moving from air into the Polar ice represent thus a non–negligible background that has to be understood in order to discriminate between a CR and a neutrino signal for an in–ice detector such as ARA.

2 Radio Signal Properties

This chapter gives a brief overview of the radio emission properties from particle cascades in both air and ice. Radio footprints, defined as the energy carried by the radio waves and distributed along a surface, are discussed in general terms, since simulated footprints will be presented in chapter 3.

2.1 Coherence and Cherenkov–like Effects

An important aspect of radio wave emission is coherence, and the considerations below are independent of the emission mechanism. Both Askaryan and geomagnetic emission are produced by numerous emitters along the shower development. Due to the relativistic motion of the emitters, the emission is strongly forward–beamed. If the radiation from all those emitters has a negligible relative phase shift at a given frequency, the amplitudes will add up coherently to give a final signal whose amplitude is proportional to the number of emitters. This is an important feature to estimate the total energy of the shower since the number of emitters scales linearly with primary energy. When the signal is coherent, its amplitude then scales linearly with primary energy, and equivalently, the received power scales quadratically with the energy of the primary particle.

In theory, coherence is achieved when the wavelength is larger than the emission region. The bulk of the longitudinal profile of an extensive air–shower (see Fig. 5) can be a few hundred meters long. This would imply coherence is only achieved for frequencies below $\sim$ MHz but it is not the case, because what matters is the projected length scale and not the true length of the emission region.
Imagine that the radiation and the emitters travel at the same speed, the speed of light in vacuum. Then the radiation emitted along the shower axis will be completely synchronized with the emitters, and all the radiation emitted in a certain time interval $\Delta t'$ during the shower development will reach the ground at the same time t (see Fig. 13). Because of this, even if the emission region has a length $L' = c\Delta t' \sim 100$ m, the projected length $L = c\Delta t = 0$.

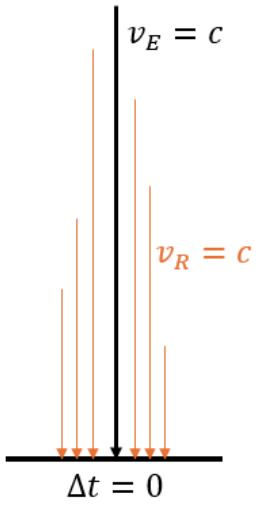

Figure 13: Schematic view of a relativistic emitter that is synchronized with its emission.

The radiation travels slower than the speed of light in vacuum because of the refractive index of the air. The speed of light in the air is c/n, where c is the speed of light in vacuum and n the refractive index of the air, which depends on the altitude. The radiation is therefore slower than the emitters, which travels roughly at the speed of light in vacuum. If we consider again an observer standing where the shower axis intersects the ground, the observer will receive the emission with a reversed time–ordering: the last signal emitted will arrive first and vice–versa.

Now if we consider an observer far from the shower axis, and a vertical air–shower to simplify, the radiation coming from different parts of the shower will arrive at different times. The radiation emitted at the top of the emission region is emitted sooner but travels at low speed over a longer distance, while the radiation emitted at the bottom has a shorter distance to travel in the air, but was emitted later. Let us consider that the emission region goes from $z = h$ to $z = 0$ and that an observer is located at $z = 0$ and at a distance $\mathbf{d}$ from the shower axis (see Fig. 14). Let $t = t_0 = 0$ be the time of emission of the first photon at $z = h$.

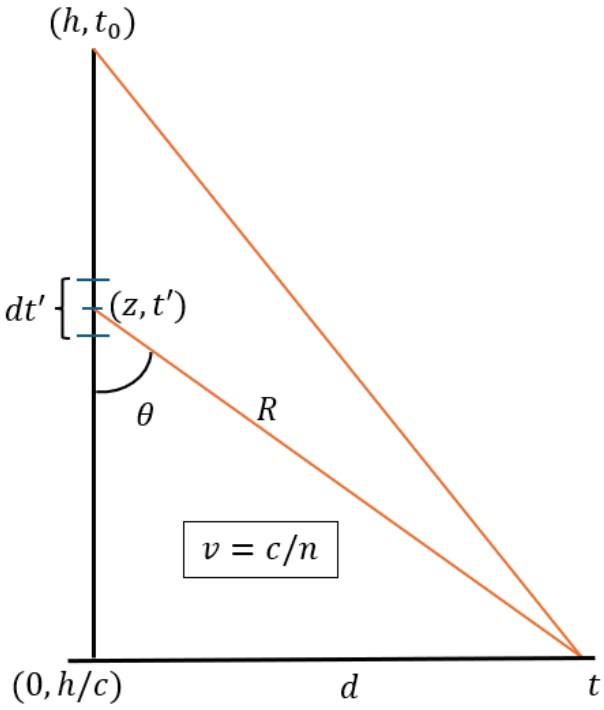

Figure 14: Scematic view of a relativistic emitter being faster than its own emission. This situation is the origin of all Cherenkov–like type of emissions.

We can compute the time of arrival of a photon at the observer location t as a function of its time of departure t'. We start from the relation:

$$\frac{c}{n}(t - t') = R = \sqrt{d^2 + z^2}$$

We can express z in function of t' knowing that the particles of the shower travel at a speed c:

$$z = h - ct'$$

By writing $ct = x$ and $ct' = x'$, we finally get:

$$x = x' + n\sqrt{d^2 + (h - x')^2}$$

and taking the derivative:

$$\frac{dx}{dx'} = 1 - n\frac{h - x'}{\sqrt{d^2 + (h - x')^2}}$$

that we can rewrite:

$$\frac{dx}{dx'} = 1 - n\frac{z}{R} = 1 - n\cos\theta$$

where θ is the angle between the shower axis and the photon direction. For photons emitted during a time interval dt' to arrive at the same time ($dt = 0$), the condition is:

$$\frac{dx}{dx'} = 0 \quad \Leftrightarrow \quad \cos\theta = \frac{1}{n}$$

The value of θ that verifies this relation is called the Cherenkov angle and plays an important role for the coherence of the signal. Indeed, for an observer located at the Cherenkov angle, the projected length L of the emission region is reduced to a negligible size, which means coherence is achieved for much smaller wavelength and therefore higher frequencies. The refractive index of the air is $n \sim 1.0003$ at ground which implies a Cherenkov angle of $\theta \sim 1°$. A higher refractive index of $n \sim 1.79$ in the ice gives a higher Cherenkov angle of $\theta \sim 56°$.

Now, since we only care about coherent emission, it means that we can consider the emission region as a small cylinder with typical projected dimensions of ~ 1 m in the air, which corresponds to frequencies below 100 MHz.
The dimensions of a particle cascade in–ice are obviously way smaller than the ones of an air–shower, allowing coherence to be achieved at higher frequencies of ~ 1 GHz, where higher frequencies often bring the advantage of lower background.

In reality, the effective thickness of the shower front depends on the observer angle, meaning that coherence is only achieved at higher wavelengths for an observer far from the shower axis (see Fig. 15). Measurements at lower frequencies therefore have the advantage of allowing larger observation angles.

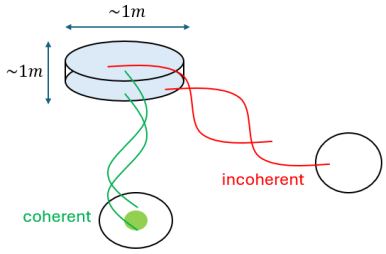

Figure 15: Impact of the width of the emission region on the coherence of the signal.

To summarize, coherence results in a very strong emission beamed in what we call a Cherenkov cone. Depending on the distance to the emission region, a radio antenna located at the right distance from the shower axis will receive a very strong signal compared to an antenna in the inside or the outside of the Cherenkov cone, where the contrast is even bigger at high frequencies. Note that this effect occurs for any coherent electromagnetic emission mechanism as it is a purely geometric effect and therefore is broader than classical Cherenkov emission[4]. We also expect time–ordering of the signal to be flipped inside the Cherenkov cone, where the last radiation emitted is the first to arrive. The typical radio pulse lengths expected go from 100 ns inside/outside of the Cherenkov ring to 1 ns on the ring location. Simulated radio pulses are presented in the next section.

2.2 Radio Footprint

When trying to represent the strength of the radio signal at a certain altitude or depth, we use a value called the fluence, which has the units of an energy per area:

$$\mathcal{F} = \epsilon_0 c_0 \int_{t_i}^{t_f} \left(E_x^2 + E_y^2 + E_z^2\right)\, dt \tag{25}$$

where $E_i[V/m]$ are the components of the electric field at the antenna position, the integration interval is $t_f - t_i \sim 100$ ns around the pulse and the integral has been multiplied by the speed of light in the vacuum ($2.99792458.10^5$ μm/ns) and the permittivity of the vacuum (55.26349406 $\mathrm{e^2eV^{-1}}\mu\mathrm{m^{-1}}$) to get units of [eV/m^2]. The radio footprint is then represented by the fluence distribution over a certain surface.

The radio signal of an air–shower, as measured by radio antennas on the ground, is the combination of geomagnetic and Askaryan emission. As the

[4]Emission produced by a (constant) net charge moving through a medium with a velocity which is higher than the speed of light in the medium.

geomagnetic emission has a directional polarization while the Askaryan emission is polarized radially inward, the resulting radio footprint on ground is asymmetric, as can be seen for a vertical shower in Fig. 16 with antennas 100 meters deep into the ice. The relative strength of the Askaryan effect to the geomagnetic effect **a** depends on the local magnetic field strength, the angle between the shower axis and the magnetic field, and additionally the depth of the shower maximum. One can estimate this relative strength by looking at the polarization of the radio signal or the asymmetry of the radio footprint on ground. Recent studies have given the following values [31]:

- AERA: $\mathbf{a} = (14\pm2)\%$ for $\mathbf{B} = 24\mu$T [30]
- Tunka-Rex: $\mathbf{a} = 8.5\%$ for $\mathbf{B} = 60\mu$T (based on CoReas simulations) [29]
- LOFAR: $\mathbf{a} = (3.3 \pm 1.0)\%$ for inclined air–showers to $\mathbf{a} = (20.3 \pm 1.3)\%$ for near-vertical showers for $\mathbf{B} = 49\mu$T [39]

We can see that the values vary a lot depending on the magnetic field strength and orientation at the location of the experiment, but the trend is that Askaryan emission is sub–dominant for air–showers. The footprint of the total emission close to the shower axis will thus be linear with a slight azimuthal dependence due to the weaker Askaryan effect. It results in a bean shape a bit displaced from the shower axis and whose size depends on the ratio **a**. The shape is seen on the left of Fig. 16.

The two major differences with the in–ice cascade is the emission process in play and the refractive index of the media. Since only the Askaryan effect participates to the emission in the ice, the emission footprint is symmetric, and since the Cherenkov angle is much larger in the ice, the coherent emission is seen further from the shower axis. It results in a ring of coherent emission that does not superpose with the in–air emission, as can be seen in Fig. 16.
Since both in–air and in–ice emission are strongly forward–beamed into a cone, the distance between X_{max} and the observation level has a strong influence on the size of the illuminated area[5] (as can be seen in [35]). The further X_{max} is from the ground, the broader the footprint will be. The radiated power will thus be more diluted and the average electric field amplitude will be lower. This distance to X_{max} mostly depends on the zenith angle, the primary energy and the primary type.

Note: Radio emission from natural showers in dense media has not been measured yet, so the knowledge about in–ice emission features comes from simulations based on the same principles as those for air–showers, which have been experimentally confirmed.

[5]This is especially true for air–showers but not as important in a media that has a high refractive index gradient, as will be seen in Section 3.2

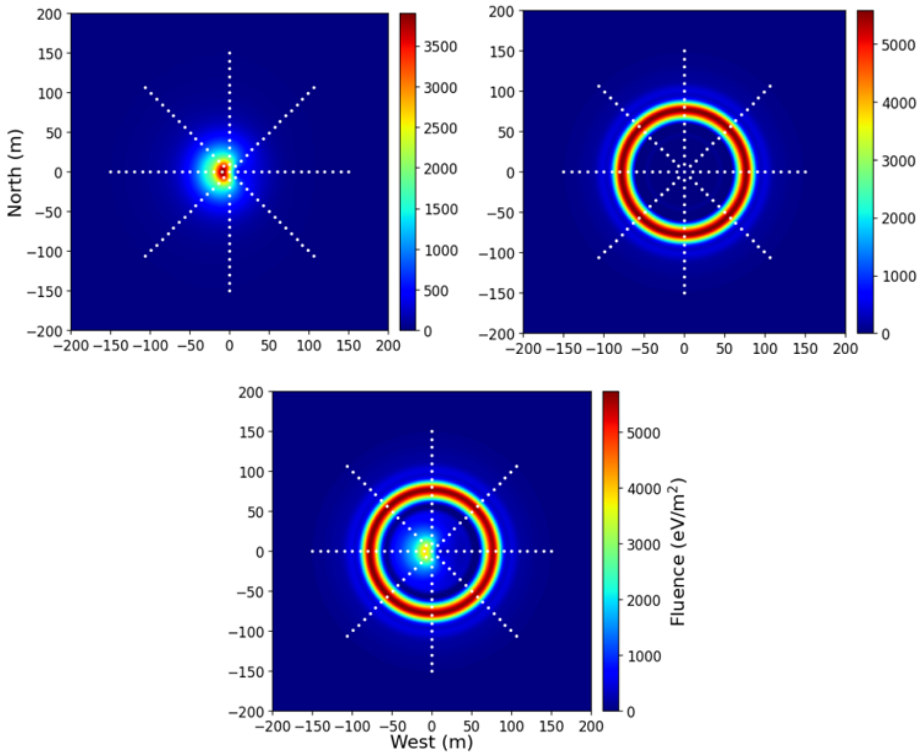

Figure 16: The fluence footprint of a simulated cosmic–ray induced shower at a depth of 100 m under the ice. **left**: in-air emission footprint, **right**: in-ice emission footprint, **bottom**: combined emission footprint. The primary energy is $E_p = 10^{18}$ eV and the zenith angle $\theta = 0°$. The simulation was performed using 121 antennas in a star-shaped grid with 8 arms and an antenna spacing of 10 m, indicated by the white dots. From [40]

3 Simulations

In this chapter we focus on the framework used for this work. As it would take too long to go into the details of each simulation code, we refer to the codes documentation for more information [41], [42], [43]. A few simulation results will then be presented to illustrate.

3.1 Framework

The framework used in this work is called FAERIE (Framework for the simulation of Air shower Emission of Radio for in-Ice Experiments) [40], and it is the first complete Monte–Carlo cosmic–ray radio emission simulation framework for in-ice detectors, including both the propagation of the particle cascade in air and in ice. This code was developed in Brussels at the ULB–VUB hosted Inter–university Institute for High Energies (IIHE).
The simulation setup goes in two steps. First, the cosmic–ray induced air–shower is simulated using CORSIKA 7.7500 [41, 44], which gives the particle content at ground level where the air–shower stops. The outputs of CORSIKA are then plugged into GEANT4 [45, 46, 43] which propagates the particles further into the ice. CORSIKA is used in parallel with a module named CoREAS [42, 47], the aim of which is to simulate the radio emission from each particle of the air–shower using the end–point formalism and propagate it down to the antennas with ray–tracing. The same formalism for radio emission and propagation is implemented in GEANT4. CoREAS has already been tested thoroughly by many experiments, but is restricted to using antenna positions on the ground. FAERIE uses a modified version of CoREAS that can handle antenna positions in ice by using full ray–tracing across the air–to–ice boundary.

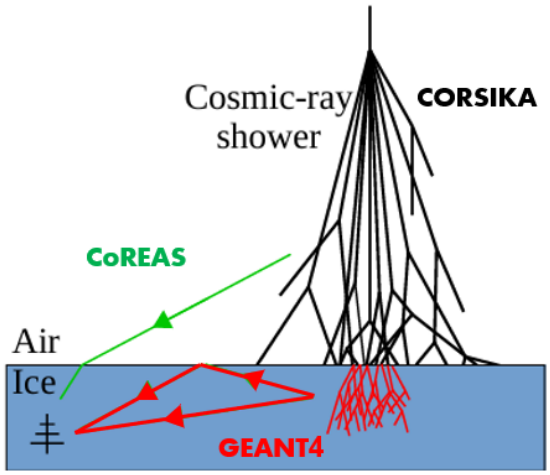

Figure 17: Scheme of the FAERIE simulation framework.

3.1.1 CORSIKA 7.7500

CORSIKA (cosmic–ray SImulations for KAscade) is a Monte Carlo program to simulate extensive air–showers initiated by high energy cosmic rays. It was developed in 1989 by the Karlsruhe Institute of Technology (KIT) in Germany, and it was originally designed for the KASCADE[6] experiment. It was originally made in FORTRAN only. CORSIKA allows to simulate interactions and decays of all hadronic and electromagnetic particles in the atmosphere up to energies of some 10^{20} eV, although the accuracy of the models drops at energies above 10^{18} eV due to uncertainties in the hadronic interaction models that probe energies above those that can be reached at LHC. It gives the type, the energy, the location, the direction and the arrival time of all secondary particles created by interactions in the atmosphere, as they reach a specified observation level. The program comprises four main components, three of which deal with low-energy hadronic interactions, high-energy hadronic interactions and the transport and interaction of electromagnetic particles. The fourth one performs the decays of unstable particles and tracks all the secondary particles taking into account ionization energy loss and deflection by multiple scattering and Earth's magnetic field. Several models exist for the three first parts and can be freely chosen when setting up the CORSIKA installation. The different models have varying precision and CPU–time consumption.

The different model options for high energy hadronic interactions are DPMJET [48], HDPM [49], QGSJET01 [50], SIBYLL [51, 52], VENUS [53], NEXUS [54], EPOS LHC (v3400) [55] and finally QGSJET II-04 [56]. For this study we use the QGSJET II-04 model (Quark Gluon String model with JETs) since it is one of the most recent and it is tuned to LHC data. It encompasses Pomeron-Pomeron interactions [57] and activates the inelastic hadron-nucleus interaction cross-sections at higher energies. The hadronization process is treated in the quark–gluon string model.

The low energy hadronic interaction models are FLUKA [58], GHEISHA [59] and UrQMD [60] which describe microscopically low energetic hadron–nucleus collisions. The model used here is UrQMD (Ultra–relativistic Quantum Molecular Dynamics). It performs the elastic and inelastic interactions of hadrons below 80 GeV in air. The UrQMD 1.3_cors version has been specially adapted to CORSIKA.

For the electromagnetic particles, two options are available: the adapted EGS4 code [61] or the analytic NKG formulae [62]. We decided to use the EGS code which is more accurate than NKG for e^- and γ at energies $> 10^{17}$eV, because NKG does not contain the LPM effect [63] (which is added to EGS4). This can alter the shower development, and thus the position of X_{max}, which has a large impact on the radio emission.

[6]European air–shower experiment located at the KIT campus (Germany) that aimed to study the cosmic–ray primary composition and the hadronic interactions from 1996 to 2013

CORSIKA also has a thinning option incorporated to speed up the simulations. Thinning allows to reduce the effective number of particles in the air–shower by combining low energy particles in a new "virtual" particle whose energy is the average of the initial particles energy.

The combined particles have to be under a specified energy threshold and originate from the same interaction. A "virtual" particle made of two "true" particles will carry a weight of two, and a maximum weight of typically 100 is set during the simulation.

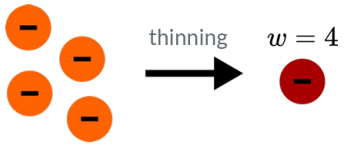

Figure 18: Thinning in CORSIKA. Credits to Simon De Kockere.

The coordinate system of CORSIKA is defined by Earth's magnetic field. It is a Cartesian axis system where the positive x–axis points to the magnetic North, the positive y–axis points to the West and the positive z–axis points towards the sky.

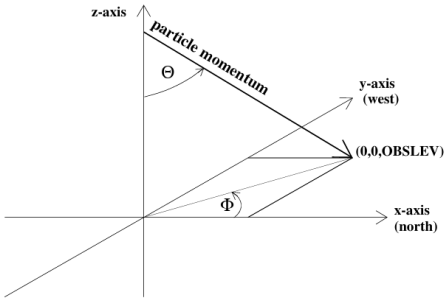

Figure 19: CORSIKA coordinate system. From [41]

The vertical origin (z=0) is set at sea level, and the coordinate (x,y)=(0,0) is defined by the shower core (intersection of the shower axis with the ground level). The zenith angle (Θ) of the event is the angle between the negative Z–axis and the shower axis, while the azimuth (Φ) is defined from the positive X–axis counterclockwise.

The density profile of the South–Pole atmosphere is a five–layer model fitted to a database used by the Global Forecast System (GFS), which is a National Center for Environmental Predictions (NCEP) in weather forecasting. It is expressed in vertical slant depth (g/cm^2). The four deepest layers are described by an exponential profile:

$$T(h) = a_i + b_i e^{-h/c_i} \quad \text{for } i = 1, 2, 3, 4 \tag{26}$$

while the uppermost layer density is given by:

$$T(h) = a_5 - b_5 h/c_5 \tag{27}$$

where the parameters a_i, b_i, c_i are displayed in Table 1. It is then trivial to get the density in a thin layer between h_1 and $h_2 > h_1$:

$$\rho(h) = \frac{T(h_1) - T(h_2)}{h_2 - h_1} \tag{28}$$

Since the first version in 1989, CORSIKA has been continuously extended and improved, as it is the most used air–shower simulation program in astroparticle physics. A fresh new version CORSIKA 8.0 is currently under development.

Layer	Altitude interval (m)	a_i (g/cm^2)	b_i (g/cm^2)	c_i (cm)
1	0 - 3217	-1.13352×10^{2}	1.19439×10^{3}	8.10969×10^{5}
2	3217 - 8364	-9.73769	1.10328×10^{3}	7.06357×10^{5}
3	8364 - 23142	-2.18461×10^{-1}	1.10964×10^{3}	6.86443×10^{5}
4	23142 - 100000	7.95615×10^{-4}	1.12499×10^{3}	6.82494×10^{5}
5	>100000	1.12829×10^{-2}	1.00000	1.00000×10^{9}

Table 1: Atmospheric density parameters used for the simulations. From [40]

3.1.2 CoREAS

CoREAS (Corsika-based Radio Emission from Air–Showers) is a Monte Carlo simulation for air–shower radio emission. As its name suggests, it has been specially made to work with CORSIKA. It computes the electromagnetic radiation of each particle simulated by CORSIKA using the end–point formalism [64]. CoREAS has already been tested thoroughly and is used in many experiments.

The endpoint formalism describes particle motion as a series of instantaneous accelerations and decelerations from/to rest along the particle track. Each acceleration and deceleration of a charged particle (of charge **q**) is seen as a separated event producing radiation. The electric field components for each event are computed from the Liénard–Wiechert potentials:

$$\Phi(\vec{x},t) = \left[\frac{q}{(1-n\vec{\beta}.\hat{r})R}\right]_{t-nR/c} \tag{29}$$

$$\vec{A}(\vec{x},t) = \left[\frac{q\vec{\beta}}{(1-n\vec{\beta}.\hat{r})}\right]_{t-nR/c} \tag{30}$$

where R is the distance from the emission point to the observer and $\hat{r}$ is a unit vector in the direction of the observer. From these potentials, one can sum the contributions from individual charges in a distribution of source charges to compute the total vector potential. The electric field can then be inferred from the total potentials and contains a near–field term ($\propto 1/R^2$) and a radiation term ($\propto 1/R$). While the electric field $\vec{E}(\vec{x},t)$ can diverge in the case of instantaneous acceleration, the time–integrated electric field is finite. After integrating and neglecting the near–field term we get the time–averaged electric field over a time–scale Δt:

$$\vec{E}_{\pm}(\vec{x},t) = \pm\frac{1}{\Delta t}\frac{q}{c}\left(\frac{\hat{r}\times\left[\hat{r}\times\vec{\beta^*}\right]}{\left(1-n\vec{\beta^*}.\hat{r}\right)R}\right) \tag{31}$$

where + refers to when the acceleration vector ($\dot{\beta}$) is parallel (acceleration) to the velocity vector (β), and - refers to the anti–parallel case (deceleration). $\Delta t = t_1 - t_0$ is the sampling time interval of the observer and $\vec{\beta^*}$ is the velocity of the particle during the step. Δt corresponds to the retarded window $t'_1 - t'_0$ that delimits the event. For an acceleration, the particle is at rest at time t'_0 and has a velocity $\vec{\beta^*}$ at t'_1. In practice, Δt is chosen depending on the time resolution of interest.
Note that the end point formalism does not make any assumption on the emission mechanism. More information on the end–point formalism can be found in [64].

In the end–point formalism, the rays are supposed to travel in a straight line from the emission point to the observer along the $\hat{r}$ direction. Furthermore, CoREAS only handles in–air propagation which is not enough if we are interested in simulating antennas buried deep into the ice. Also, while straight line propagation is a good approximation in the air where the refractive index stays close to unity between X_{max} and the ground, it is completely false in the South–Pole firn[7], which goes from the surface to 200m depth and where the refractive index goes from 1.35 at the surface to 1.78 in the first $100 - 200$ m, inducing a significant ray–bending. A modified version of CoREAS is therefore needed, and was made by Uzair Latif and Simon De Kockere [38], from VUB. The modified CoREAS allows antenna positions in the ice using full ray–tracing. Ray tracing is the procedure of tracing the trajectory of radio waves traveling through a given media, and/or passing the boundary of two different media [40]. The updated version of CoREAS takes into account the gradient of the index of refraction in both air and ice, as well as the transition of the radiation from air to ice. It does so analytically by using an exponential profile for the refractive index of the air and another for the ice. The Earth is assumed to be flat and the refractive index profiles only depend on the vertical coordinate. Typical profiles for the atmosphere and the ice at South–Pole were adopted for this work. The refractive index of the atmosphere is modeled by five exponential profiles:

$$n(z) = 1 + B_i e^{-C_i h} \tag{32}$$

where the parameters B_i, C_i are displayed in Table 2. The refractive index profile in the ice is given by [65]:

$$n(z) = 1.78 - 0.454 \exp\left(-(0.0202 m^{-1})|z|\right) \tag{33}$$

In this modified version of CoREAS, Eq. 31 stays the same but the parameters have a different meaning. Indeed, the variable R in Eq. 25 refers to the geometrical distance between the emitter and the receiver. It is now interpreted as the optical path length of the ray, which is different from the distance between

[7]Layer of the South–Pole between 0 and 200m depth, made of accumulated snow slowly compacting into ice over the course of many years.

emitter and receiver because of ray–bending. This implies in particular that the relation $t = t' + nR/c$ still holds. In the end–point formalism, $\hat{r}$ points directly from the emitter to the receiver, and is now interpreted as the launch direction of the ray. The angle between the vertical and $\hat{r}$ is referred to as the launch angle. Since in the presence of ray–bending the launching direction does not correspond to the arrival direction of the ray at the receiver, the electric field is rotated so that its components arrive perpendicular to the receiver direction.

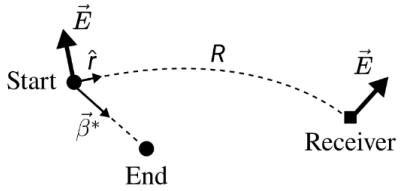

Figure 20: Rotation of the electric field during ray–tracing. From [40]

Ray–tracing now allows us to use CoREAS with in ice radio antennas, but considering the number of emitters in a typical air–shower $\mathcal{O}(10^9)$, using ray–tracing directly during the CORSIKA simulation can take weeks or months at EeV energies. To speed–up the process we thus use interpolation tables. Since the refractive index profile only depends on depth, two receivers at a same depth are equivalent from a ray–tracing point of view. Therefore, ray–tracing solutions are pre–simulated in interpolation tables that are made for different emitter positions distributed in a 2D grid, one for each depth. The 2D grids are filled with vertical and horizontal distances to the receiver. When simulating the air emission towards a certain receiver position in the ice, the code looks at the interpolation table with the closest depth and find the ray–tracing solutions from each emitter position by doing a linear interpolation in the 2D grid. This way the code does not have to re-calculate the ray–tracing solutions, it only has to find the corresponding pre-calculated ones. For any given receiver depth, the associated 2D grid goes from the ground level up to 100 km altitude and the horizontal extension of the grid is obtained by varying the ray launch angle at $z = 100$ km from 0° (vertically down) to 89.9° (almost horizontal).

Now, when calculating the electric field amplitude at a receiver location in the ice, one has to be very careful with the behaviour of the rays at the air–ice boundary. Indeed, the air–to–ice rays will be partially reflected when reaching the ground, which translates in a decrease of the signal amplitude described by the Fresnel coefficients. By defining the reflection coefficients r_ϕ and r_θ for the two components of the electric field perpendicular to $\hat{r}$, the final electric field corrected for the reflection at the boundary is given by:

$$\vec{E}_C = (\hat{r}.\vec{E})\hat{r} + r_\phi(\hat{\phi}.\vec{E})\hat{\phi} + r_\theta(\hat{\theta}.\vec{E})\hat{\theta} \tag{34}$$

These modifications can be applied directly at the receiver since they only represent a re–scaling of the electric field.

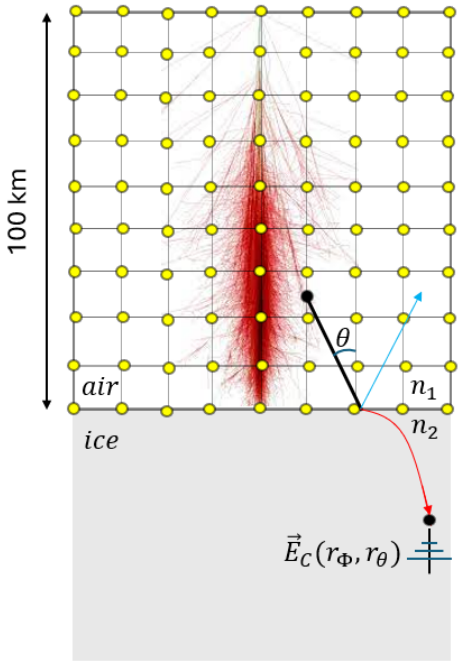

The Fresnel coefficients are given by the Snell's law and they only depend on the refractive index of the two media and the angle θ between the ray and the normal on the interface.

Figure 21: Schematic view of an interpolation table for the in–air part. The yellow dots represent possible emitter position and ray–tracing solutions are calculated from each dot to each antenna depth, taking into account the Fresnel coefficient by a re–scaling of the electric field at the antenna.

Lastly, in case of bent trajectories a convergence or divergence of the rays is expected at an antenna. The ray density increases in case of a convergence and so does the amplitude of the signal, while the opposite effect occurs in case of a divergence. Since the simulated antennas have no spatial extension, no convergence or divergence of rays can happen in the simulations. The simulated amplitudes are therefore multiplied by a focusing factor calculated with the same procedure as described in [66].

Layer	Altitude interval (m)	B_i	C_i (m^{-1})
1	0 - 3217	3.28911×10^{-4}	1.23309×10^{-4}
2	3217 - 8364	3.48817×10^{-4}	1.41571×10^{-4}
3	8364 - 23142	3.61006×10^{-4}	1.45679×10^{-4}
4	23142 - 100000	3.68118×10^{-4}	1.46522×10^{-4}
5	>100000	3.68404×10^{-4}	1.46522×10^{-4}

Table 2: The atmospheric index of refraction parameters used for the simulations in this work. From [40]

3.1.3 GEANT4

GEANT4 is a toolkit that allows to simulate the passage of particles through any given media. In our case it is used together with CORSIKA to simulate the in–ice cascade from the particle content of the air–shower at ground level. After

propagating the particles of the air–shower in the ice, GEANT4 uses its own physics models to describe all the particles interactions over a very wide energy range, depending on the specified density profile of the ice. The ice density profile is cut in 1 cm–thick horizontal layers, and the profile used here is [67]:

$$\rho(z) = \rho_{ice} - (\rho_{ice} - \rho_{surface}) \exp\left(-\frac{1.9}{t_{firn}}|z|\right) \tag{35}$$

with $\rho_{ice} = 917$ kg.m^{-3}, $\rho_{surface} = 359$ kg.m^{-3} and $t_{firn} = 100$ m.

As already discussed in Section 1.6, the particles far from the shower core are not expected to induce a cascade in the ice and as can be seen in Fig. 12, one can consider only the particles within a 1 m radius from the shower core when simulating the in–ice cascade. Once the CORSIKA simulation is over, all the particles at ground level and within a 1 m radius from the shower core are thus transmitted to GEANT4 which propagates them in the ice.

The radio emission of the in–ice cascade is also simulated via the end–point formalism, and all the considerations discussed above for CoREAS apply to GEANT4 as well, with a few differences that are discussed below. Note that the refractive index profile of the ice used in GEANT4 does not depend on the layered density profile, and is given in our case by Eq. 33.

For ice–to–ice ray propagation, ray–tracing generally finds two different solutions: a direct path and an indirect one. The indirect one can be either a refracted ray with a ray path longer than the direct one, or a ray reflected on the air–ice boundary, as shown in Fig. 22.

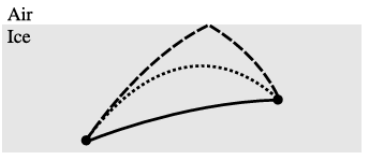

Figure 22: The different ray–tracing solutions. From [40]

Since all the emitters are typically contained in a box of 20 m, the interpolation tables of the in–ice emission are way smaller than for the in–air case, and one table is made for every receiver position even if they are at the same depth.

In the case of ice–to–ice rays reflected on the air–ice boundary, the decrease of electric field amplitudes can be described with Fresnel coefficients as for the air–to–ice case, by replacing r_ϕ and r_θ in Eq. 34 by the transmission coefficients t_ϕ and t_θ. The transmission coefficients verify:

$$t_\phi = 1 + r_\phi \tag{36}$$

$$t_\theta = (1 + r_\theta)\frac{n_1}{n_2} \tag{37}$$

Another process to take into account is the transition radiation, which is another type of free–electron radiation emerging from particle–matter interactions. It occurs whenever a charged particle moves across an inhomogeneous region such as an optical interface irrespective of the velocity of the particle. Here

this process is divided in two steps: First CoREAS simulates the sudden death emission when electrons reach the ground, then GEANT4 simulates the sudden appearance emission in the ice. The combination of both gives the transition radiation.

Lastly, to speed up the simulations, only the electromagnetic interactions are simulated, which gives almost identical results for the radio emission (see Fig. 3 and Fig. 4 of [68]).

3.2 Simulation Results

The inputs used for all the simulations can be found in Appendix A.

As already mentioned above, a CORSIKA simulation gives the particle content at ground level. Fig. 23 shows the ground particle energy distribution of a vertical air–shower initiated by a 10^{17} eV proton, just before GEANT4 propagates the particles into the ice. To visualize separately the distribution of high and low energy particles when going further away from the shower axis, several cuts in particle energy have been made. The black line on the top–left plot represents the increase of the particle footprint total energy when increasing the size of the considered region. It is therefore a cumulative plot. The yellow line represents the particle footprint energy when only summing the energies of the particles with $E_{part} > 10^{11}$ eV. We see that up to a 50 cm region, the total energy of the footprint is very well described by considering only the very high energy particles. The opposite cuts are displayed on the right, where we can see that the particles with $E_{part} < 10^{8}$ eV bring a negligible contribution to the total energy. Remember that we only propagate in the ice the particles within a 1 m radius from the shower axis. The validity of this approximation is not very clear if we look at the top–left graph, since the total energy continues to increase above 5 meters. This is because a lot of energy is carried by lower energy particles far from the shower axis, as can be seen in the middle plots.

The middle plots show the distribution of the number of particles with the same energy cuts as given above. Note, by looking at the yellow line on the left, that the number of high energy particles is very low compared to the low energy ones, and that it stays approximately constant when increasing the size of the considered region. It means that all the very high energy particles are well contained in the first 1 m from the shower axis. These particles are the ones that are able to cascade in the ice and produce the energy density profile displayed in Fig. 12. Although low energy particles continue to increase the total footprint energy at larger distances due to their large number, the main contributors of the in–ice cascade are thus confined in a very small region around the shower axis and there would be no benefits to propagate a bigger portion of the particle footprint into the ice.

Finally, the bottom plots show the mean energy per particle as the size of the considered region is increased. It simply represents the top plots divided by the middle ones. Note that the high energy particles contained in a region of 1 m radius from the shower axis have a mean energy of 10^{12} eV. Note also that the mean energy of these particles quickly decreases when increasing the radius from 1 m to 2 m where it flattens due to the lack of new high energy particles.

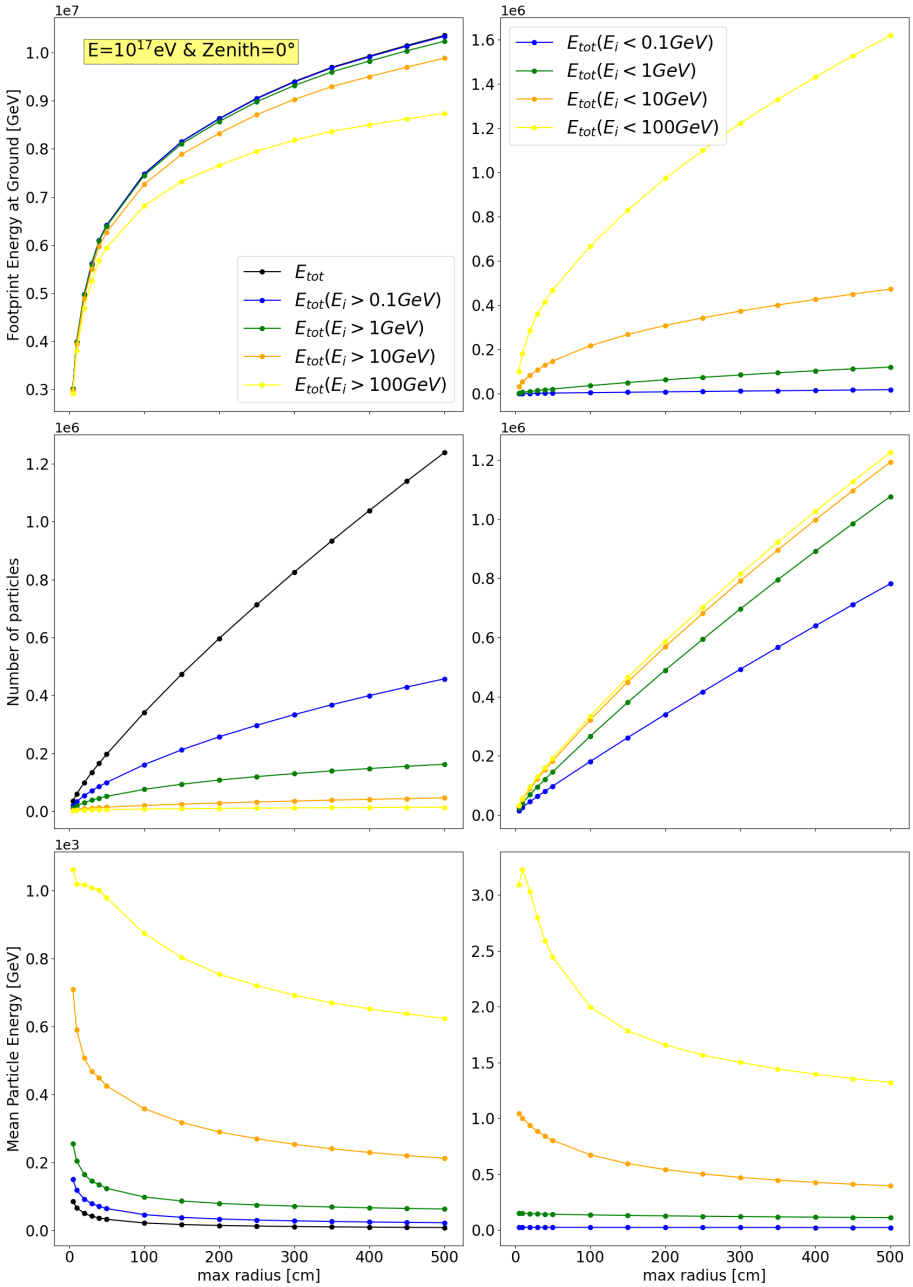

Figure 23: **(top)** Sum of particles energy at ground level depending on the radius of the region considered (cumulative plot). Different particle energy cuts are used to show the contribution of low and high energy particles to the total energy. **(middle)** Number of particles at ground level with the same particle energy cuts. **(bottom)** Mean energy per particle at ground level (upper plots divided by middle plots).

Fig. 25 shows three simulated fluence plots for three different zenith angles for an observation level at 160 m depth and for a primary cosmic–ray energy of $10^{17.5}$ eV. The difference with Fig. 16 is that no interpolation is used between the antennas. Interpolation can be used with symmetric footprints to reduce the number of antennas simulated by applying a linear scaling between the antennas. It can be achieved as in Fig. 16 with a star–shape antenna grid or any grid featuring a polar symmetry, since the code uses polar functions [69]. While it can handle small asymmetries as the bean shape in Fig. 16 caused by the combination of the Geomagnetic and Askaryan effect, the code does not work properly when footprints become globally elliptic, as for non–vertical showers. Since we want to simulate non–vertical showers we thus have no choice but to simulate a large number of antennas very close from each other in order to capture most of the emission. The antenna spacing used here is 20 m and the number of antennas on each grid is respectively 361, 361 and 506 from top to bottom. The reasons for these particular grid geometries are explained in detail in Section 5.1. We can already understand that different grids are needed depending on the zenith angle. There are two reasons for that: The first is that the air component of radio footprint gets bigger when increasing the zenith angle as seen in the bottom plot for 50°. This is because the source of emission, i.e. the X_{max} of the shower, is further away for a very inclined air–shower, since it develops higher in the atmosphere. The grids have thus to grow accordingly. The second reason is just a trigonometric effect. For a same impact position on the ice surface, the emission of an inclined shower at a certain depth will be shifted compared to the one of a vertical shower.

The top plot is very similar to Fig. 16 since they are both for a vertical air–shower. We can see the Cherenkov ring of the in–ice emission with a radius ~ 100 m, surrounding the in–air emission in the center. As already mentioned, increasing the zenith angle implies less particles of the air–shower reaching the ground and cascading in the ice. We can see this effect here by looking at the decreasing in intensity of the ice Cherenkov ring from the top plot to the middle one, and its disappearance in the bottom plot.
Note that because of the antenna spacing and the small width of the in–ice emission Cherenkov ring, the peak of the emission can leak through the grid in some cases by falling right between two antennas. This is especially true for small zenith angles where the ice Cherenkov ring is very well defined. This leaking effect can be seen on Fig. 24 which shows the total radio footprint energy as a function of depth. Since we have a discretized set of antenna positions, the total radio footprint energy was calculated by summing the fluence of each antenna and multiplying by the total area of the grid:

$$E = \left(\sum_{ant \in \mathrm{GRID}} \mathcal{F}_{ant} \right) \cdot A_{\mathrm{grid}} \tag{38}$$

The sum was calculated separately for the in–air emission (left) and the in–ice emission (right). The decreasing of the total in–air emission energy with depth

can be understood the following way: As the depth increases, the radio footprint becomes bigger and bigger, but the same antenna grid was used at each depth (see Section 5.3 for more details about the simulations). It means that more and more energy is lost by not increasing the grid size with depth. This lost energy is however irrelevant for radio detection since what matters is the individual signal amplitude at each antenna position. For the in–ice emission total energy (right plot) we can see huge fluctuations of $\sim 25\%$. This is due to the leaking effect caused by the antenna spacing. Since the radius of the Cherenkov ring increases with depth, it can either fall right on the grid antennas or just between them, meaning that the total energy captured by the grid depends on the depth and on the antenna spacing.

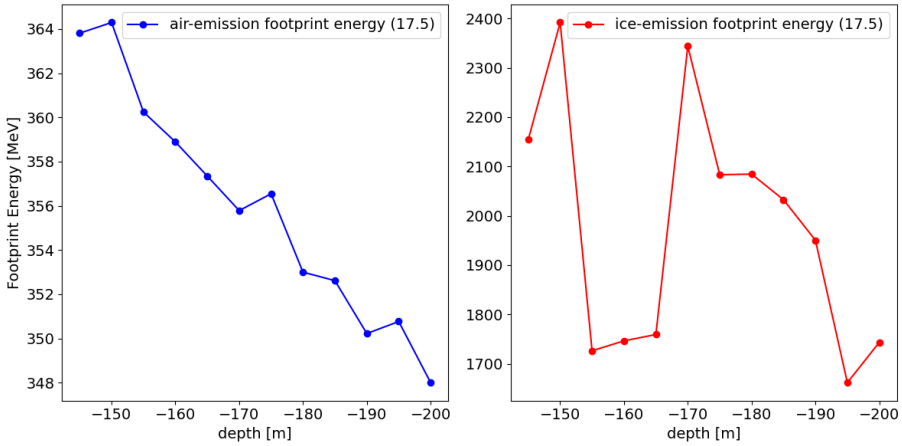

Figure 24: Fluence integrated over the footprint at different depths. The primary energy is $10^{17.5}$ eV and the zenith angle is 0. **left:** only the air–emission energy. **right:** only the ice–emission energy.

The values of X_{max} for these simulations (Fig. 25) are 715 g/cm^2, 725 g/cm^2 and 755 g/cm^2 from top to bottom. Since the slant–depth is calculated along the shower axis (see Fig. 6), only the value for the vertical shower (715 g/cm^2) can be compared to the ground level (see Appendix A). We see that the X_{max} of a vertical air–shower at $10^{17.5}$ eV is only $\sim$ 15 g/cm^2 above the ground, modulo shower–to–shower fluctuations. This is due to the very high altitude of the South–Pole ice sheet and it explains why the in–air emission footprint is so small ($\sim$ 50 m radius). To compare the X_{max} values of inclined air–showers to the ground level, we must calculate the slant–depth of the ground level along an inclined trajectory. This is done by dividing the vertical slant–depth by $\cos\theta$ (see Eq. 22). For a zenith angle of 30° it gives 842 g/cm^2 to compare with $X_{max} = 725$ g/cm^2 (middle plot). For 50° it gives 1134 g/cm^2 to compare with $X_{max} = 755$ g/cm^2 (bottom plot). This confirms that the source of the emission is way further for increasing zenith angle and explains the broadening of the in–air emission footprint as seen in Fig. 25.

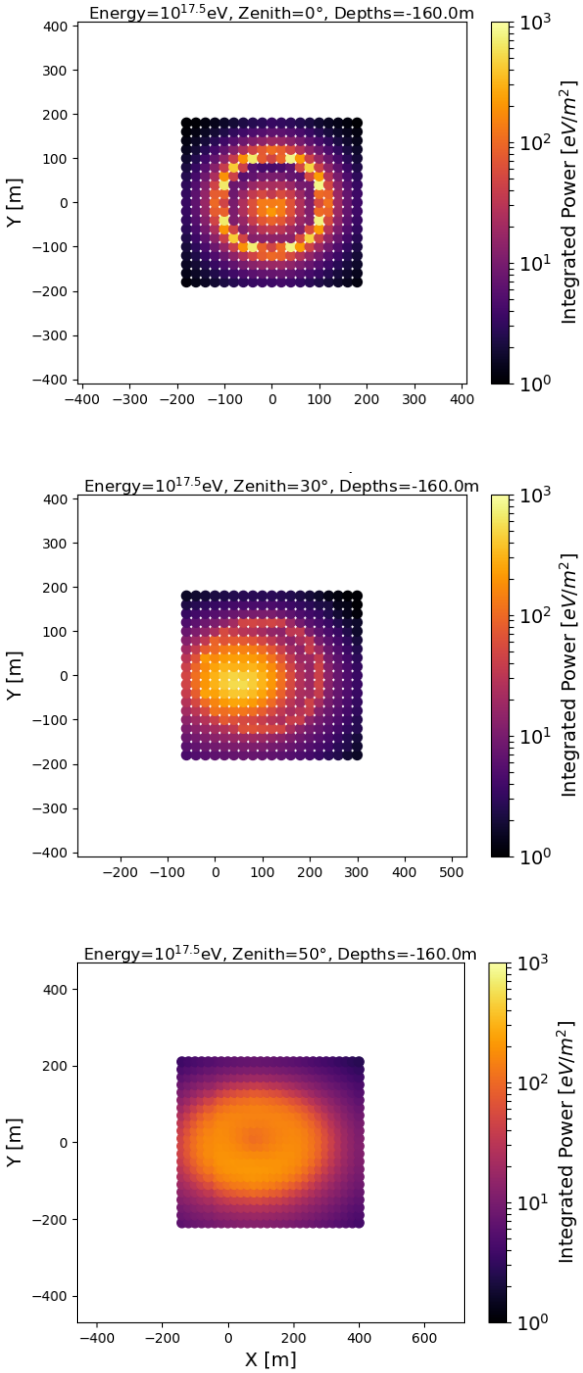

Figure 25: Radio footprints at 160 m depth for a proton primary with energy $10^{17.5}$ eV and zenith angle 0° (top), 30° (middle) and 50° (bottom). Other simulated fluence plots can be found in appendix B.

The electric fields used to calculate the fluence of two different antennas in Fig. 25 (top) are shown in Fig. 26. The in–air (blue) and in–ice (red) emission are displayed separately. The left plots correspond to the electric field components seen by an antenna at ($x = 20$ m,$y = 0$ m), while the right plots are from an antenna at ($x = 100$ m,$y = 0$ m). By comparing with the upper plot of Fig. 25 we see that the first one is right in the part of the footprint where in–air emission dominates, and the second one is inside the Cherenkov ring of the in–ice emission.

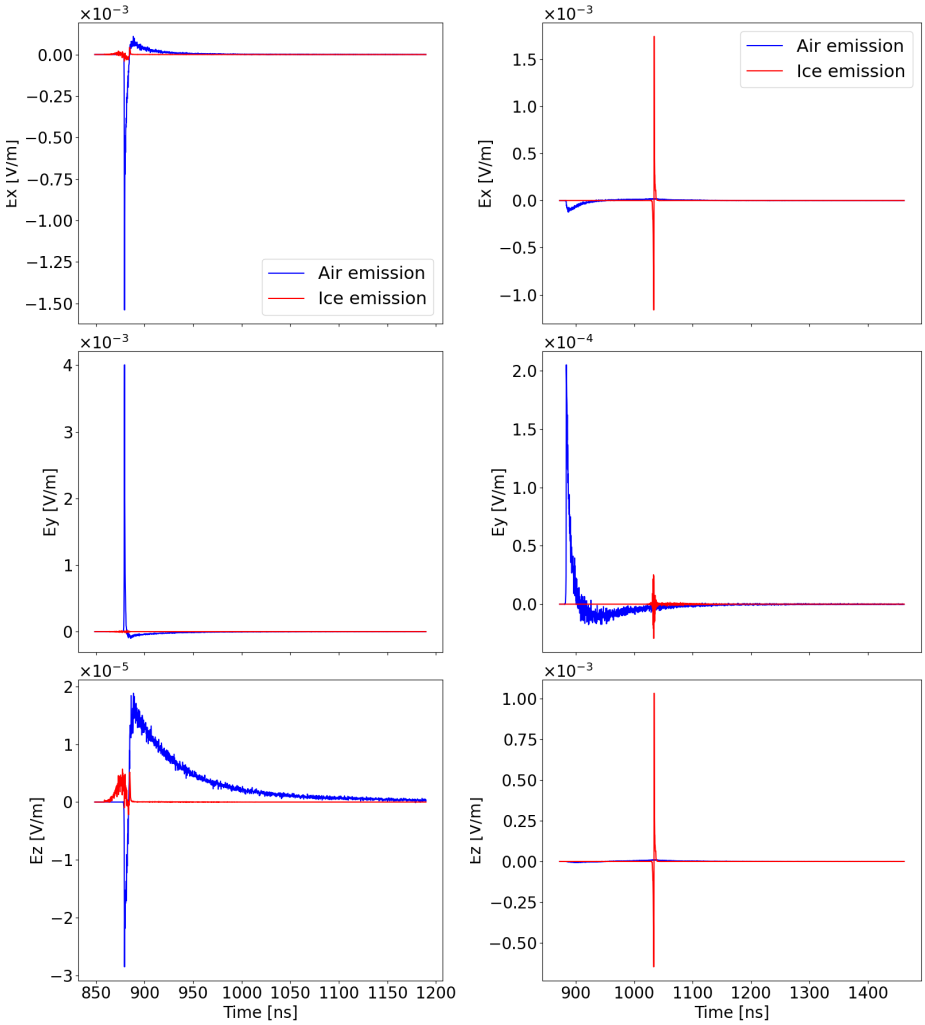

Figure 26: Evolution of the electric field in two different antennas for a vertical air–shower at $10^{17.5}$ eV. The in–air emission is displayed in blue and the in–ice emission in red.
left: Antenna in (x=20 m,y=0,z=-160 m).
right: Antenna in (x=100 m,y=0,z=-160 m).

The first observation is that the signals are very peaked in both antennas. This happens when all the emission arrive at the antenna position almost simultaneously. This is due to the effect described in Section 2.1, resulting from the maximum coherence of the emission being reached at the Cherenkov angle of the media.
Note also the reversed order of time–of–arrival of the in–air/in–ice emission between these two antennas. This effect was also described in Section 2.1 and is due to the faster travel speed of the emitters compared to the light in the air and the ice.

Another less evident effect that can be seen in Fig. 25 is the ray–bending in the ice. Indeed, we can use a simple geometric argument to guess where the radio footprint would have been located at -160 m depth if the emission traveled in a straight line. For a zenith angle of 30°, the emission should have been centered around $160 \times \tan(\theta) = 92$ m and for a zenith of 50°, the footprint center would have been at 191 m. Ray–bending tend to make the emission go downwards, as can be seen in Fig. 27.

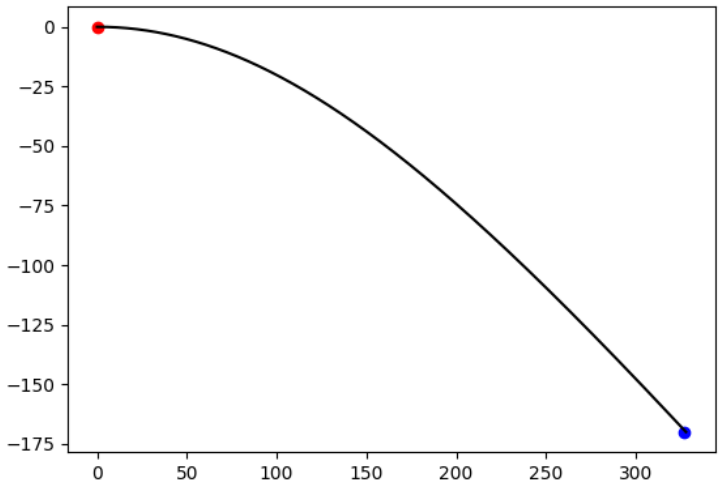

Figure 27: Representation of ray–bending in South–Pole ice with an almost horizontal launch angle. Credits to Abby Bishop

This effect is more clear in Fig. 28 where the distance from the shower axis of the in–ice emission maximum (i.e. the radius r_{max} of the Cherenkov ring) has been calculated at several depths (left). The fits make it look like the rays travel in straight line but the fitted line makes an angle of 35° with the vertical which is too small for a Cherenkov emission in the firn. Indeed, even at its lowest density, i.e. closest to the surface, the Cherenkov angle in the firn would be over 42°. As can be seen in Fig. 27, the regime between -100 m and -200 m

depth is close to a straight line propagation, while most of the bending occurs in the first 100 m. The right plot of Fig. 28 shows the apparent Cherenkov angle of the in–ice emission assuming straight line propagation between ($x = 0$,$z = 0$) and ($x = r_{max}$,$z = -160$ m), the fluctuations being caused by the antenna spacing again. A fit of the index of refraction in the firn can be found in [70].

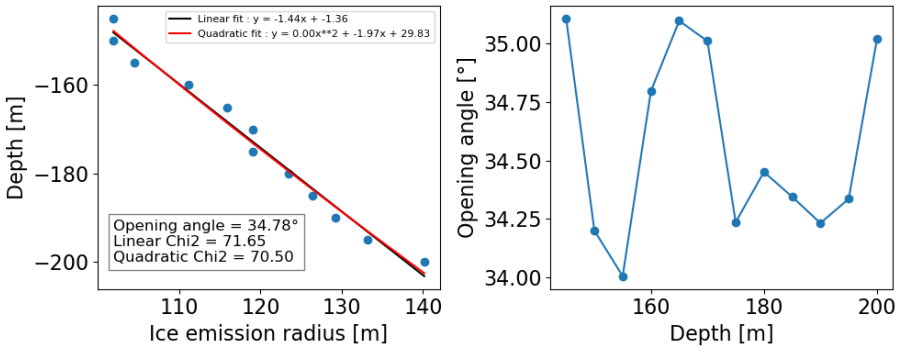

Figure 28 (for a vertical shower at $10^{17.5}$ eV) left: Radius of the in–ice emission Cherenkov cone at different depth, with a linear and a quadratic fit. **right:** Apparent opening angle of the in–ice emission Cherenkov cone.

4 The Askaryan Radio Array

The Askaryan Radio Array is a neutrino detector deployed at the South–Pole, just a few kilometers away from IceCube. ARA is currently made of 5 stations, each composed of 16 radio antennas of different polarization buried in the ice between -145 m and -200 m. Having antennas with different polarization allows to reconstruct the neutrino direction.
Each station is named following the order it was deployed, going from ARA1 to ARA5. The newest station ARA5 has two separate but connected detectors, as seen in Fig. 31. The first one, referred as the baseline system, follows the same design as the other ARA stations. The second, called the Phased Array, is a single string with its own trigger instrument added in the center of ARA5. The Phased Array and the baseline system are connected but they possess two separate Data Acquisition (DAQ) systems and operate thus as independent detectors. The Phased Array is meant to significantly improve the performance of the station.

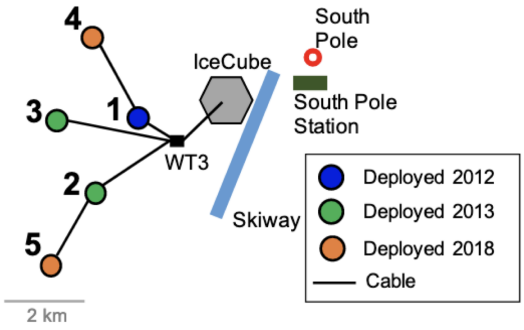

Figure 29: A diagram of the ARA layout with the year of deployment of each station. From the ARA collaboration

The spacing between two stations is about 2 km, which is enough to make sure that a neutrino–induced signal can only be seen by one single station given that the attenuation length of radio waves in the ice is ~ 1 km. As ARA aims to detect the first UHE–neutrino, this choice was made to maximize the effective volume. With this choice, each station works as an independent detector and the number of events is thus proportional to the number of stations.

4.1 ARA Station Layout

The structure of a typical ARA station is shown in Fig. 30. The 16 radio antennas of one station are divided in 8 HPols (horizontally–polarized antenna) and 8 VPols (vertically–polarized antenna), distributed along four different vertical strings. Each string is connected to two VPols and two HPols. The four radio antennas of one string are again divided in two sub–groups: one HPol and one VPol only 1 m away at around −165 m depth (Top HPol and Top VPol in Fig. 30), and the other two antennas, also 1 m away, at around −200 m depth (Bottom HPol and Bottom VPol). This design was chosen to take advantage of the ray–bending occurring in the firn. Since the rays are bent downwards, a same instrumented area deeper in the ice will have an increased chance of intercepting a neutrino signal, increasing thus the effective volume of detection. Going under 200 m depth would be very expensive since it would require to drill in a pure ice layer and it would not drastically improve the effective volume as the refractive index stabilize from −200 m downwards (see Fig. 27). Finally, the separation between adjacent strings is about 15 m in ARA1,2,3 and around 30 m in ARA4 and the baseline system of ARA5.

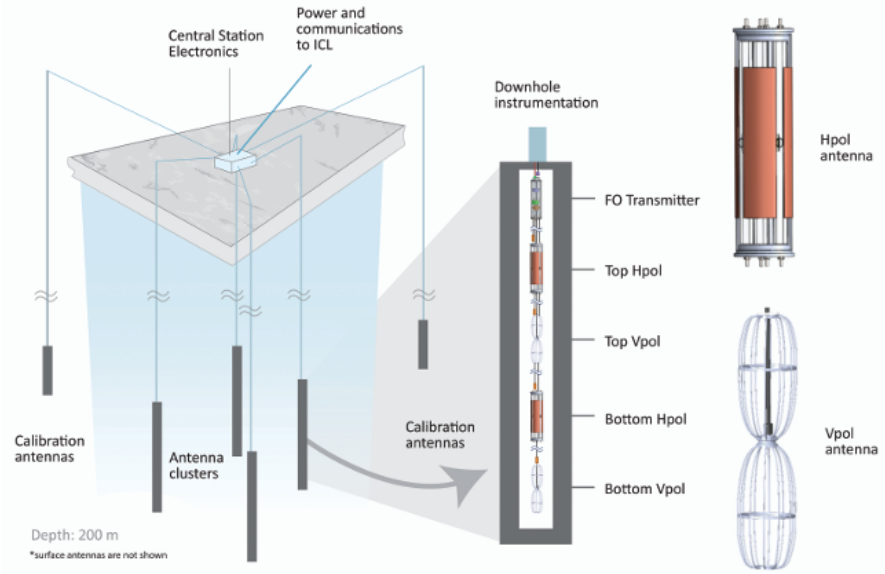

Figure 30: A diagram of a typical ARA Station, including close-up views of the VPol and HPol antennas. From [65]

The small diameter of the holes (∼ 15 cm) make the HPol antennas much harder to design than VPol antennas because their radial length, and thus their gain, is very limited. On the other side, the vertical length of a VPol not being restricted by the geometry of the hole, it can be freely chosen to reach the desired gain.

Finally, for the reasons explained in Section 2.1, in order to be sensitive to neutrino–induced Askaryan emission in the ice, ARA antennas are designed to be sensitive to frequencies between 200 and 850 MHz.

4.2 Phased Array

The Phased Array is a supplementary string deployed in the middle of the four strings of the baseline system of ARA5 and connecting seven VPols antennas and two HPol antennas together. The seven VPols are spaced by 1 m from each other, between -172 m and -180 m, and are meant for triggering. The two HPols below were installed for reconstruction purposes.

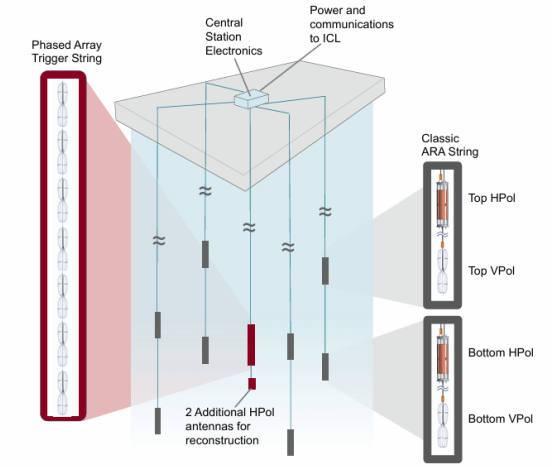

Figure 31: Example of a one-dimensional vertically-spaced Phased Array, surrounded by additional antennas used for reconstruction. From [71]

The idea behind the Phased Array is to improve the total gain by phasing multiple antennas together. Indeed, after applying the appropriate time delays depending on the direction of the incoming emission, the signals from each antenna will add up coherently whereas the noise will add incoherently. The Phased Array scans over the full sky forming several beams in pre–defined directions, prior to any trigger decision, in order to cover all possible incoming neutrino directions.

The gain of an array of N antennas having each a gain G and arranged closely along a single dimension is then given by:

$$G_{array} = 10 \times \log_{10}\left(N \times 10^{\frac{G}{10}}\right) \tag{39}$$

and we have $G_{array} > G$ as long as $N > 1$. Having a higher gain means the effective volume is also increased for neutrino detectors. The Phased Array trigger is now the baseline design for current and future radio experiments.

4.3 ARA Status

As of today, no neutrino has been observed in ARA but it could happen in a near future thanks to the ongoing analysis. Although the first ARA stations were deployed a decade ago, no data analysis has been performed yet due to a lack of manpower for calibrating the detector. Now that each station has been calibrated, all the data accumulated during this past decade is ready for analysis. However, the five ARA stations have not been working permanently since their deployment due to the difficulty of sending people in Antarctica for maintenance and reparations. Combining the data recorded by every station, a dataset equivalent to 25 station–years is stored and ready for a combined analysis. The ARA collaboration is actively working to find the first UHE neutrino in this consequent dataset.

Unfortunately, the ARA5 baseline system had to be turned off in 2020 after its DAQ was damaged. Since each ARA DAQ has 16 entries, seven antennas of the baseline system were thus added to the Phased Array DAQ, together with the nine antennas of the Phased Array string. These seven antennas from the baseline system are, since then, used for reconstruction, and do not participate to the trigger decision.

For the analysis presented in Section 5, we chose to use the current Phased Array layout with the inclusion of the seven antennas from the baseline system, as this instrument has the highest gain. The layout geometry can be visualized in Fig. 32.

Until now, the ARA collaboration has not published any results on the detection of cosmic rays because a robust estimate of the expected events was missing due to a lack of complete simulations. However, three different ARA analyses searching for neutrinos have shown events that may be consistent with radio emissions from cosmic rays. In 2020, a set of $\sim 10 - 20$ cosmic–ray candidates was presented at the APS April Meeting [72], and one candidate was found in two separate analyses, at a zenith angle of $\sim 1°$.
The first analysis uncovered 23 events consistent with being cosmic rays due to their angular distribution: a flat distribution in azimuth and a peak of the zenith distribution around 30°, consistent with estimations. Out of the 23 candidates of this analysis, one event showed a double pulse with a time delay that was not the same in each antenna. The time difference between the two pulses in all antennas reminded the two sources of radio emission from a cosmic–ray air–shower hitting the ice.
Another analysis performed on a 10% sample of a 4–year dataset [73] revealed 1 cosmic–ray candidate that was part of the 23 candidates of the first analysis. Finally, a recent analysis [74] using data from the Phased Array contained 14 cosmic–rays candidates. As explained in Section 4.2, the Phased Array has a reduced detection threshold, so that lower energy events can be detected. The

cosmic–ray flux in this energy range varying as $E^{-2.7}$, the 14 candidates from this Phased Array analysis are consistent with the 1 candidate from the 10% dataset.
However, the CR–rate in ARA appears to be an order of magnitude lower than expected by comparison with ARIANNA[8] [75]. The hypothesis for this discrepancy is that the real trigger threshold for cosmic rays is slightly higher than expected, leading to a decrease of events due to the $E^{-2.7}$ dependency of the flux, but nothing is confirmed as of today.

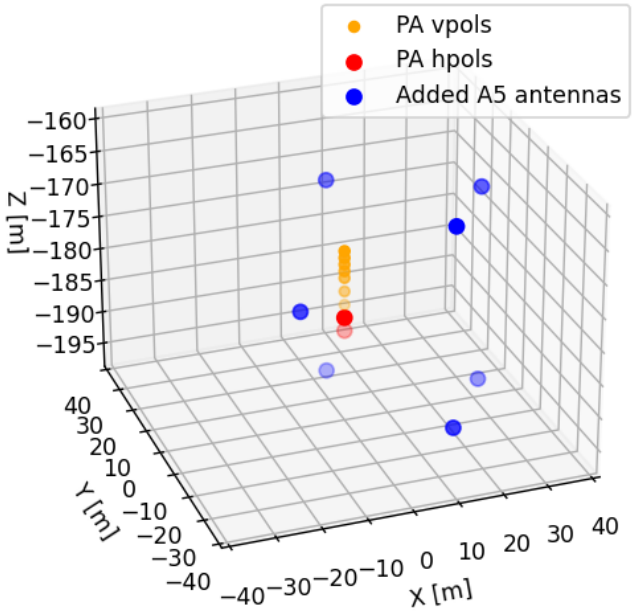

ID	X [m]	Y [m]	Z [m]
s0a0	0	0	-184.79
s0a1	0	0	-182.79
s0a2	0	0	-180.79
s0a3	0	0	-178.75
s0a4	0	0	-176.70
s0a5	0	0	-175.68
s0a6	0	0	-174.66
s0a7	0	0	-173.65
s0a8	0	0	-172.635

ID	X [m]	Y [m]	Z [m]
s1a0	1.5483	15.6665	-196.2045
s1a1	1.5458	15.6587	-166.5366
s2a0	-12.9616	-8.6511	-177.7466
s3a0	12.3309	-31.8967	-190.8559
s3a1	12.3428	-31.8885	-161.02376
s4a0	29.6505	-3.2845	-194.739
s4a1	29.6347	-3.3004	-165.0948

Figure 32: 3D visualization of the current antennas connected to the Phased Array DAQ. s0a0 and s0a1 are the Phased Array HPols used for reconstruction (red) and s0a2 to s0a8 are the Phased Array VPols (orange). The 7 other antennas are from the baseline system of ARA5 (blue).

[8]Neutrino experiment in Antarctica sensitive to in–ice Askaryan emission that reflects off of the ice-water boundary at the bottom of the Ross Ice Shelf

4.4 ARA Perspectives

Even if no neutrino is found in the current dataset, important knowledge can still be extracted from the ongoing analysis. Just as IceCube, ARA is setting limits on the UHE–neutrino flux by utilizing the present lack of neutrino detection. If no neutrino is found at the end of the analysis, ARA will be able to set the most stringent limit on the flux of UHE neutrinos. As discussed in Section 1.1.2, UHE neutrinos are expected to be produced by protons through the GZK effect. The 3 neutrinos produced by the π^+ decay in Eqs. 7 and 8 each carry approximately 5% of the initial proton energy. However, if the primary cosmic ray is not a proton but a heavier nuclei, its interaction with a CMB photon will only split it in lighter components with lower energies. The final components are then less likely to interact again through GZK effect and produce neutrinos. Since the cosmic–ray flux has been measured to energies up to 10^{21} eV, the absence of GZK neutrino at $\sim 10^{18-19}$ eV would thus indicate a much heavier mass composition of UHE cosmic rays. The neutrino flux limit would set constraints on various astrophysical and cosmogenic models. This would lead to better models of both sources that are found to produce neutrinos and sources that are not.

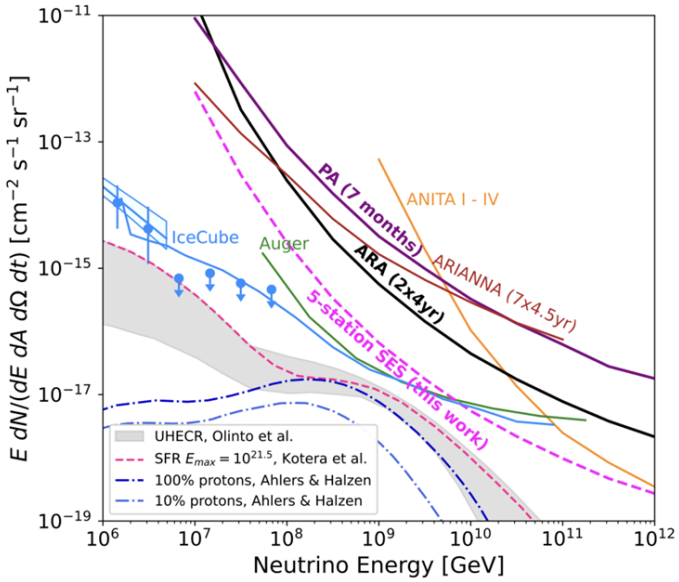

Figure 33: Projected single–event[9] sensitivity of the diffuse neutrino flux from the ARA five–station analysis, compared to limits from previous ARA analyses. From [76]

The current limits set by ARA on the UHE neutrino flux are shown in Fig. 33. This figure includes the sensitivity from two previous analyses: one

[9]The level of flux where we would expect a single event (zero background assumed)

based on a seven–month dataset from the Phased Array and another on a four–year dataset from ARA2 and ARA3. Additionally, it displays the projected single-event sensitivity of the ongoing analysis (dashed line), calculated by rescaling the previous sensitivities for the livetime of the new analysis.

Finally, even without conclusive results, the work done by ARA members to develop the reconstruction methods and the detector technology will greatly benefit the incoming radio upgrade of IceCube. ARA is thus a test bed for IceCube–Gen2 Radio and a pathfinder for all the next generation radio arrays.

5 Estimating the Number of CR Events in ARA

With the dataset that ARA accumulated over 25 station–years and the simulation framework presented in Section 3.1, it is possible to search for cosmic–ray signals in ARA. However, the starting point for any cosmic–ray or neutrino search is to estimate how many neutrino and cosmic–ray events we should find inside the dataset. To estimate the cosmic–ray event rate in a detector like ARA, one needs a good knowledge of the physical process producing the signal, the flux of cosmic rays hitting the atmosphere and the detector itself. The physics implemented in CORSIKA has been tested thoroughly by several experiments and while the in–ice part has not yet been challenged by in–situ experiments, it is well motivated by laboratory tests. The flux of cosmic ray has been measured up to 10^{21} eV by the Pierre Auger Observatory but the composition at high energies remains unclear, which introduces an uncertainty in the event rate estimate. Lastly, the response of a given ARA antenna to a radio signal is simulated using another framework called AraSim[77]. Some uncertainties can arise from the detector simulation or from the knowledge of the refractive index profile in the ice, but these should not have a big impact on a raw event rate estimate.
We can thus confidently use the available simulation frameworks to make our way towards an event rate estimate in ARA. The steps are the followings:

1. Build a library of simulated cosmic–ray events
2. Generate a dataset based on the library
3. Simulate the ARA response to the generated events
4. Compute the trigger efficiency and effective area for a given ARA station
5. Multiply the effective area by the cosmic–ray flux to obtain the final event rate in the detector

5.1 Build a Library

Building a library of simulated events with different parameters is not only important to estimate the event rate but also to better understand the properties of the signal and how it depends on the input parameters.

5.1.1 Preliminary Analysis

In order to build the library, the first step is to determine the antenna grid to use. Ideally we would be able to use a star grid with radial symmetry that allows for interpolation as in Fig. 16, but as previously mentioned, interpolation does not work with non–vertical showers. As we want our grids to include all the interesting features of the radio emission, a dense square grid of antennas

must be used. The problem with dense antenna grids is that their simulation is very CPU–time consuming (see next section), so that a good balance has to be found between antenna spacing and grid size. The grid size mostly depends on the radius of the Cherenkov ring for the in–ice emission for low zenith angles. As shown in Fig. 25, high zenith radio footprints are dominated by the in–air emission, and the grid size must thus be scaled accordingly. In order to estimate the needed grid size, we started by simulating a cross–shape (Fig. 34, left) and subsequent denser grids (Fig. 34, right) for different zeniths.

Based on the results in Fig. 34, the grid sizes displayed in Table 3 have been chosen to contain the bulk of the emission, implying a certain number of antennas required for the simulations. As discussed in Section 3.2, the antenna spacing induces a leakage of the signal through the grid, which limits the precision of subsequent analysis. An antenna spacing of 20 m was thus chosen as a good balance between computational time and accuracy of the reconstruction of radio footprints properties.

ZENITH [deg]	x_{min} [m]	x_{max} [m]	y_{min} [m]	y_{max} [m]	# of antenna
0	-180	180	-180	180	361
10	-140	220	-180	180	361
20	-100	260	-180	180	361
30	-60	300	-180	180	361
40	-60	360	-200	200	462
50	-140	400	-210	210	616

Table 3: Size of the grids used to build the library. Together with an antenna spacing of 20 m, it gives the required number of antenna to simulate (right column).

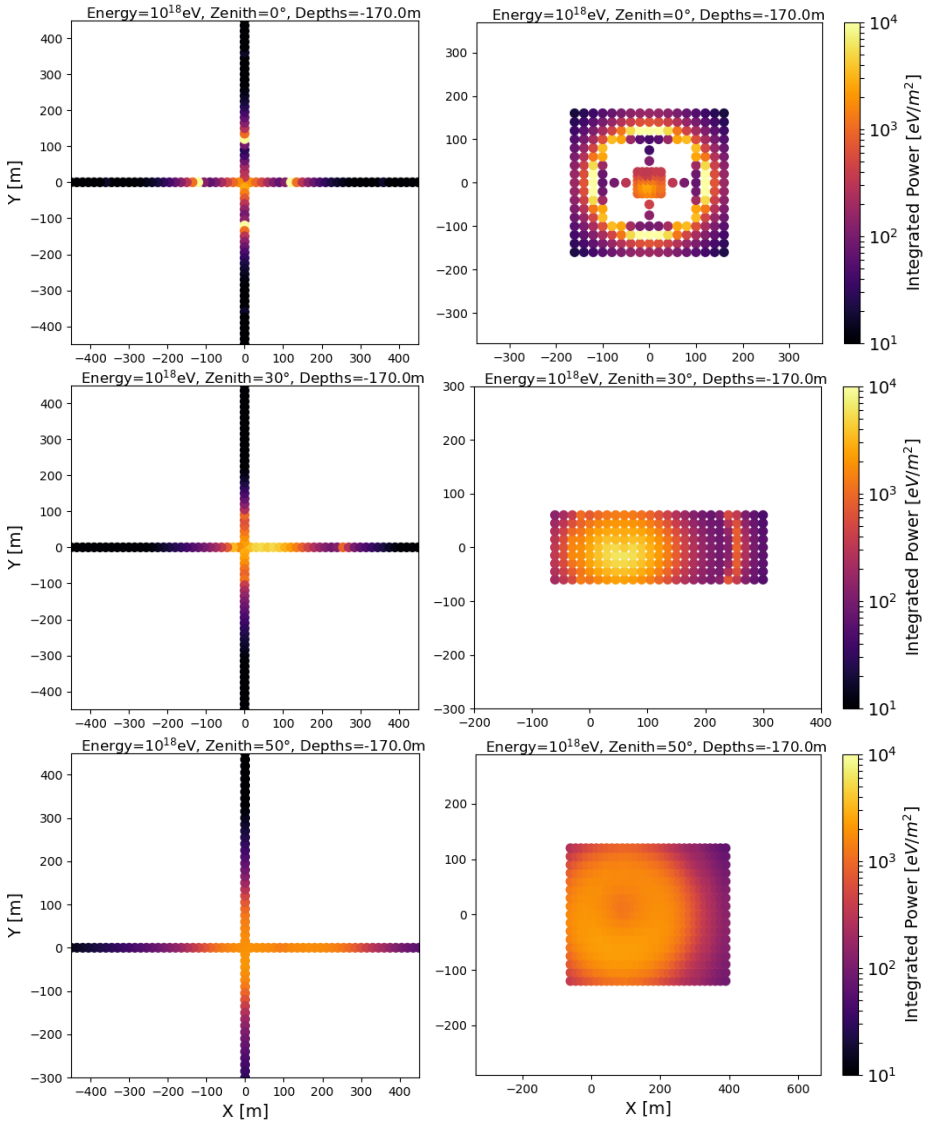

Figure 34: Fluence plots of the total emission made with plus–shape grids and denser grids to locate the features of the signal and understand the size of the footprints. These tests have been made at different zenith angles: 0° (top), 30° (middle) and 50° (bottom), with a primary energy of 10^{18} eV.

5.1.2 CPU–time consumption

CORSIKA and GEANT4 are quite different in terms of computational cost. Since both of them use multiple CPU's, we can distinguish between CPU–time (the time spent by a single CPU) and the job run time (the time between the start and the end of the simulation process, equivalent to the longest CPU–time).

To simulate an air–shower initiated by a high energy proton entering the atmosphere, the CORSIKA+CoREAS simulation is split in groups of 10 antennas, each on a different CPU. A low zenith air–shower therefore requires the usage of 36 CPU's (see Table 3). Each CPU simulates the full air–shower and its radio emission down to the corresponding set of 10 antennas. The CPU–time consumption has not been tracked in this work but a very similar study [40] using 10^{17} eV vertical proton–induced showers obtained an average CPU–time of 21.3 h by splitting the simulations in groups of 15 antennas, and a job run time of 26.8 h. The CPU–time obviously depends on the primary energy, and increases by a factor of roughly ~ 5 when increasing the latter by a factor 10. The CPU–time also depends on the zenith angle: Increasing the zenith angle implies longer distances over which the shower develops and the emission is ray–traced. The CPU–time is thus longer for $\theta = 50^\circ$ than for a vertical shower, reaching up to $\sim 8 - 9$ days for a 10^{18} eV, 50° shower.

To reduce the job run time of the in–ice simulation with GEANT4, only the particles within a radius of 1 m from the shower axis are propagated through the ice, as discussed in Section 3.2. The particles contained in this 1 m radius footprint are then split in separate parts, each of these parts being then used as inputs for separate GEANT4 simulations on different CPU's. Each CPU thus simulates the in–ice cascade produced by a reduced number of particles and propagates the in–ice emission towards all antennas of the grid. To balance the CPU–time over all these parts, the splitting process is based on the energy of the particles: certain parts contain fewer high energy particles and other contain more low energy particles. The CPU–times for a 10^{17} eV vertical proton from the previously mentioned study [40] are shown in Fig. 35.

We see that most of the CPU–times are reasonably low but the job run time is driven by a few simulations containing the highest energy particles.
For the zenith scaling of CPU time for the in-ice component, the situation contrasts with that of the in-air component. As noted earlier, increasing the zenith angle results in fewer particles reaching the ground and cascading in the ice, leading to shorter CPU times.

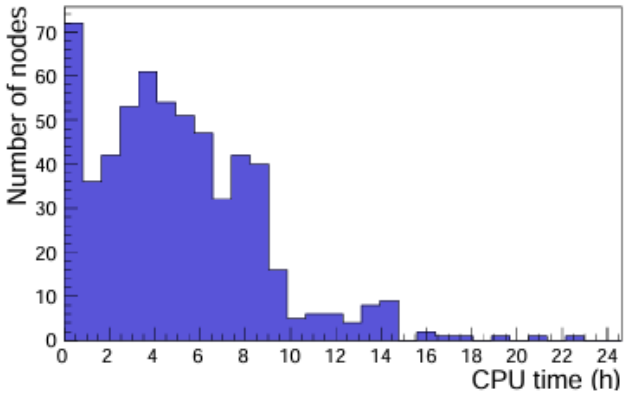

Figure 35: A distribution of the CPU time of 591 cores used for the simulation of the in-ice particle cascade and the corresponding radio emission for 121 antennas in the ice, using a primary energy $E_p = 10^{17}$ eV and a zenith angle $\theta = 0$. From [40]

5.1.3 Parameters Phase Space

The phase space of the simulations inputs is displayed in Table 4.

log_{10}(Energy [eV])	16.5, 17, 17.5, 18
Zenith [deg]	0, 10, 20, 30, 40, 50
Azimuth [deg]	0
Antenna Depth [m]	From -145 to -200 per step of 5

Table 4: Simulations inputs used to build the library.

By varying only the primary energy and zenith, we reach a number of 24 different events in the library. However, as it would take too much time to simulate all the layers at the same time, we speed up the process by simulating separately for each of the 12 layers, which means a total of 288 simulations are needed.
In this work we simulated only protons and heavier primaries can be equivalently simulated by asking for smaller values of X_{max} (i.e. higher altitude), which can be done when launching a CORSIKA simulation. Here however, only one value of X_{max} is used per zenith and per energy. The X_{max} used are displayed in Table 5 and they are typical values for protons, as can be seen in Fig 2.4 of [78]. The library thus only contains proton events and should in principle be completed by simulating heavier primaries.
However, the phase space of the input parameters is very limited as a consequence of the CPU–time consumption for each simulation, as described in the previous section. For the same reason, no simulation has been made for 10°, 20° and 40° zenith for the two highest energies $10^{17.5}$ eV and 10^{18} eV, as it would take a few additional months.

	$10^{16.5}$eV	10^{17} eV	$10^{17.5}$ eV	10^{18} eV
0°	710	705	715	720
10°	710	715	\	\
20°	705	705	\	\
30°	700	740	725	745
40°	690	725	\	\
50°	690	740	755	775

Table 5: X_{max} of the simulations for each zenith and energy, in g/cm^2 and along the shower axis.

A 3D visualization of the emission footprint for a typical event from the library is displayed in Fig. 36.

5.1.4 Energy Scaling

In order to fill the library with the missing simulations in a reasonable amount of time, we used an energy scaling on the low energy events of the library to infer the electric fields at $10^{17.5}$ eV and 10^{18} eV, for zeniths of 10°, 20° and 40°.

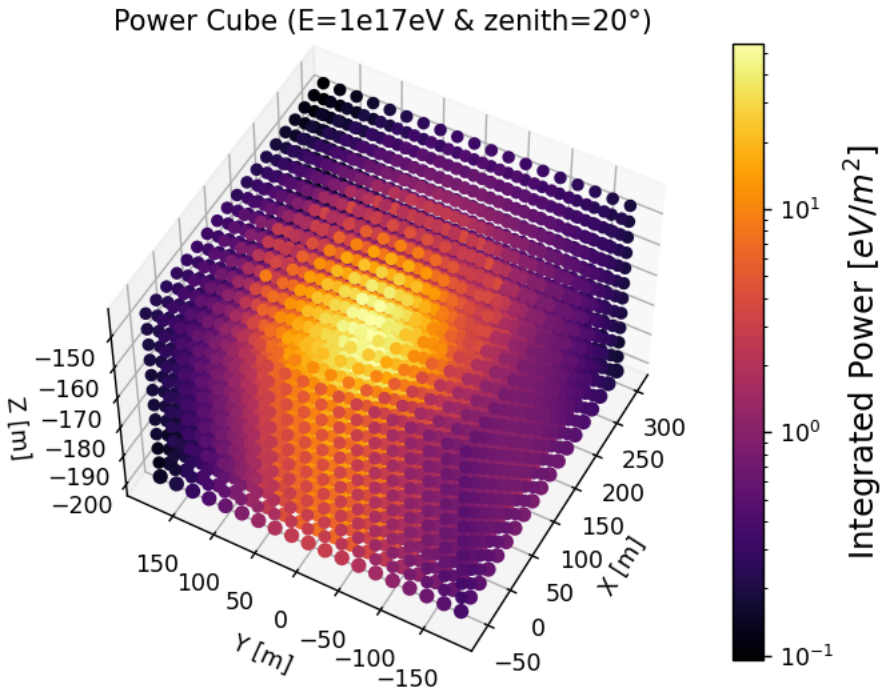

Figure 36: 3D visualization of one of the cubic grid used to build the library.

A. In–Air Emission

The principle behind an energy scaling for air–shower radio emission was already explained in Section 2.1. If the primary energy is increased by a factor 10, the number of emitters (i.e. electromagnetic particles) increases by a factor 10 as well, and coherence implies a linear relationship between the number of emitters and the signal amplitude. Since the fluence depends on the electric fields squared, the fluence values at 10^{18} eV should be 100 times the ones at 10^{17} eV. To check if this is correct, one can integrate the in–air emission fluence over the footprint at a certain depth and compare the results for two different primary energies. It is thus a comparison of the total air–shower emission energy. Since a fluence plot is a discrete set of fluence values, the total in–air emission energy is calculated as in Eq. 33:

$$E_{air} = \sum_{ant \in GRID} \mathcal{F}_{ant}^{air} \tag{40}$$

where F_{ant}^{air} is the air–emission fluence value at a certain antenna of the grid. Calculating the total air emission energy for two different primary energies E_{p1} and E_{p2}, one gets the fluence scaling factor for in–air emission:

$$s = \frac{E_{air}(E_{p1})}{E_{air}(E_{p2})} \tag{41}$$

Fig. 37 shows the scaling factors calculated from the simulations available in the library, for 0°, 30° and 50° zeniths. To have more statistics, the scaling factor was calculated separately for each layer of the cubic grid. The dashed lines represent the scaling factor averaged over each layer/depth.

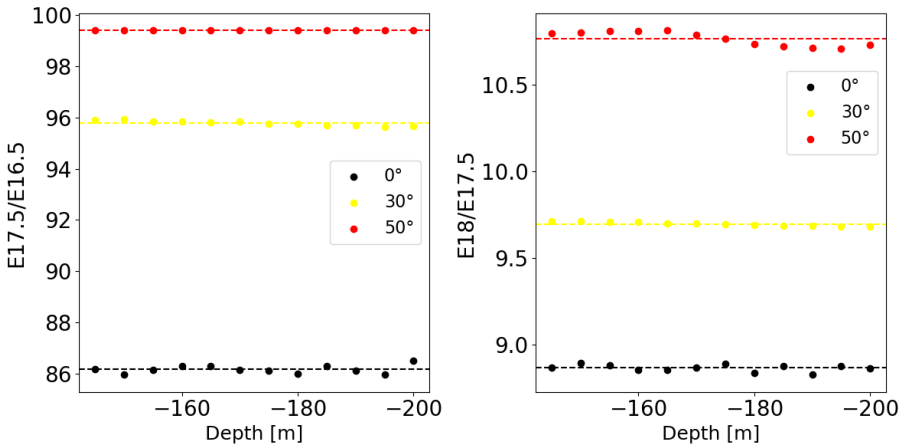

Figure 37: Scaling factor of the in–air emission total energy between different primary energies, for several depths. The dashed lines represent the average over depths.
Left: Scaling from a primary energy of $10^{16.5}$ eV to $10^{17.5}$ eV.
Right: Scaling from a primary energy of $10^{17.5}$ eV to 10^{18} eV.

The results are in agreement with:

$$s \approx \left(\frac{E_{p1}}{E_{p2}}\right)^2 \tag{42}$$

except for the vertical showers were the scaling factor seems significantly lower. We explain it the following way: Because of the high elevation of the South–Pole ice sheet (2835 m), vertical air–showers have their X_{max} very close to the ground. For instance, a 10^{18} eV air–shower has an $X_{max} \sim 720$ g/cm^2, to compare with the ground level in slant depth: 728 g/cm^2. In this case, a fraction of the total electromagnetic energy of the shower is buried in the ice before being radiated. This causes a decreasing of the scaling factor for high energy vertical showers. The same conclusion was reached in [40], with a scaling factor of 9 to go from a primary energy of $10^{17.5}$ eV to 10^{18} eV (right plot in Fig. 37). This effect is expected to disappear when considering lower energies because low energy showers develop faster, so X_{max} is further from the ground and the emission is less affected by the ground proximity. The scaling factor between $10^{16.5}$ eV and 10^{17} eV is thus expected to be 10. Now, if we take a scaling factor of 10 for $10^{16.5} \rightarrow 10^{17}$ and a scaling factor of 9 for $10^{17} \rightarrow 10^{17.5}$, it makes a factor of 90 for $10^{16.5} \rightarrow 10^{17.5}$, in good agreement with the left plot of Fig. 37. Note that the scaling factor of the electric field amplitudes is simply given by $\sqrt{s}$.

B. In–Ice Emission

For the in–ice emission the situation is a little bit different as the number of emitters in the in–ice cascade also depends on the shower development just before reaching the ground, and thus on the distance from X_{max}. The amplitude of the in–ice emission has thus no reason to scale linearly with primary energy. In fact, when increasing the primary energy by a factor of 10, 2 effects add up to increase the in–ice emission amplitude. The first is the linearly increasing number of electromagnetic particles in the air–shower. The second is due to the X_{max} of the shower being closer to the ground, resulting in a higher fraction of the electromagnetic energy of the air–shower being deposited in the ice. The scaling factor of the in–ice emission amplitude is thus expected to be higher than 10. In order to derive this scaling factor, we can compare the total energy deposited in the ice for different primary energies. Fortunately, the GEANT4 module allows to compute the deposited energy density, as represented in Fig. 12. After integration, the total deposited energy can be compared for two primary energies, and the resulting ratios are shown in Fig. 38.

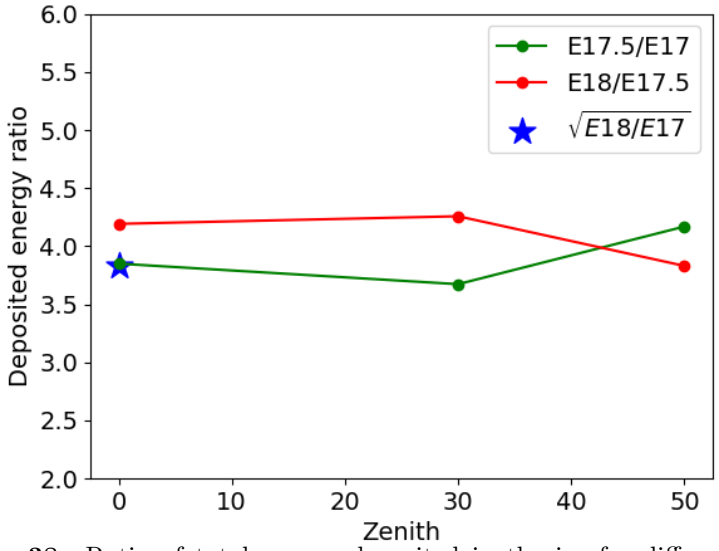

Figure 38: Ratio of total energy deposited in the ice for different primary energies. The blue star was added from [40], where a ratio of 14.70 was found between 2 vertical showers at 10^{17} eV and 10^{18} eV.

Note that the ratios here are equivalent to $\sqrt{s}$, as they are not integrated fluence scaling factors like in Fig. 37, but just measures of the total particle energy contained in the in–ice cascades. The amplitude of the in–ice emission is then expected to scale linearly with the deposited energy. The results suppose a scaling factor of 4 when the primary energy is increased by $\sqrt{10}$, independently of the zenith angle. This is in agreement with [40] where a scaling factor of 14.70 was found between a 10^{17} eV and a 10^{18} eV primary.

C. Summary

In order to fill the library with events at $10^{17.5}$ eV and 10^{18} eV for 10°, 20° and 40° zenith angles, different scaling factors are applied to the in–air and in–ice electric fields. For all zeniths, the amplitudes of the in–ice emission at $10^{17.5}$ eV are obtained by multiplying the ones at $10^{16.5}$ eV by 16 (see Table 6 from $10^{16.5}$ to $10^{17.5}$ eV), and the ones at 10^{18} eV are then obtained by multiplying the amplitudes at $10^{17.5}$ eV by a factor 4. For the in–air emission, different scaling factors are applied depending on the zenith angle. For 10° zenith angle, the amplitudes at $10^{16.5}$ eV are multiplied by $\sqrt{10} \times 3$ to obtain the ones at $10^{17.5}$ eV, which are then multiplied by 3 to obtain the ones at 10^{18} eV. For 20° and 40°, the amplitudes at $10^{16.5}$ eV are multiplied by $\sqrt{10} \times \sqrt{10}$ to obtain the ones at $10^{17.5}$ eV, which are then multiplied by $\sqrt{10}$ to obtain the ones at 10^{18} eV. The fluence can then be calculated with Eq. 20.

	0°	10°	20°	30°	40°	50°
$10^{16.5} \rightarrow 10^{17}$	$\sqrt{10}$	$\sqrt{10}$	$\sqrt{10}$	$\sqrt{10}$	$\sqrt{10}$	$\sqrt{10}$
	4					
$10^{17} \rightarrow 10^{17.5}$	3	3	$\sqrt{10}$	$\sqrt{10}$	$\sqrt{10}$	$\sqrt{10}$
	4					
$10^{17.5} \rightarrow 10^{18}$	3	3	$\sqrt{10}$	$\sqrt{10}$	$\sqrt{10}$	$\sqrt{10}$
	4					

Table 6: Scaling factors of the electric field amplitudes of the in–air emission (in blue) and the in–ice emission (in red), for different zenith angles. The values were chosen based on Fig. 37 and Fig. 38.

5.2 Random Event Generator

With the library completed, it is possible to generate events with random energy, zenith, azimuth and impact position of the shower core on the ground. These generated events are then associated to the closest event in the library in terms of energy and zenith, before being rotated following the azimuth angle and shifted following the impact position. The phase space of the generated parameters is the following:

- Energy: From $10^{16.25}$ eV to $10^{18.25}$ eV
- Zenith: From 0° to 55°
- Azimuth: From 0° to 360°
- Impact position: From –500m to 500m in both $\hat{x}$ and $\hat{y}$ directions

From geometrical considerations, we know that a zenith bin of [0,ϵ] enclose a smaller solid angle on the sky than [50°,50°+ϵ] and thus the number of incoming cosmic rays should increases with zenith. To take this into account, a flat distribution in cos(θ) was first generated before being converted in a zenith (θ) distribution (see Fig. 40). The energy was split in 4 logarithmic bins of width 0.5 and the number of events was equally distributed in each bin. Note that in all the simulations, the origin (x=0,y=0) is defined as the impact position but here the origin is just an arbitrary point on the ice layer surface.

Fig. 39 shows an example of randomly generated fluence plot. In this example, the random parameters are:

- Energy = $10^{18.11}$ eV
- Zenith = 28.6°
- Azimuth = 47°
- Impact position on the ice surface: (x,y) = (67 m,-182 m)

The procedure starts with the zenith angle and the primary energy. In this example the closest simulated event in the library is $\theta = 30^\circ$ and $E = 10^{18}$ eV, so the electric fields of the in–air and in–ice emission of this event are selected (left plot). Then the position of each grid point is rotated by $\phi = 47^\circ$ on the x–y plane and then shifted by 67 m towards positive x and 182 m towards negative y (right figure). To go from the left to the right plot, the formulae is:

$$X'_{ant} = X_{ant}cos(\phi) - Y_{ant}sin(\phi) + X_{impact} \tag{43}$$

$$Y'_{ant} = X_{ant}sin(\phi) + Y_{ant}cos(\phi) + Y_{impact} \tag{44}$$

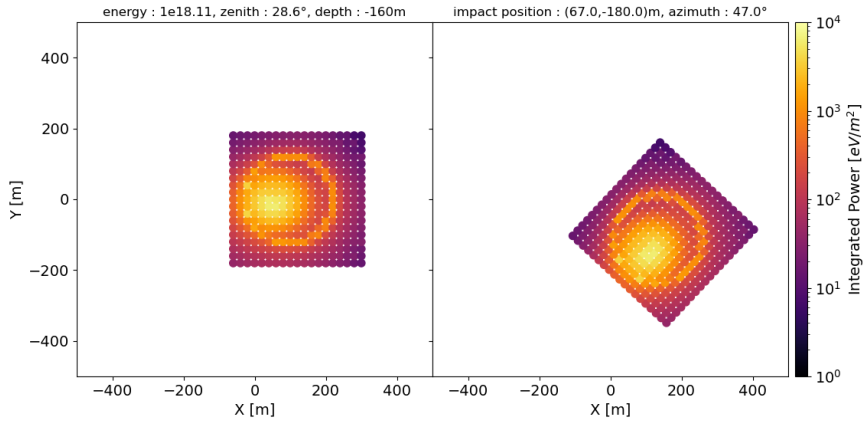

Figure 39: Randomly generated fluence plot at −160 m. The random parameters are: $E = 10^{18.11}$ eV, $\theta = 28.6^\circ$, $\phi = 47^\circ$, $X_{impact} = 67$ m and $Y_{impact} = -182$ m. On the left is the fluence plot of the corresponding closest event from the library and on the right is the same fluence plot after rotation through the azimuth and shift through the impact position.

Since we already calculated energy scaling factors in the previous section, we can use them to scale the electric fields amplitudes from the closest simulated energy in the library (E_{ref}) to the randomly generated energy (E_{gen}). The formulae is the following:

$$E'_i = E_i \times (\sqrt{s})^{\frac{log(E_{gen}) - log(E_{ref})}{0.5}} \tag{45}$$

where E_i is the $i = x, y, z$ component of the electric field and $\sqrt{s}$ is the amplitude scaling factor that depends on the reference zenith angle and on E_{ref} (see Table 6). In this example, since $\theta_{ref} = 30^\circ$ and $E_{ref} = 10^{18}$ eV, we have $s_{air} = 10$ and $s_{ice} = 16$, so $E'_{i,air} = 1.29E_{i,air}$ and $E'_{i,ice} = 1.36E_{i,ice}$. The electric fields from in–air and in–ice emission are then (vectorially) added together to get the total electric field.

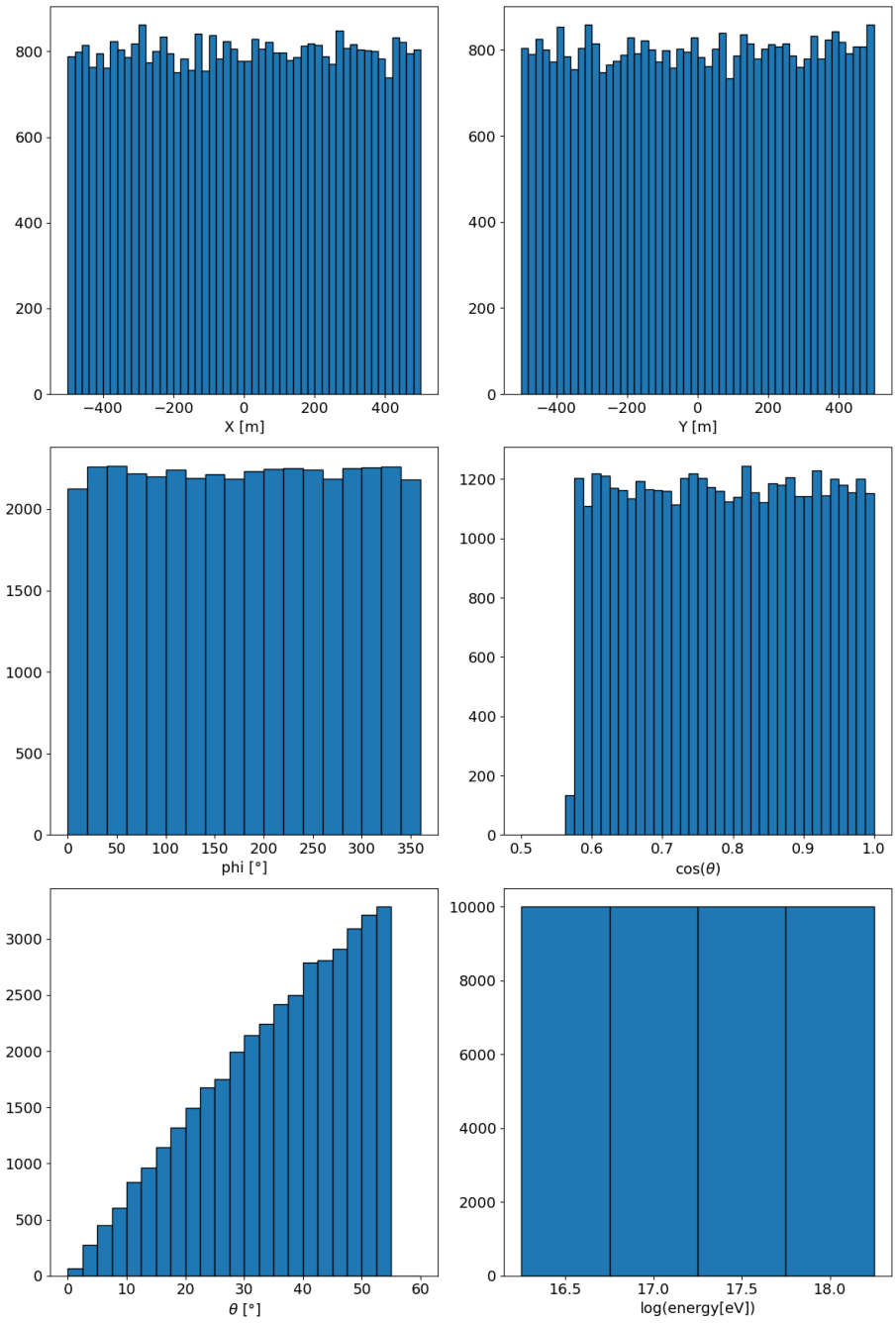

Figure 40: Distributions of the randomly generated parameters over 40000 events: Impact position of the shower core on the South–Pole ice sheet (x,y), azimuth angle (phi), cosinus of the zenith angle ($cos\ \theta$), zenith angle and logarithm of the primary energy.

The last important thing to take care of is the polarization of the signal. The x and y polarizations have to be rotated according to the azimuth angle. This can be done simply with:

$$E'_x = E_x cos(\phi) - E_y sin(\phi) \tag{46}$$
$$E'_y = E_x sin(\phi) + E_y cos(\phi) \tag{47}$$

5.3 Implement Trigger Conditions

Now that we have all the tools to generate random events, the next step is to add an ARA station. The idea is to place a typical ARA station centered at (x=0,y=0) and infer the signal received by each antenna by looking at the closest point on the generated grid. The antenna positions used are the ones in Fig. 32. If the generated grid is too far from the antennas, we assume that they do not receive any signal and therefore no trigger occurs. The exact condition is $D_{ant}^{min} > 20$ m, where D_{ant}^{min} is the distance between an antenna and the closest generated grid point, and 20 m is the spacing between two grid points. Any antenna with $D_{ant}^{min} < 20$ m will be associated to its closest grid point.

To trigger a typical ARA station, the condition is that either 3 VPols or 3 HPols have a signal to noise ratio (SNR) higher than SNR=6. If the station has a Phased Array, then there is also the possibility that the Phased Array triggers. As explained in Section 4.2, the Phased Array acts as a single antenna with an increased gain, so that ARA5 is easier to trigger on a coherent signal induced by a cosmic–ray or neutrino emission. For ARA5, since the only antennas used for triggering are the Phased Array antennas, the trigger condition only involves the Phased Array.

As the previous condition requires to compute the SNR, which highly depends on the antennas properties and noise model, we can use another trigger condition that is very naive but simpler to implement. The idea is to use a basic fluence threshold, i.e. asks that the fluence value of at least one of the Phased Array antennas is above a certain threshold.

The fluence threshold condition completely ignores the shape, the polarization and the arrival angle of the signal. In order to implement a more realistic trigger condition, the best solution is to use AraSim. AraSim is a complex framework developed to simulate neutrino interactions in the South–Pole ice, ray–trace the emission to the antennas and simulate the full electronic chain of the ARA stations. This part of the work was realised by an ARA expert who modified AraSim to be able to process the simulated electric fields from this work at given antenna positions to directly simulate the antenna response. In order to do that, since the antenna gain depends on the arrival direction of the ray at the antenna, the latter has to be guessed from ray–tracing considerations, assuming a certain position of the emitter.

The assumption we make is that all the emission comes from the shower impact point on the ground. We thus neglect the vertical extension of the in–ice cascade and the fact that the in–air signal coming from X_{max} is emitted at $\sim 1°$. The latter assumption is especially problematic when considering a very inclined air shower, since X_{max} is very far from the ground in this case. This means that the in-air emission can reach the ground far from the shower impact point.
Then, because of ray–bending in the ice, a ray emitted horizontally at the shower impact point will reach a certain depth at a finite horizontal distance r_{max}. It can be seen in Fig. 41 that a ray emitted at $z = 0$ with a 90° launch angle reaches $z = -100$ m at a horizontal distance of $r \sim 180$ m. As the randomly generated cosmic rays are allowed to fall up to 500 m away from the origin where the antennas are situated, any signal coming from a shower impact point that is too far from the origin cannot be ray–traced to the antenna position. In this case, the assumption that the emission comes from the shower impact point cannot be used, and the X_{max} position is used instead. The procedure is thus the following:

1. Ray–tracing is done from the shower impact point to a fixed depth h, varying the launch angle from 0° to 90°. For each launch angle, the horizontal distance (r) and the arrival direction (θ_f) of the ray when it reaches the chosen depth (h) is written in a table. The horizontal distance reached with a 90° launch angle is stored as r_{max}.

2. The ray–tracing is now done from the position of X_{max}. If the zenith angle of the air–shower is θ, the launch angle is varied between θ and 90° until $r > r_{max}$. The launch angle corresponding to $r \approx r_{max}$ is now stored as θ_{start}.

3. Ray–tracing is done from X_{max} to the depth h by varying the launch angle from θ_{start} to 90°. The horizontal distances $r_{max} < r < 500m$ and the arrival angles θ_f are added to the table.

4. The process is repeated for each depth corresponding to the layers used in the simulations ($d \in$ [-145 m,-200 m]).

We now have interpolation tables giving the arrival elevation of the ray at a certain antenna given the depth and the horizontal distance of the antenna with respect to the shower impact point. Note that the tables assume a certain X_{max} position and thus depend on the energy and zenith angle of the air–shower. They have thus been generated for each event of the library, and the X_{max} used are the ones displayed in Table 5. For the non–simulated events at high energies, typical X_{max} values have been taken. To express the X_{max} given in Table 5 as an altitude above the ground level in meters, one has to use the atmospheric model of South–Pole (Eqs. 21 and 22).

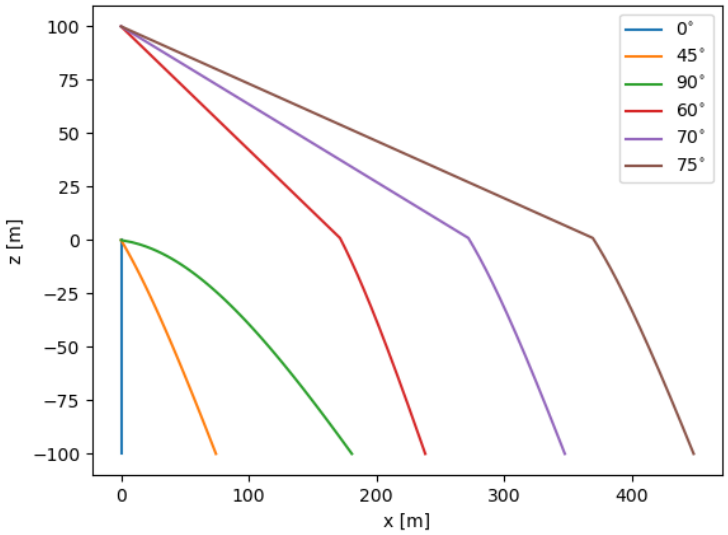

Figure 41: Ray–tracing in South–Pole ice with several launch angles and assuming 2 different emission points: One in $z = 0$ corresponding to the shower impact point and one at $z = 100m$ corresponding to the X_{max} of a vertical air–shower of a certain energy.

The azimuth angle of arrival is easier to calculate and is simply given by:

$$tan(\phi_f) = \frac{y_{core} - y_{ant}}{x_{core} - x_{ant}} \tag{48}$$

where x_{core}, y_{core} are the coordinates of the shower impact point and x_{ant}, y_{ant} are the coordinates of the antenna.

We are now able to generate a high number of random events (see Fig. 40) and, for each event, calculate the electric field received at each antenna of ARA5 (see Fig. 32), as well as the arrival direction of the ray. AraSim then decides for each event if ARA5 triggers or not.

5.4 Trigger Efficiency

The trigger efficiency is simply given by the number of events that triggered an ARA station divided by the total number of events. However, to take into account for the fact that the projected surface area is less than the actual simulated area by a factor cos(theta) when considering showers that arrive at a non-zero zenith angle, we multiply by this factor at this stage already. We thus calculate the trigger efficiency in zenith bins, then sum over the bins:

$$\mathcal{E}_{trig} = \frac{\sum_i N_{trig,i} cos(\theta_i)}{\sum_i N_{tot,i}} \tag{49}$$

$N_{trig,i}$ is the number of event with a zenith angle in the zenith bin i that triggered an ARA station, and $N_{tot,i}$ is the total number of event in that bin. From now on we will call trigger efficiency the $\mathcal{E}_{trig}$ given by Eq. 49.

5.5 Effective Area

From the trigger efficiency, it is trivial to calculate the effective area, defined as the surface of detection that the detector can cover modulo the trigger efficiency.

$$A_{eff} = A \times \mathcal{E}_{trig} \tag{50}$$

where in this case, $A = 1$ km^2. In principle, the effective area is invariant under a change of A as long as A is big enough to contain all the events that can possibly trigger the ARA station.

5.6 Cosmic–Ray Flux

The cosmic–ray flux at ultra high energies has been studied for multiple years by several experiments. The left part of Fig. 42 shows three different fitted flux functions from three different published results: One from IceTop[10] [79] and two from the Pierre Auger Observatory [80, 81]. Since we need a flux function in the interval $10^{16.25}$ eV - $10^{18.25}$ eV, we will be using the one from [81] (orange curve), which is the only one defined on the entire interval. The CR–flux integrated over each energy bin is displayed in the right part of Fig. 42.

The analytical flux function we use writes as:

$$J(E) = J_0 \left(\frac{E}{10^{16} eV}\right)^{-\gamma_0} \prod_{i=0}^{4} \left[1 + \left(\frac{E}{E_{ij}}\right)^{\frac{1}{\omega_{ij}}}\right]^{(\gamma_i - \gamma_j)\omega_{ij}} \tag{51}$$

The function is fitted over four parameters J_0, E_{ij}, γ_i and ω_{ij}, where the last three take different values $(i, j = 0, 1, 2, 3, 4, 5)$ corresponding to the different energy intervals over which different spectral indices are needed. The γ_i parameters represent the spectral indices of the power laws while ω_{ij} determines the width of the transitions between the power laws. The best–fitted parameters in the different energy intervals with statistical and systematic uncertainties are the following [81]:

- From $10^{15.8}$ eV to $E_{01} = (2.8 \pm 0.3 \pm 0.4) \times 10^{16}$ eV (*low energy ankle*): $\gamma_0 = (3.09 \pm 0.01 \pm 0.10)$
- From the *low energy ankle* to the *second knee* at $E_{12} = (1.58 \pm 0.05 \pm 0.2) \times 10^{17}$ eV: $\gamma_1 = (2.85 \pm 0.01 \pm 0.05)$

[10] Surface array of IceCube whose purpose is to detect secondary particles from UHE cosmic rays initiated air–showers [82]

- From the *second knee* to the *ankle* at
  $E_{23} = (5.0 \pm 0.1 \pm 0.8) \times 10^{18}$ eV: $\gamma_2 = (3.283 \pm 0.002 \pm 0.10)$
- From the *ankle* to the *instep* at
  $E_{34} = (1.4 \pm 0.1 \pm 0.2) \times 10^{19}$ eV: $\gamma_3 = (2.54 \pm 0.03 \pm 0.05)$
- From the *instep* to the abrupt suppression of the flux at
  $E_{45} = (4.7 \pm 0.3 \pm 0.6) \times 10^{19}$ eV: $\gamma_4 = (3.03 \pm 0.05 \pm 0.10)$
- After the suppression: $\gamma_5 = (5.3 \pm 0.3 \pm 0.1)$

The normalisation factor is given by $J_0 = (8.34 \pm 0.04 \pm 3.40) \times 10^{11} km^{-2} sr^{-1} yr^{-1} eV^{-1}$ and the values of ω_{ij} that describe the data the best are $\omega_{01} = \omega_{12} = 0.25$ and $\omega_{23} = \omega_{34} = \omega_{45} = 0.05$.

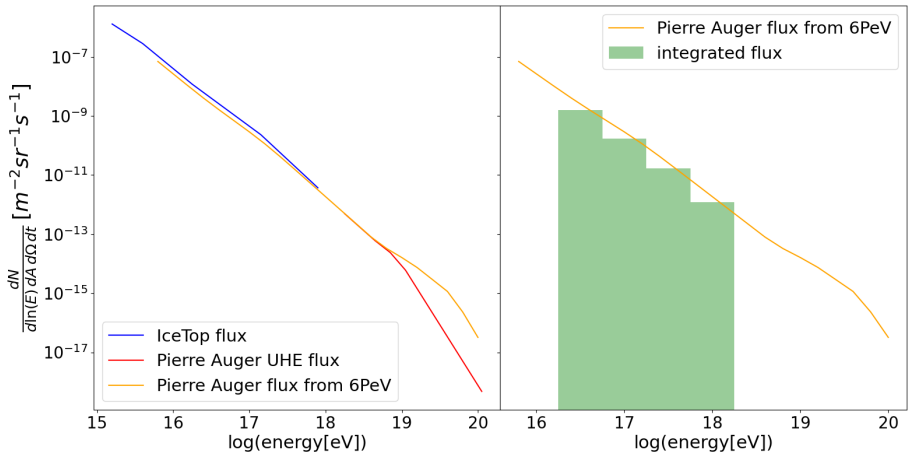

Figure 42: (left) Comparison of the UHE–CR flux function from [79], [80] and [81]. (right) UHE–CR flux function from [81] and integrated flux in the energy bins used in the random event generator.

We now have all we need to calculate the cosmic–ray event rate in ARA. We just need to multiply the effective area in each energy bin by the integrated flux, the observation time and the solid angle of arrival directions:

$$R(E_i) = A^i_{eff} F_i \int dt \int d\Omega \tag{52}$$

where:

$$\int d\Omega = \int_0^{2\pi} d\phi \int_0^{\theta_{max}} sin(\theta) d\theta \tag{53}$$

with $\theta_{max} = 55^\circ$.

5.7 Final Results

5.7.1 Fluence Threshold

We begin by presenting the results obtained using a simplistic fluence threshold. All the following results depend thus on this fluence threshold, the value of which is uncertain since the actual trigger condition does not rely on fluence.

A. Trigger Map

What we call a trigger map is a 2D representation of the impact position of the air–showers core at ground level. The events that triggered the Phased Array (yellow dot in the center) are marked in blue, and the other in red.

The trigger map for 10.000 events with primary CR energies between $10^{16.25}$ eV and $10^{16.75}$ eV and a fluence threshold of 1 eV/m^2 is shown in the left of Fig. 43. As expected, the triggering events gather around the Phased Array, in a region of $\sim$ 200 m radius. The right plot shows the zenith angle distribution of the triggering events. We see that the furthest events all have large zenith angles, while the small zenith events can only trigger the Phased Array if they land very close to it. This is due to the growing size of radio footprints with zenith angle.

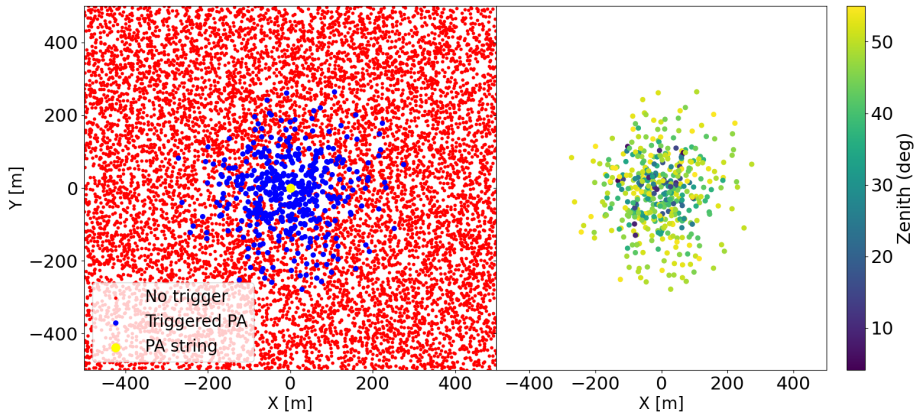

Figure 43: Generated shower impact positions in an energy range of $10^{16.25} - 10^{16.75}$ eV and for a fluence threshold of 1 eV/m^2. Left: The events that triggered the Phased Array (yellow dot) are marked in blue and the others in red. Right: Zenith distribution of the events that triggered the Phased Array.

Similar plots for a subset of events with primary CR energies between $10^{17.75}$ eV and $10^{18.25}$ eV and fluence thresholds of 1 eV/m^2 (top) and 1000 eV/m^2 (bottom), are shown in Fig. 44

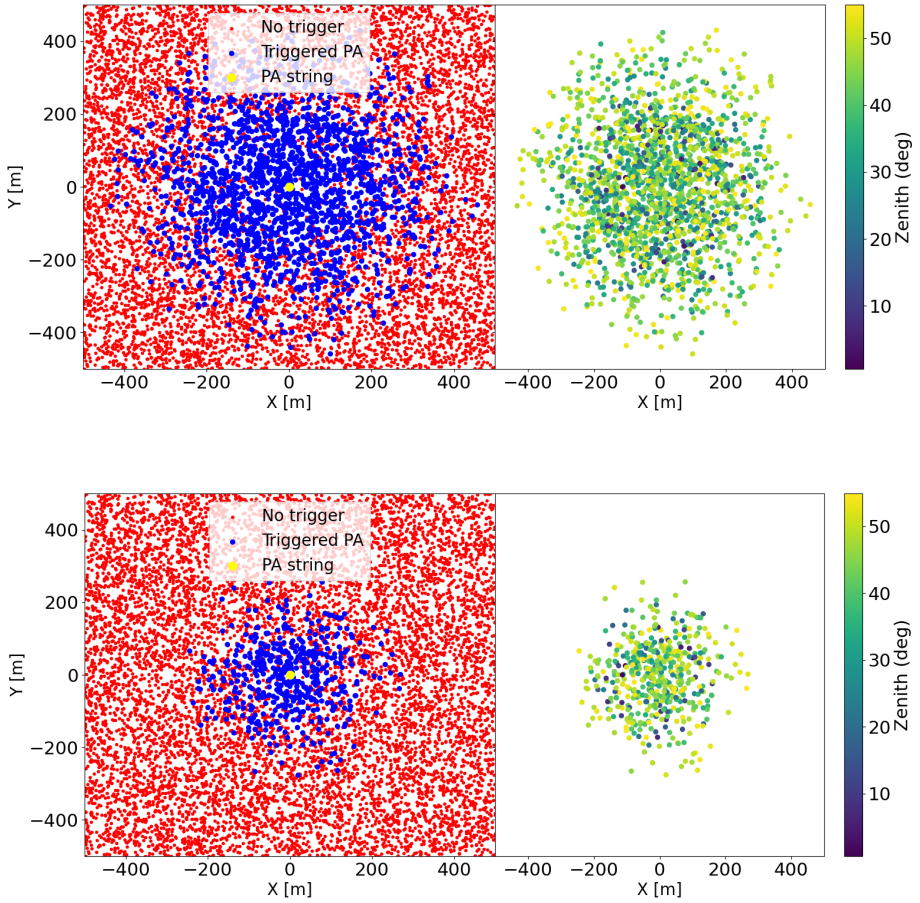

Figure 44: Generated shower impact positions in an energy range of $10^{17.75} - 10^{18.25}$ eV and for a fluence threshold of 1 eV/m^2 (top) and 1000 eV/m^2 (bottom).

We clearly see that the triggering region (blue dots) shrinks when increasing the fluence threshold, as the furthest events, i.e. the ones with the highest zenith angles, are not energetic enough due to the dilution of the radio emission energy at high zenith angles.

More trigger maps can be seen in Appendix C.

B. Trigger Efficiency Curves

The trigger efficiency as a function of the fluence threshold is shown in Fig. 45 for different energies. We see that the trigger efficiency drops very rapidly at low energies, and saturates around 15% at the highest energies for low thresholds. This saturation effect is purely geometrical since at such a high energy all the

grid points receive a fluence value superior to 1 eV/m^2 and the Phased Array thus triggers whenever a grid point is close enough ($D_{ant}^{min} < 20$ m). Note that in this case our simulation grid is likely too small and additional simulations are needed.

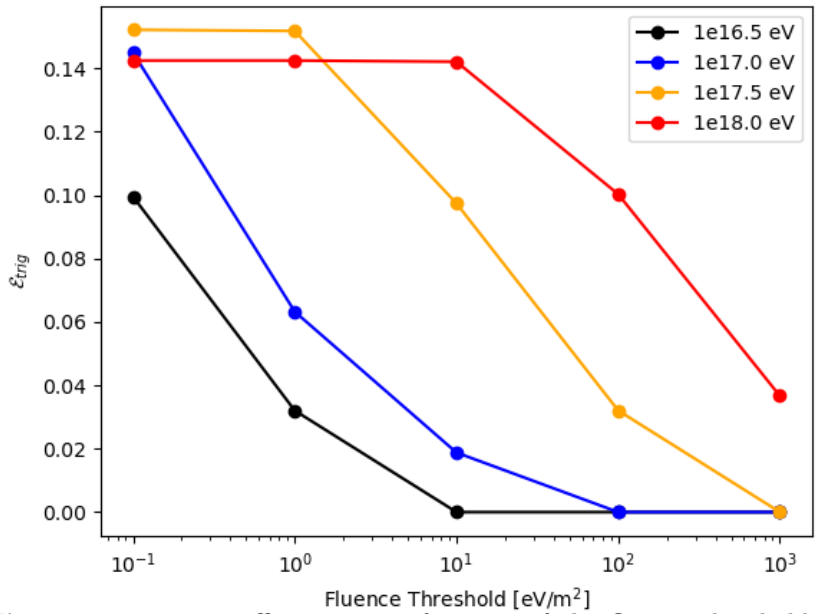

Figure 45: Trigger efficiency as a function of the fluence threshold in four different energy bins centered around $10^{16.5}$ eV (black), 10^{17} eV (blue), $10^{17.5}$ eV (orange), 10^{18} eV (red).

C. Effective Area Results

As the trigger efficiency depends on the size of the considered area, it is usually more interesting to calculate the effective area. Since the latter is simply given by the trigger efficiency times the size of the considered area, which is 1 km^2 in our case, the resulting plot is identical to Fig. 45 but with units of km^2 in the y–axis.

Fig. 46 shows the effective area in several zenith bins, for different energies and a fluence threshold of 1 eV/m^2. A lot of different features can be seen in this plot, but they are all due to three different effects: When increasing the zenith angle, the size of the footprint increases but the fluence values are lower and the number of events decreases due to the $\cos(\theta)$ factor in Eq. 49. For a very low threshold (top), the high-energy events are unaffected by the threshold, as all the grid points have a high enough fluence. Therefore, the behavior of the

red and yellow curves is purely geometrical. The effective area initially drops because of the $\cos(\theta)$ factor, but increases again at high zenith angles due to the growing size of the grids. At low energies, only the emission located on the in–ice Cherenkov ring or inside of the in–air Cherenkov ring can trigger, while all the other grid points have an insufficient fluence. The effective area is thus very low at low zenith angles because of the small size of the maximum emission region, and grows steadily at higher zenith angles because of the growing size of the in–air emission footprint.

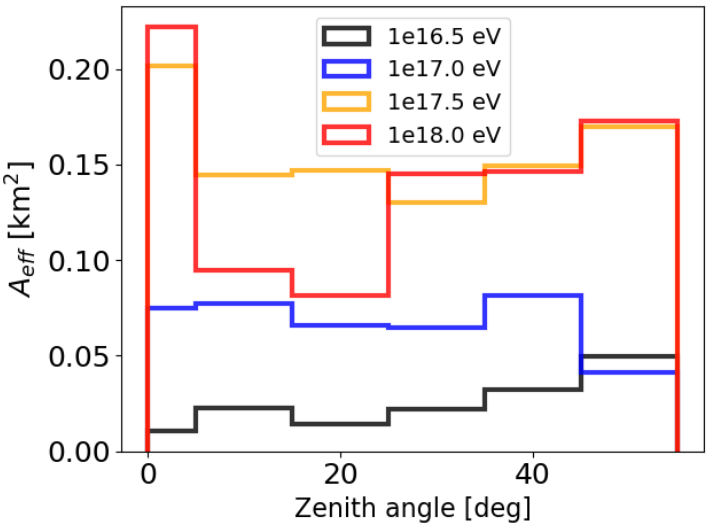

Figure 46: Effective area in different zenith bins and energy bins. The energy bins are the same as in Fig. 45 and the fluence threshold is 1 eV/m^2.

Fig. 47 shows two other plots for higher threshold values: 100 eV/m^2 (top) and 1000 eV/m^2 (bottom). For these very high thresholds, only the highest energies ($10^{17.5}$ and 10^{18} eV) can trigger. In the top figure, the behaviour of the red curve is identical to the one in Fig. 46, meaning that a threshold of 100 eV/m^2 is still too low for the highest energies. What is interesting is that the yellow curve ($10^{17.5}$) now behaves as the black one ($10^{16.5}$) in Fig. 46.
With a threshold of 1000 eV/m^2 (bottom), even the $10^{17.5}$ eV events are not able to trigger anymore, and only the highest energy events remain.
We note also a general decrease of the effective area values with increasing thresholds.

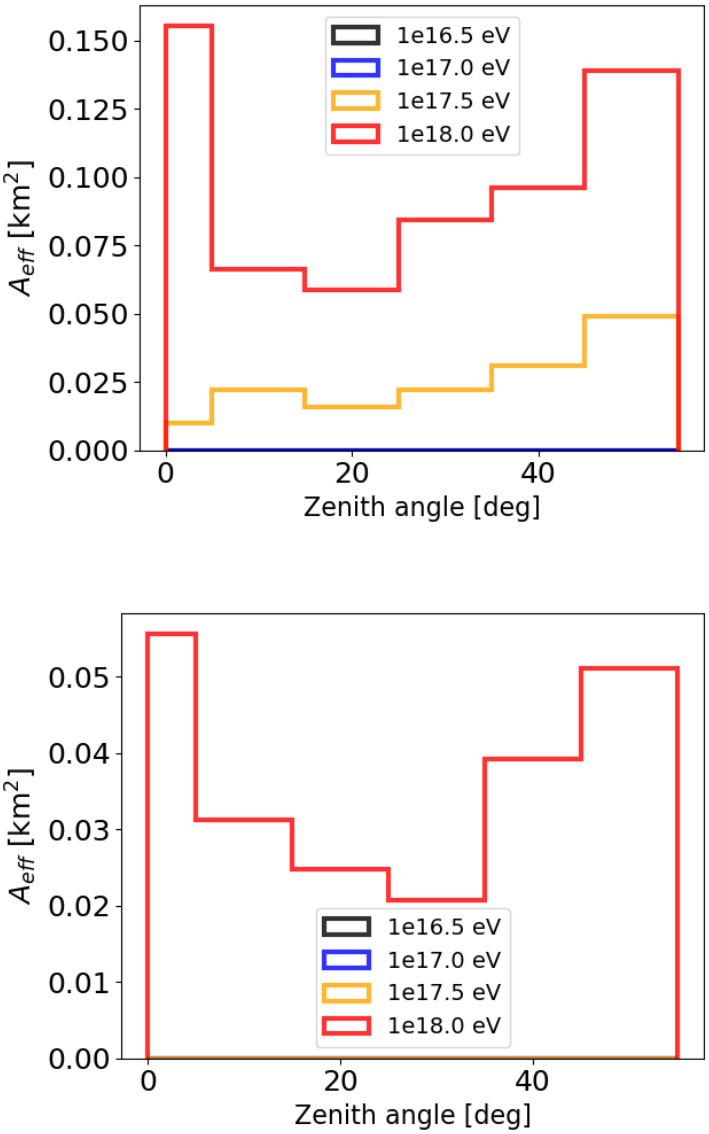

Figure 47: Effective area in different zenith bins and energy bins. The energy bins are the same as in Fig. 45 and the fluence threshold is 100 eV/m^2 (top) and 1000 eV/m^2 (bottom).

D. Cosmic Ray Event Rate

Using Eq. 52, we finally compute an estimate of the number of events per year for ARA's Phased Array. The results are shown in Fig. 48 for two different thresholds: 1 eV/m^2 (top) and 10 eV/m^2 (bottom).

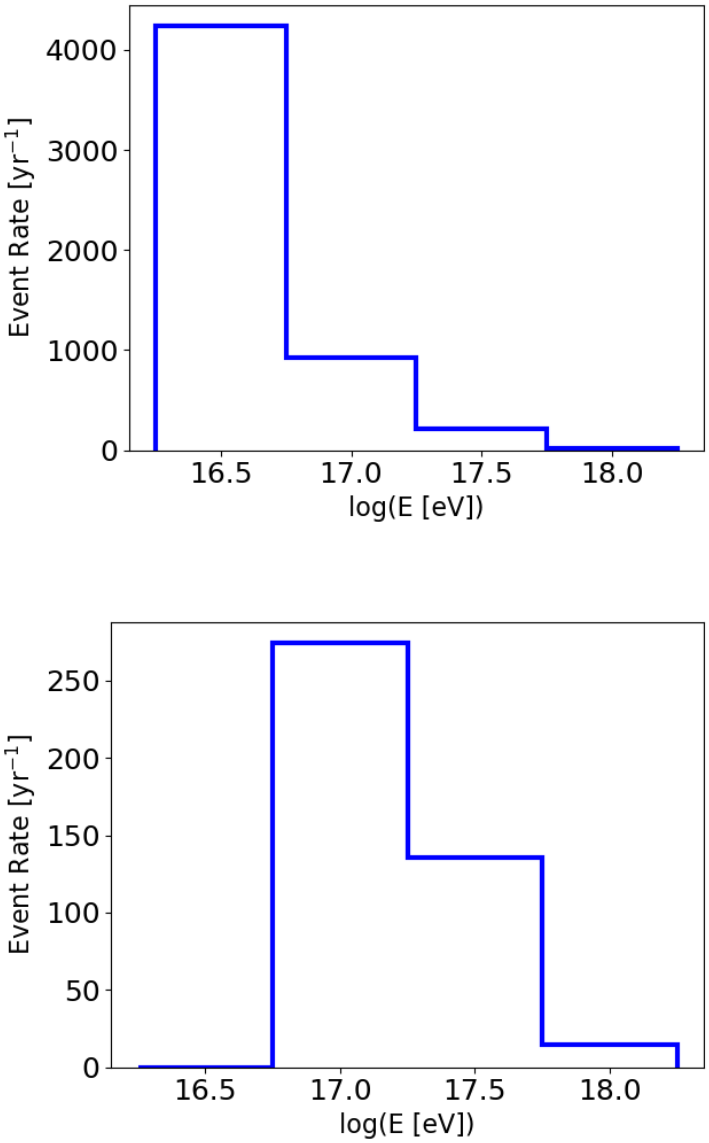

Figure 48: Event rate estimate in ARA's Phased Array in different energy bins and with fluence thresholds of 1 eV/m^2 (top) and 10 eV/m^2 (bottom)

As expected, despite a lower effective area, the low energy events are way more present than the high energy ones for low thresholds since the flux is several orders of magnitude higher. When increasing the fluence threshold, the numerous events at low energies stop triggering and event rate drops thus consequently ($\sim$ 5400 events at 1 eV/m^2 (top) and $\sim$ 425 at 10 eV/m^2 (bottom)). If the CR trigger rate was this high, many more CR candidates would have been

observed in previous analyses. This suggests that the fluence threshold is higher. Fig. 49 shows more realistic event rate for thresholds of 100 eV/m^2 (top) and 1000 eV/m^2 (bottom). These results give respectively ~ 55 and ~ 4 events per year, which fits better the number of CR candidates of previous analyses.

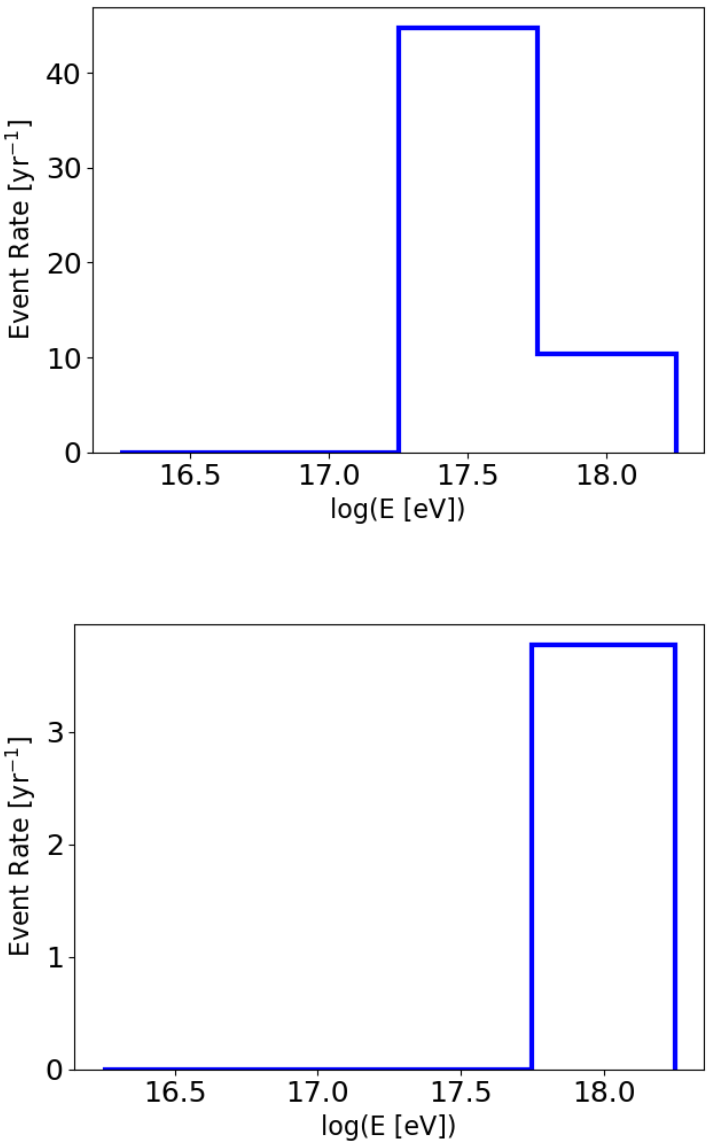

Figure 49: Event rate estimate in ARA's Phased Array in different energy bins and with fluence thresholds of 100 eV/m^2 (top) and 1000 eV/m^2 (bottom)

The relationship between total CR event rate and fluence threshold can be seen in Fig. 50.

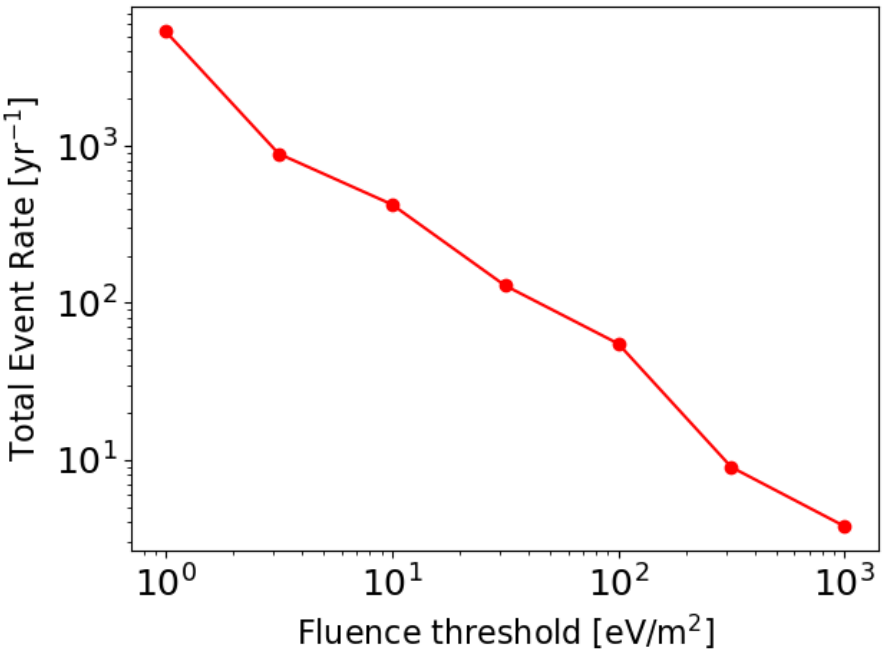

Figure 50: Total number of events per year as seen by ARA's Phased Array as a function of the fluence threshold.

5.7.2 AraSim Results

We now present more realistic results obtained by directly inserting the generated electric fields in AraSim and asking for a SNR above 6.

A. Trigger Map

Fig. 51 shows the four trigger maps corresponding to the four energy bins in which the events are distributed. The statistics is also increased with respect to Fig. 43, 44 since the number of generated events per bin is 250.000.

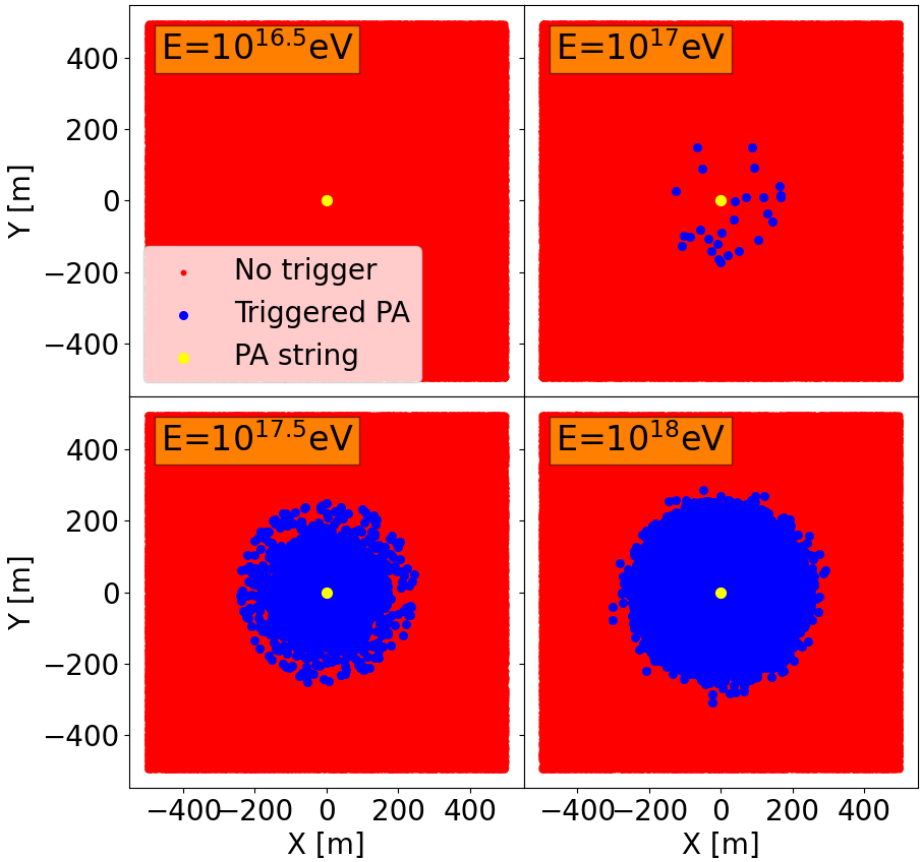

Figure 51: Trigger maps for four different energies, obtained with the trigger condition implemented in AraSim for the Phased Array. Each trigger map contains a total of 250.000 generated events.

The trigger map corresponding to the lowest energy bin (top left) shows absolutely no trigger. This means that we can already exclude the results obtained in section 5.7.1 with the lowest fluence thresholds and implies, in particular, that the event rate is not driven by the "numerous" lowest-energy cosmic rays.

The trigger map for the second lowest energy bin (top right) shows less than 30 triggers over 250.000 events. This indicates that the the threshold for the radio detection method in the case of cosmic rays should be slightly above 10^{17} eV.
The events with an energy in the range $10^{17.25} - 10^{17.75}$ eV (bottom left) trigger more easily, up to $\sim$ 200 m horizontal distances between the shower impact position and the antenna string. We observe that more events trigger very close to the string ($<$ 100 m). At distances between $100 - 200$ m, the number of triggering events start to decrease because the low zenith events stop contributing to the trigger rate.
At the highest energies (bottom right), we observe a large number of triggering events. However, we do not observe the decrease of triggering events at larger distances from the string as in the previous case. The triggering events seem uniformly distributed up to $\sim$ 300 m from the string, which roughly corresponds to the size of the antenna grids used in the simulations. This sharp cut–off around 300 m is thus probably due to the limited size of the antenna grids, since they all miss a part of the radio emission (see Fig. 24).

B. Trigger Efficiency Curves

From Fig. 52, we extract the realistic trigger efficiencies (Eq. 49) of ARA's Phased Array in each energy bin. The trigger efficiency in the two lowest energy bins is negligible. In the energy bins centered around $10^{17.5}$ eV and 10^{18} eV, the trigger efficiency is respectively $\sim 0.7\%$ and $\sim 3.3\%$.

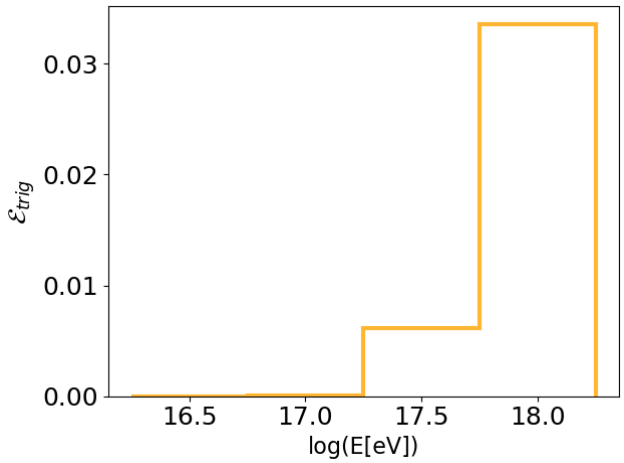

Figure 52: Cosmic–ray trigger efficiency of ARA's Phased Array with the trigger condition $SNR_{PA} > 6$.

Comparing with Fig. 45, this suggests a fluence threshold of $\sim$ 1000 eV/m^2, although the fluence threshold is not the exact trigger condition. Note that the trigger efficiency in the highest energy bin implies an effective area of $\sim$ 33.000 m^2 which corresponds to a disk of radius $\sim$ 100 m.

C. Effective Area Results

Fig. 53 is the equivalent of Fig. 46, 47 but with the more realistic trigger condition described above. We observe a sawtooth structure that indicates a difficulty to trigger in certain zenith bins, at least at the highest energies. These problematic zenith bins are exactly the ones where a proper simulation could not be performed in the two highest energy bins and where energy scaling was used instead to infer the electric fields. Therefore, this feature of Fig. 53 is most likely the sequel of a flaw in the energy scaling procedure, rather than an actual physical effect. However, the fluence plots made from the scaled values of electric fields at $10^{17.5}$ (Appendix B, Fig. 57) do not show any striking differences with the simulated ones (Fig. 25) and the sawtooth structure of Fig. 53 is absent in Fig. 46, 47. The exact cause of this problematic feature therefore requires further investigation.

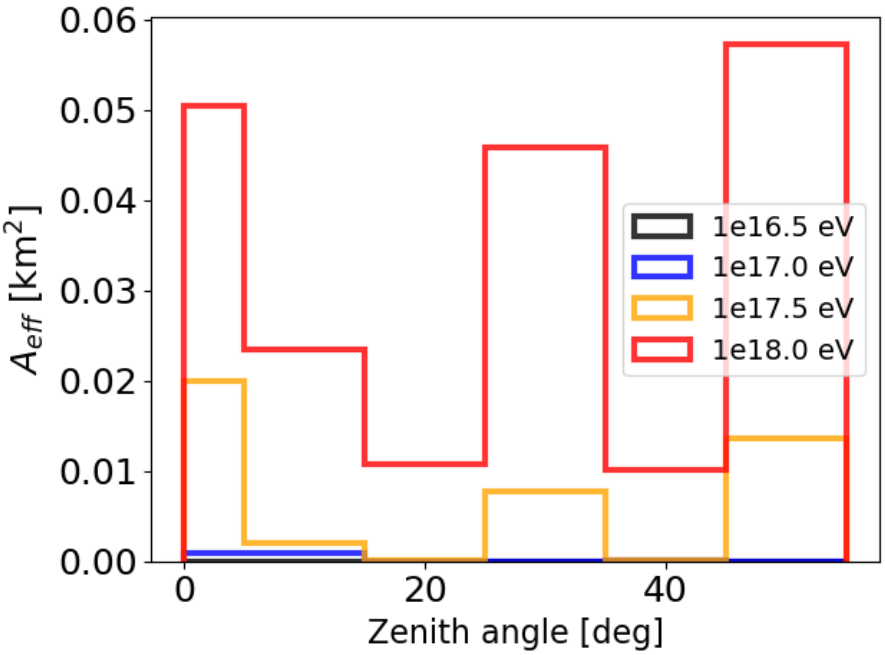

Figure 53: Effective area in different zenith bins and energy bins, with a more realistic trigger condition: $SNR_{PA} > 6$.

Fig. 54 represents the effective area as a function of the distance between the shower impact position and the top of the Phased Array string. We observe a maximum at a non–zero distance, followed by a sharp decrease up to ~ 300 m. The non–zero maximum represents the difficulty to trigger on a shower that hits the ice right on top of the Phased Array. It can be understood the following

way: For vertical showers, the in–air emission is weaker than the in–ice emission, and the latter is initially emitted at an angle higher than 42°, so that it never reaches the Phased Array. For high zenith angles, the radio footprints at depths $145 - 200$ m in the ice are shifted towards increasing distances from the Phased Array.
The sharp cut–off at $\sim$ 300 m is also an effect of the limited grid sizes. If the simulations were performed with infinite grids, the tail of the distribution in Fig. 54 would probably have been smoother and would have extended to greater distances.

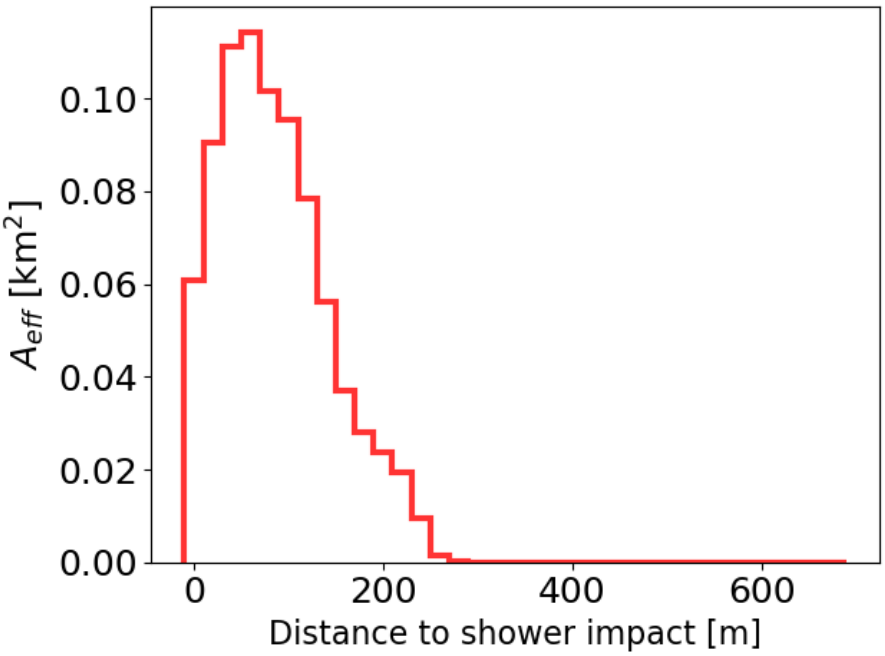

Figure 54: Effective area in different bins of horizontal distance between the shower impact position and the Phased Array.

D. Cosmic Ray Event Rate

Finally, we present the estimated event rate in ARA's Phased Array. As can be seen in Fig. 55 and Eq. 52, the event rate is a compromise between the trigger efficiency and the steeply falling cosmic ray flux with increasing energies. The good balance is found in the range $10^{17.25} - 10^{17.75}$ eV. The expected event rates are written in Table 7.

Energy bin (eV)	Event rate ($year^{-1}$)
$10^{16.25} - 10^{16.75}$	0
$10^{16.75} - 10^{17.25}$	2
$10^{17.25} - 10^{17.75}$	8
$10^{17.75} - 10^{18.25}$	3

Table 7: Estimated UHE–CR event rate per energy bin in ARA's Phased Array.

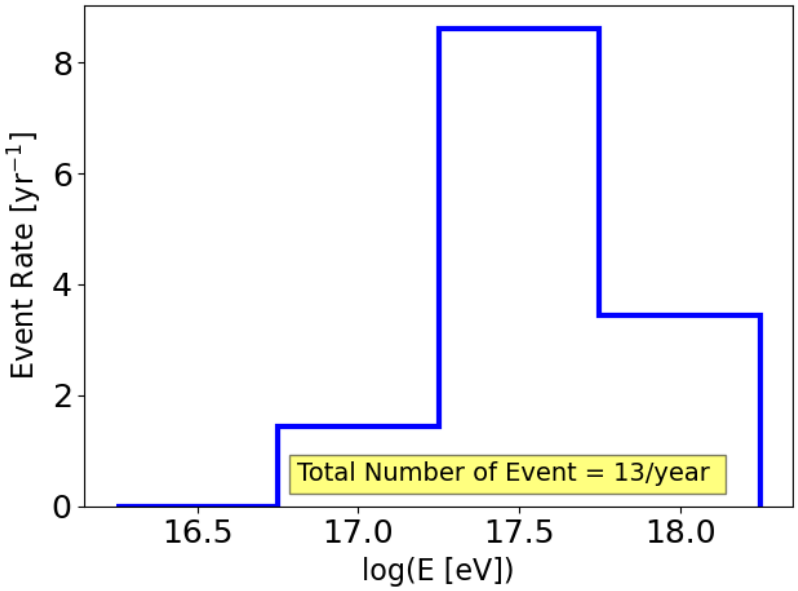

Figure 55: Estimated UHE–CR event rate per energy bin in ARA's Phased Array.

Conclusion of this work: The total number of Ultra–High–Energy cosmic ray events expected in ARA's Phased Array is 13 per year.

This number seems reasonable considering the number of cosmic ray candidates found in previous analyses. However, due to the problematic feature of Fig. 53, this event rate is probably underestimated.
The average of the effective area in the non–problematic zenith bins of Fig. 53 (0-5°, 25-35°, 45-55°), is respectively 0.014 km^2 and 0.051 km^2 for $10^{17.5}$ eV and 10^{18} eV. Using these values instead, we obtain a total event rate estimate of 25 events per year, i.e. twice as many.

6 Conclusion

We produced a simulated dataset of radio emission originating from cosmic–ray initiated air–showers as well as their in–ice continuation. The dataset covers wide areas filled with antennas at depths between -145 m and -200 m. From this library of simulations, we were able to generate random events in an energy range of $10^{16.25}-10^{18.25}$ eV and a zenith range of $0-55°$. We then implemented a simple trigger condition using a fluence threshold to determine whether an ARA station triggers or not. This procedure allowed us to estimate the effective area of ARA's Phased Array, as well as the number of cosmic–ray events that the latter should observe per year. The results depend on one parameter which is the fluence threshold. A more accurate study using AraSim to directly simulate the detector response to simulated electric fields provided an event rate estimate of 13/year. However, this result is very likely to be an underestimate, and the actual event rate could be twice as high.

In future research, the library of simulated CR events will allow us to search for CR signals in ARA and verify the identity of the CR candidates observed in previous studies. We could either use template matching on the CR candidates or try to reproduce them by generating cosmic–ray events with the setup developed in this work.
Furthermore, the CR signal properties inferred from the library will allow us to build a CR discriminant for neutrino searches in ARA. This discriminant could be based on the primary particle properties as the zenith angle or the distance of the shower impact position from the antennas, or could be based on properties of the signal as, for example, its amplitude or time evolution. This is especially important as the ARA collaboration is in the process of analysing 25 station–years of data to hopefully discover the first ultra high energy neutrino.

7 Acknowledgements

I would like to emphasize that this work was only made possible through the invaluable help of several individuals from the IIHE. Firstly, I am grateful to Simon De Kockere, who taught me how to use the simulation framework and assisted me with debugging throughout the year. I am also very thankful to Abby Bishop from Wisconsin for her help on simulating the antenna responses with AraSim, and to Simon Chiche who joined mid–year and who shared his experience and some of his codes with me. I am particularly indebted to my two supportive supervisors, Simona Toscano and Krijn De Vries, whose enlightened ideas and passion for research guided me throughout the year. Additionally, I would like to thank the IIHE IT team for their prompt responses and hard work in maintaining the IIHE cluster in good condition, despite the countless simulations it had to handle from me.

A Simulations Inputs

The inputs used for the simulations are the following:

- Earth magnetic field [11]:
  - Horizontal component: $B_{hor} = 16.7525\ \mu T$ (to the x–direction of the coordinate system = North (see Fig. 19))
  - Vertical component: $B_{ver} = -52.0874\ \mu T$ (downwards)
- Ground level: 2835 m asl or 728.67 g/cm^2 in slant–depth
- Primary type = proton: Heavier primaries are equivalent to considering higher altitudes of X_{max} (see Eq. 18), so that we can fix the primary type and vary X_{max} instead.
- Thinning used in CORSIKA:
  - Electromagnetic particles with an energy lower than $10^{-5}E_p$ are combined, where E_p is the primary energy
  - No hadronic thinning
- Cuts to eliminate low energy particles from the shower: $E_{hadron,muon} < 0.3$ GeV and $E_{e^-,\gamma} < 0.401$ MeV
- Primary energy range: from $10^{16.5}$ eV (slightly above radio detection threshold) to 10^{18} eV (to keep a reasonable CPU time consumption and because hadronic models start to fall in accuracy)
- Zenith angle range: from 0° (vertical) to 50° (above 60° the in–ice cascade contribution to the radio signal is expected to be negligible and the flat Earth approximation is not valid anymore)
- Azimuth angle = 0°: In principle the radio signal depends on the azimuth angle through the angle between the shower axis and the Earth magnetic field, but the magnetic field lines are almost vertical in South-Pole. Cylindrical symmetry is therefore a good approximation.

[11] Obtained from the program Geomag which is available on-line in the world wide web [83]

B Library Fluence Plots

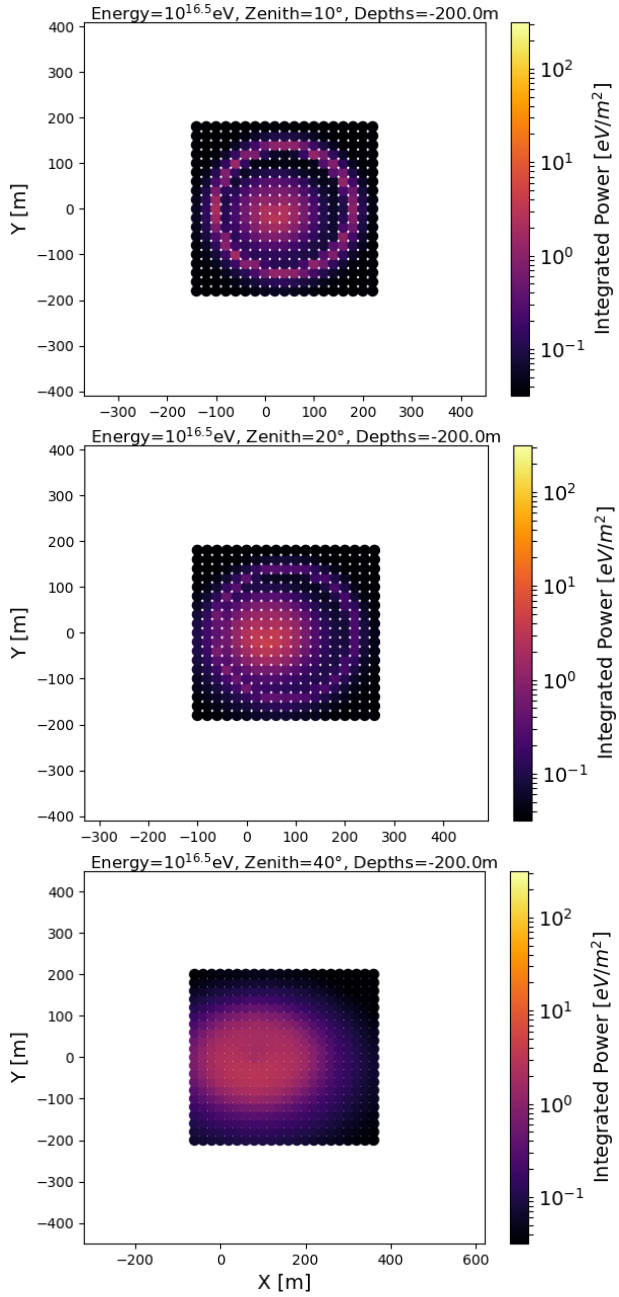

Figure 56: Radio footprints at 200 m depth for a proton primary with energy $10^{16.5}$ eV and zenith angle 10° (top), 20° (middle) and 40° (bottom).

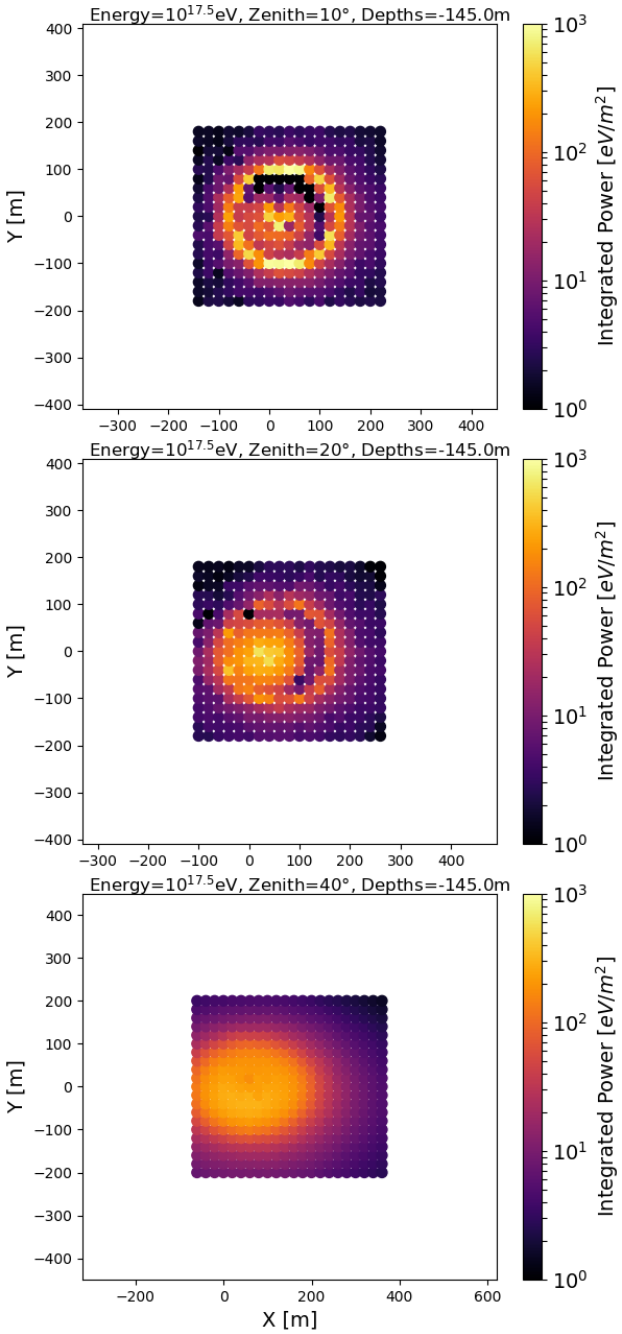

Figure 57: Radio footprints at 145 m depth for a proton primary with energy $10^{17.5}$ eV and zenith angle 10° (top), 20° (middle) and 40° (bottom). These footprints were obtained with an energy scaling from the electric fields at $10^{16.5}$ eV, as explained in Section 5.1.4.

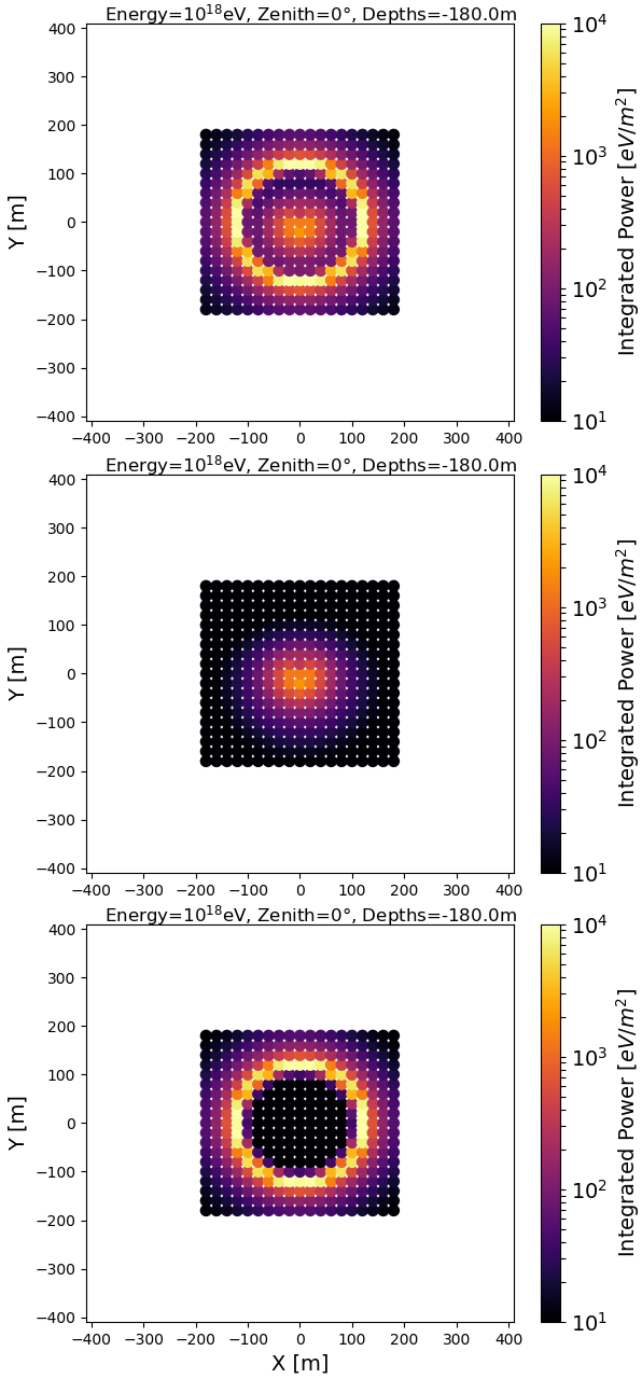

Figure 58: Radio footprints at 180 m depth for a proton primary with energy 10^{18} eV and zenith 0°. **Top:** full emission. **Middle:** in–air emission only. **Bottom:** in–ice emission only.

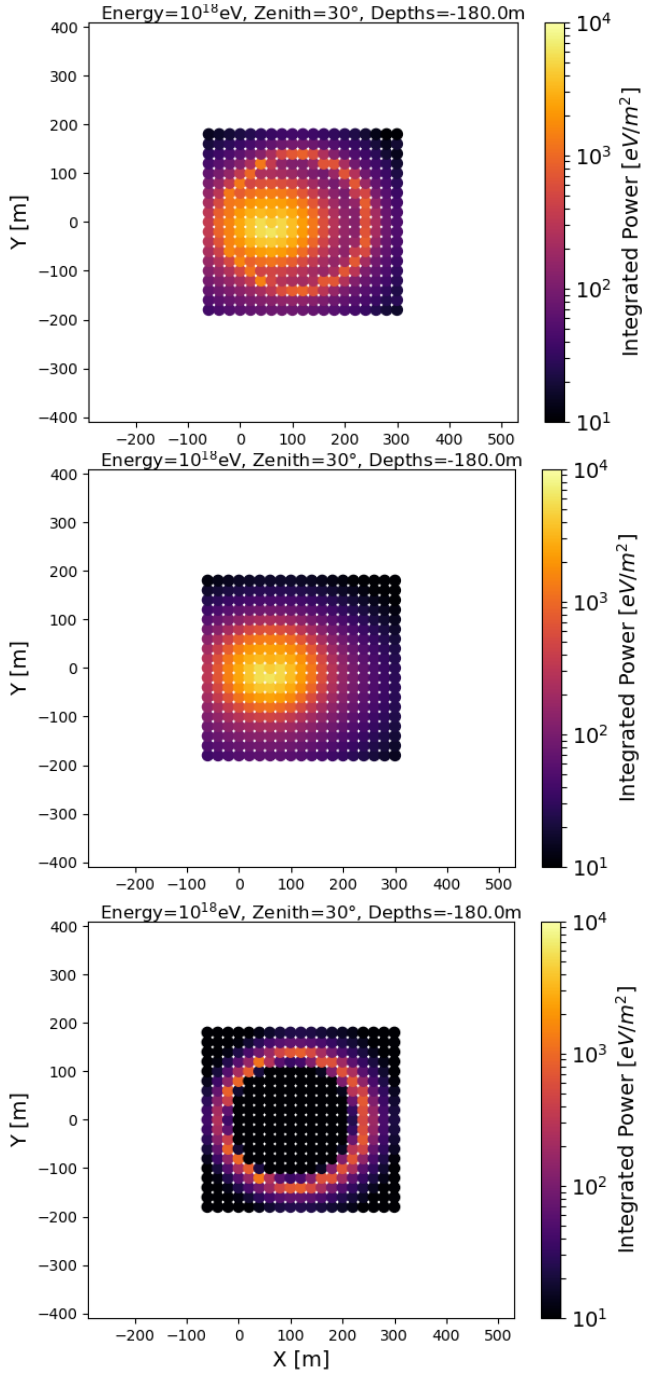

Figure 59: Radio footprints at 180 m depth for a proton primary with energy 10^{18} eV and zenith 30°. **Top:** full emission. **Middle:** in–air emission only. **Bottom:** in–ice emission only.

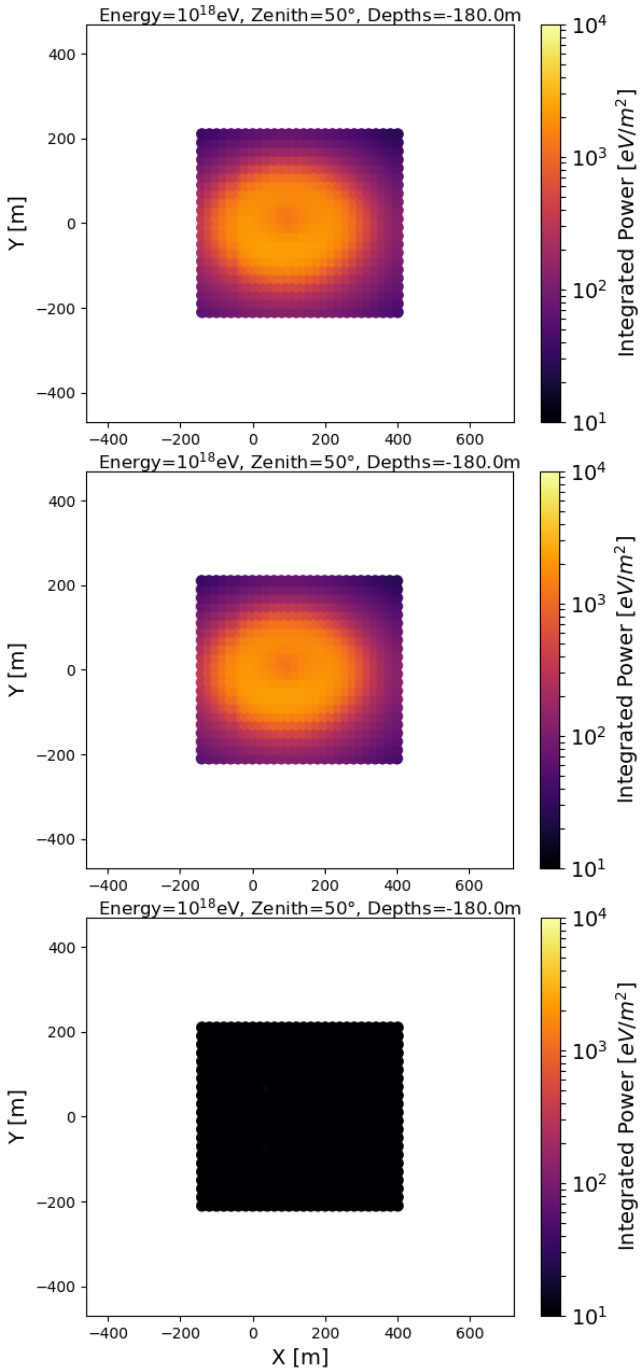

Figure 60: Radio footprints at 180 m depth for a proton primary with energy 10^{18} eV and zenith 50°. **Top:** full emission. **Middle:** in–air emission only. **Bottom:** in–ice emission only.

C More Final Results

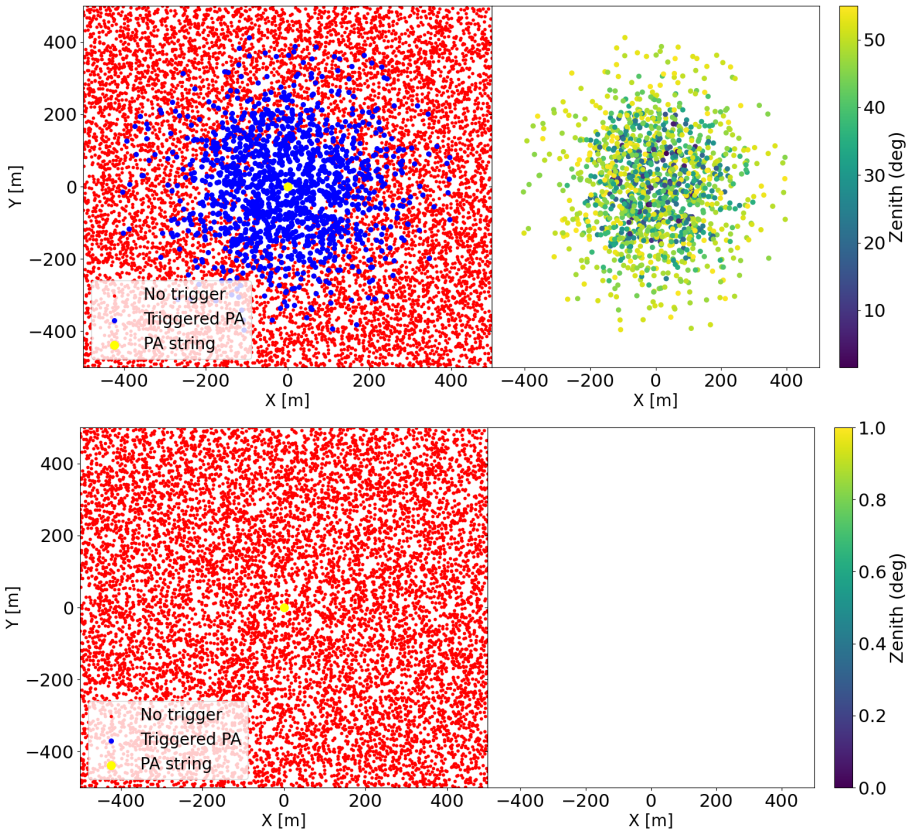

Figure 61: Trigger maps for an energy range of $10^{16.25} - 10^{16.75}$ eV and a fluence threshold of 0.1 eV/m^2 (top), and 10 eV/m^2 (bottom).

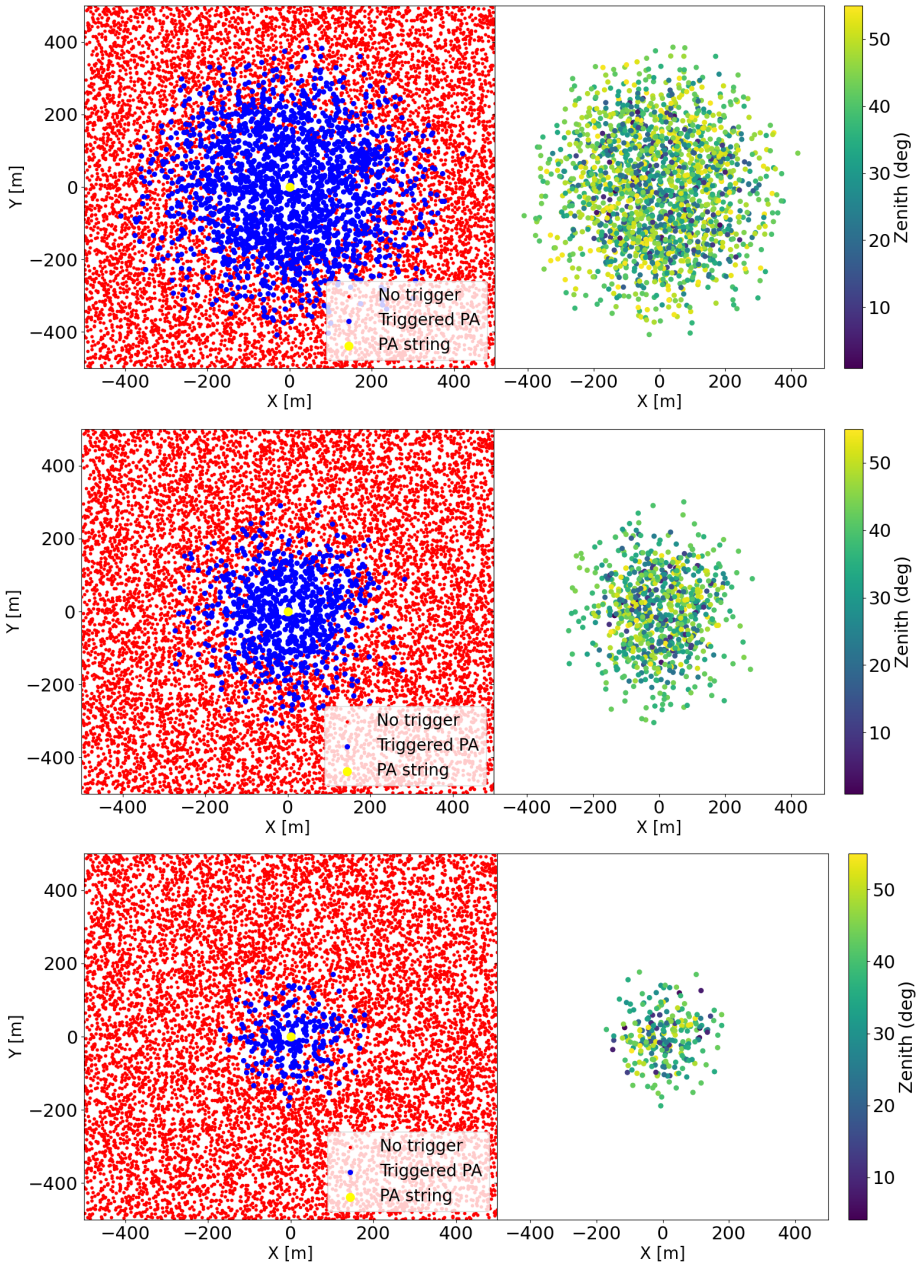

Figure 62: Trigger maps for an energy range of $10^{16.75}-10^{17.25}$ eV and a fluence threshold of 0.1 eV/m^2 (top), 1 eV/m^2 (middle), and 10 eV/m^2 (bottom).

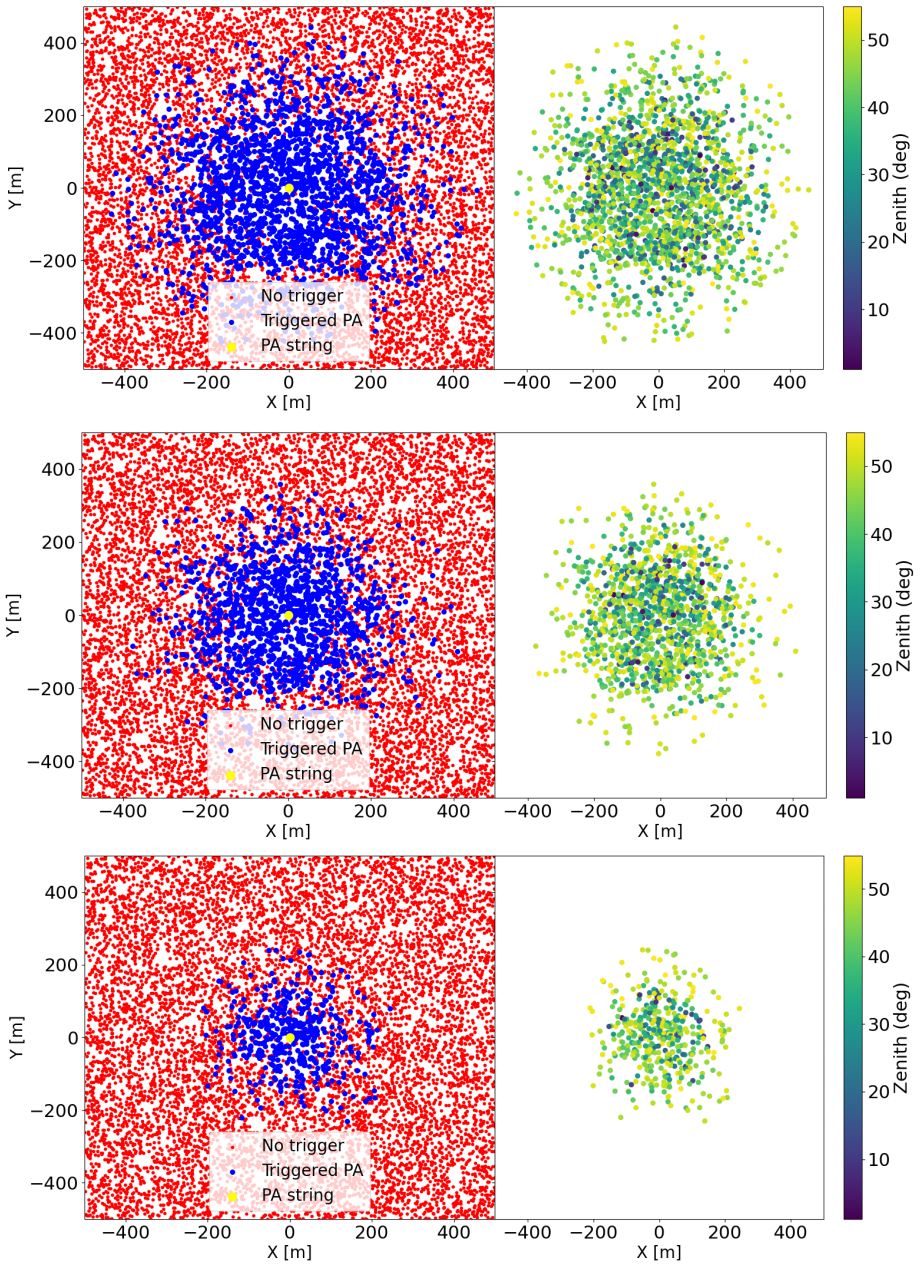

Figure 63: Trigger maps for an energy range of $10^{17.25}$–$10^{17.75}$ eV and a fluence threshold of 1 eV/m^2 (top), 10 eV/m^2 (middle), and 100 eV/m^2 (bottom).

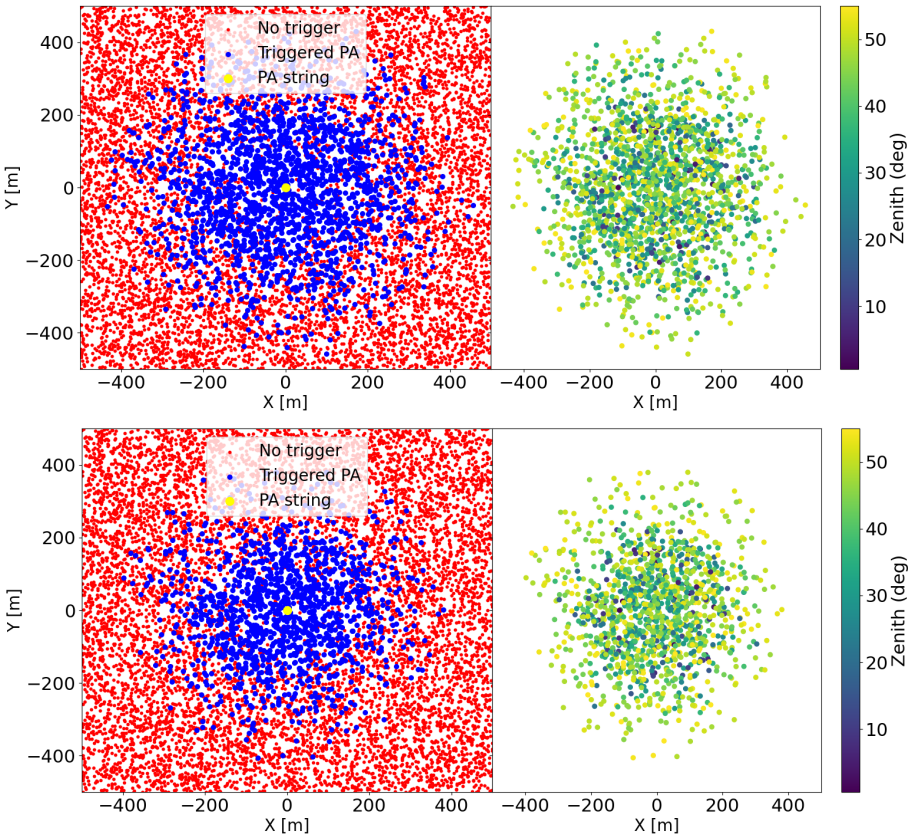

Figure 64: Trigger maps for an energy range of $10^{17.75} - 10^{18.25}$ eV and a fluence threshold of 10 eV/m^2 (top), and 100 eV/m^2 (bottom).

References

[1] Theodor Wulf. Observations of the radiation of high-penetration capacity on the Eiffel Tower. *Physikalische Zeitschrift*, 11:811–813, 1910.

[2] Per Carlson. A century of cosmic rays. *Physics Today*, 65(2):30–36, 02 2012.

[3] Frederick Reines et al. Detection of the free neutrino. *Science*, 124(103), 1953.

[4] J. N.; Davis Jr. Bahcall. Solar Neutrinos: A Scientific Puzzle. *Science*, 191(4224):264–267, 1976.

[5] K. Hirata et al. Observation of a Neutrino Burst from the Supernova SN 1987a. *Phys. Rev. Lett.*, 58:1490–1493, 1987.

[6] IceCube Collaboration. Evidence for high-energy extraterrestrial neutrinos at the icecube detector. *Science*, 342(6161), November 2013.

[7] Abbott B. P. et al. Observation of gravitational waves from a binary black hole merger. *Phys. Rev. Lett.*, 116:061102, Feb 2016.

[8] Juan Antonio AGUILAR SANCHEZ. Astroparticle physics. Course given at the ULB university, 2021–2022.

[9] D. Semikoz. Multi-messenger observations with cosmic rays, gamma-rays and neutrinos, present status and future perspectives. *Journal of Physics: Conference Series*, 1263:012009, 06 2019.

[10] Kenneth Greisen. End to the cosmic-ray spectrum? *Phys. Rev. Lett.*, 16:748–750, Apr 1966.

[11] G.T. Zatsepin and V.A. Kuz'min. Upper limit of the spectrum of cosmic rays. *Journal of Experimental and Theoretical Physics Letters*, 4:78–80, 1966.

[12] J.D. Myers. https://fermi.gsfc.nasa.gov/.

[13] John Bahcall and Eli Waxman. High energy astrophysical neutrinos: the upper bound is robust. *Physical Review D - PHYS REV D*, 64, 02 1999.

[14] Aartsen et al. Neutrino emission from the direction of the blazar txs 0506+056 prior to the icecube-170922a alert. *Science*, 361(6398):147–151, July 2018.

[15] M.G. Aartsen et al. Evidence for neutrino emission from the nearby active galaxy ngc 1068. *Science*, 378(6619):538–543, November 2022.

[16] R. Abbasi et al. Observation of high-energy neutrinos from the galactic plane. *Science*, 380(6652):1338–1343, 2023.

[17] J.C. Arteaga-Vel´azquez et al. Testing hadronic interaction models with the attenuation length of muons in kascade-grande. *Proc. of Science PoS(ICRC2015) 314*, 2015.

[18] Aab et al. Muons in air showers at the pierre auger observatory: Mean number in highly inclined events. *Phys. Rev. D*, 91:032003, Feb 2015.

[19] Schatz G.; Thouw T.; Werner K.; Oehlschlager J. and Bekk K. Validity of the superposition model for extensive air showers. *J. Phys. G: Nucl. Part. Phys.*, 20:1267–81, 02 1994.

[20] A. Aab et al. *Nucl. Instr. and Meth. A*, 798(172), 2015.

[21] Kelley Christensen. Detecting cosmic rays from a galaxy far, far away. `https://www.mtu.edu/news/2017/09/detecting-cosmic-rays-galaxy-far-far-away.html`, 2017.

[22] P. Allison et al. *Astropart. Phys.*, 35(457), 2012.

[23] P. Allison et al. *Astropart. Phys.*, 70(62), 2015.

[24] J. A. Aguilar et al. Design and Sensitivity of the Radio Neutrino Observatory in Greenland (RNO-G). *JINST*, 16(03):P03025, 2021. [Erratum: JINST 18, E03001 (2023)].

[25] J. Jelley et al. Radio pulses from extensive air showers. *Nature*, 1965.

[26] H. et al. Falcke. Detection and imaging of atmospheric radio flashes from cosmic ray air showers. *Nature*, 435(7040):313–316, May 2005.

[27] D. Ardouin et al. Detection and imaging of atmospheric radio flashes from cosmic ray air showers. *Nucl. Instr. and Meth. A*, 555(148), 2005.

[28] Schellart P. et al. Detecting cosmic rays with the lofar radio telescope. *Astronomy amp; Astrophysics*, 560:A98, December 2013.

[29] D. Kostunin et al. *Astropart. Phys.*, 74(79), 2015.

[30] Pierre Auger Collaboration. *Phys. Rev. D*, 89(052002), 2014.

[31] Frank G. Shröder. Radio detection of cosmic-ray air showers and high-energy neutrinos. *arXiv:1607.08781 [astro-ph.IM]*, 2017.

[32] F.D. Kahn and I. Lerche. *Math. and Phys. Sciences*, 289(206), 1967.

[33] S.A. Colgate. *Jounal of Geophysical Research*, 72(4869), 1967.

[34] G.A. Askaryan. *Soviet Physics JETP*, 14(441), 1962.

[35] Tim Huege. Radio detection of cosmic ray air showers in the digital era. *arXiv:1601.07426v1 [astro-ph.IM]*, 26 january 2016.

[36] G.A. Askaryan and M.S. Rabinovich. Cascade Ionization Induced in a Medium by an Intense Light Flash. *JETP*, 21(1):190, 1965.

[37] G.A. Askaryan. Excess Negative Charge of an Electron-Photon Shower and its Coherent Radio Emission. *JETP*, 14(2):441, 1962.

[38] N. van Eijndhoven S. De Kockere, K.D. de Vries and U.A. Latif. Simulation of in-ice cosmic ray air shower induced particle cascades. *arXiv:2202.09211v2 [astro-ph.HE]*, 25 august 2022.

[39] P. Schellart et al. *J. Cosmol. Astropart. Phys.*, 10(014), 2014.

[40] S. De Kockere; Dieder Van den Broeck; Uzair Abdul Latif; Krijn D. de Vries; Nick van Eijndhoven; Tim Huege and Stijn Buitink. Simulation of radio signals from cosmic-ray cascades in air and ice as observed by in-ice askaryan radio detectors. *arXiv:2403.15358v1 [astro-ph.HE]*, 22 march 2024.

[41] D. Heck and T. Pierog. *Extensive Air Shower Simulation with CORSIKA : A User's Guide*. KARLSRUHER INSTITUT FÜR TECHNOLOGIE(KIT), April 2023.

[42] Tim Huege. *CoREAS 1.4 Users Manual*. Online Manual, August 26, 2019.

[43] S. Agostinelli et al. Geant4 - a simulation toolkit. *Nucl. Instrum. Meth. A 506 250-303*, 2003.

[44] D. Heck, J. Knapp, J.N. Capdevielle, G. Schatz, and T. Thouw. Corsika: A monte carlo code to simulate extensive air showers. `https://www.iap.kit.edu/corsika/70.php`, 1998. Forschungszentrum Karlsruhe.

[45] S. Agostinelli et al. Recent developments in geant4. *Nucl. Instrum. Meth. A 835 186-225*, 2016.

[46] J. Allison et al. Geant4 developments and applications. *IEEE Trans. Nucl. Sci. 53 270-278*, 2006.

[47] T. Huege; M. Ludwig and C. W. James. Simulating radio emission from air showers with coreas. *arXiv:1301.2132 [astro-ph.HE]*, 10 january 2013.

[48] Stefan Roesler; Ralph Engel and Johannes Ranft (Univ. of Siegen). The monte carlo event generator dpmjet-iii. *arXiv:hep-ph/0012252*, 19 december 2000.

[49] J.N. Capdevielle et al. The karlsruhe extensive air shower simulation code corsika. *Report KfK 4998*, 1992.

[50] N.N. Kalmykov and S.S. Ostapchenko. The nucleus-nucleus interaction, nuclear fragmentation, and fluctuations of extensive air showers. *Yad. Fiz. 56 105; Phys. At. Nucl. 56 N3*, 1993.

[51] R.S. Fletcher; T.K. Gaisser; P. Lipari, , and T. Stanev. Sibyll: An event generator for simulation of high energy cosmic ray cascades. *Phys. Rev. D50 5710; J.*, 1994.

[52] R. Engel et al. Hadronic interaction model sibyll 2.3d and extensive air showers. *arXiv: 1912.03300 [astro-ph]*, 2019.

[53] K. Werner. Strings, pomerons and the venus model of hadronic interactions at ultrarelativistic energies. *Phys. Rep. 232 87*, 1993.

[54] H.J. Drescher et al. Parton-based gribov-regge theory. *Phys. Rep. 350 93*, 2001.

[55] T. Pierog et al. Epos lhc: Test of collective hadronization with data measured at the cern large hadron collider. *Phys. Rev. C92 (2015) 034906*, 2015.

[56] S.S. Ostapchenko. Monte carlo treatment of hadronic interactions in enhanced pomeron scheme: Qgsjet-ii model. *Phys. Rev. D83 014018*, 2011.

[57] In search of the strong interaction: The pomeron. `https://cms.cern/news/search-strong-interaction-pomeron`, 2023.

[58] A. Ferrari; P.R. Sala; A. Fass‘ o and J. Ranft. Fluka : A multi-particle transport code. *Report CERN-2005-10*, 2005.

[59] H. Fesefeldt. The simulations of hadronic showers. *Report PITHA-85/02*, 1985.

[60] S.A. Bass et al. The simulations of hadronic showers. *Prog. Part. Nucl. Phys. 41 225*, 1998.

[61] W.R. Nelson; H. Hirayama and D.W.O. Rogers. The egs4 code system: Solution of gamma-ray and electron transport problems. *Report SLAC 265*, 1985.

[62] A.A. Lagutin; A.V. Plyasheshnikov and V.V. Uchaikin. The ehistory option of the air-shower simulation program corsika. *Proc. 16th Int. Cosmic Ray Conf.*, 2009.

[63] A. Misaki. The landau - pomeranchuk - migdal (lpm) effect and its influence on electromagnetic cascade showers at extremely high energies. *Nuclear Physics B - Proceedings Supplements*, 33(1):192–199, 1993.

[64] C. W. James; H. Falcke; T. Huege and M. Ludwig. General description of electromagnetic radiation processes based on instantaneous charge acceleration in 'endpoints'. *arXiv:1007.4146*, 2011.

[65] Kaeli Autumn Hughes. *A low threshold neutrino search with the Askaryan Radio Array*. PhD thesis, UNIVERSITY OF CHICAGO, June 2022.

[66] C. Glaser et al. Nuradiomc: simulating the radio emission of neutrinos from interaction to detector. *European Physical Journal C 80, 77*, 2020.

[67] I. Kravchenko; D. Besson and J. Meyers. In situ index-of refraction measurements of the south polar firn with the rice detector. *Journal of Glaciology 50, 522–532*, 2004.

[68] Juan Ammerman-Yebra; Uzair Abdul Latif; Nikolaos Karastathis and Tim Huege. Simulations of cross media showers with corsika 8. *PoS(ICRC2023)442*, 2023.

[69] A. Corstanje; S. Buitink; M. Desmet and H. Falcke et al. A high-precision interpolation method for pulsed radio signals from cosmic-ray air showers. *Journal of Instrumentation 18 (09), P09005*, 2023.

[70] Ilya Kravchenko; David Besson and Josh Meyers. In situ index-of-refraction measurements of the south polar firn with the rice detector. *Journal of Glaciology , Volume 50 , Issue 171*, 2017.

[71] P. Allison et al. Design and performance of an interferometric trigger array for radio detection of high-energy neutrinos. *Nuclear Instruments and Methods in Physics, Research A, 930:112–125*, 2019.

[72] `https://meetings.aps.org/Meeting/APR20/Session/R09.5`.

[73] Uzair Latif. Towards measurement of uhe-cr with the ara experiment. *[Order No. 28029861]. University of Kansas.*, 2020.

[74] Kaeli Hughes. Implementing a low-threshold analysis with the askaryan radio array (ara). *PoS ICRC2021*, 2021.

[75] Barwick et al. Radio detection of air showers with the arianna experiment on the ross ice shelf. *Astroparticle Physics*, 90:50–68, April 2017.

[76] Dasgupta et al. Progress towards a diffuse neutrino search in the full livetime of the askaryan radio array. In *Proceedings of 38th International Cosmic Ray Conference — PoS(ICRC2023)*, ICRC2023. Sissa Medialab, August 2023.

[77] P. Allison et al. for the ARA Collaboration. First constraints on the ultra-high energy neutrino flux from a prototype station of the askaryan radio array. *Astroparticle Physics, Vol 70, Pg 62-80*, 2015.

[78] The Pierre Auger Collaboration. The pierre auger observatory upgrade "augerprime". *arXiv:1604.03637v1 [astro-ph.IM]*, 2016.

[79] Aartsen et al. Measurement of the cosmic ray energy spectrum with icetop-73. *Physical Review D*, 88(4), August 2013.

[80] The Pierre Auger Collaboration. Features of the energy spectrum of cosmic rays above 2.5×10^{18}ev using the pierre auger observatory. *Physical Review Letters*, 125(12), September 2020.

[81] Vladimír Novotný et al. Energy spectrum of cosmic rays measured using the pierre auger observatory. *PoS(ICRC2021)324*, 2021.

[82] R. Abbasi et al. *Nucl. Instr. and Meth. A*, 700(188), 2013.

[83] National Centers for Environmental Information. `http://www.ngdc.noaa.gov/geomag/`.